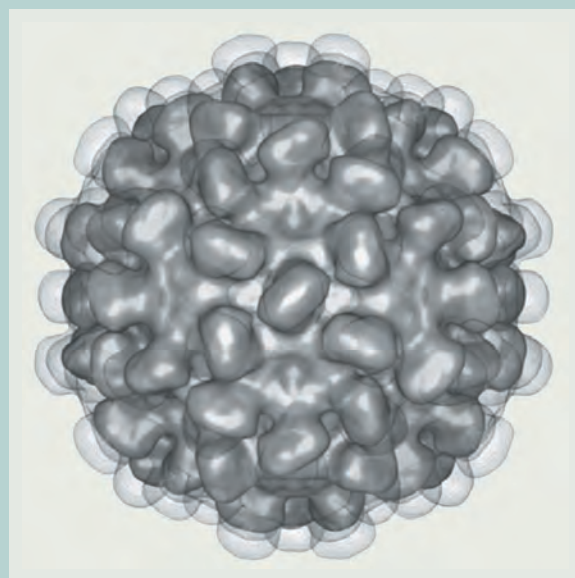
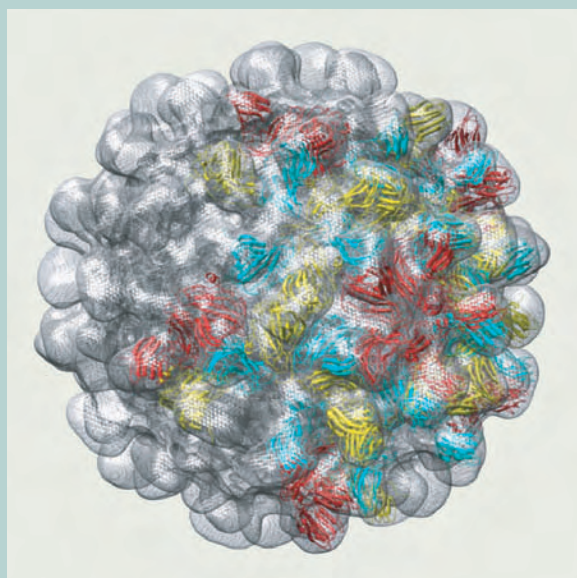
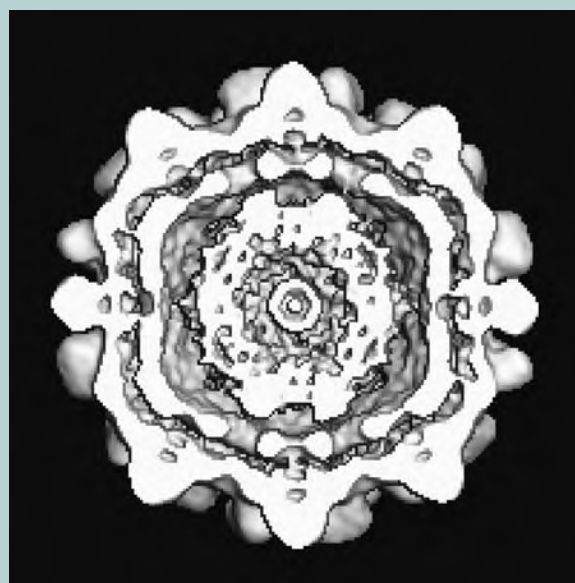
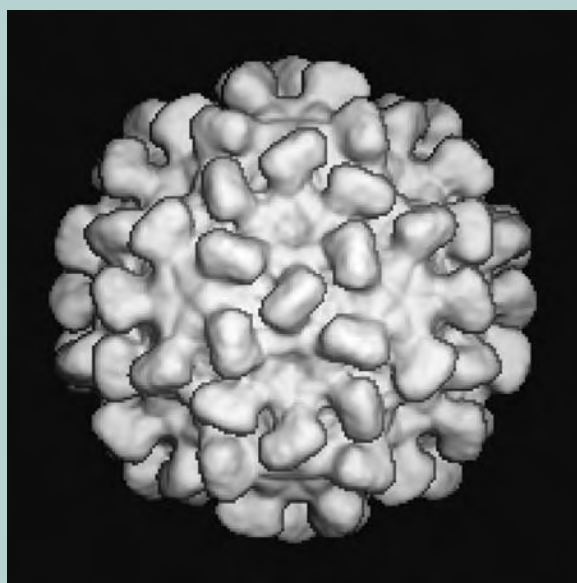
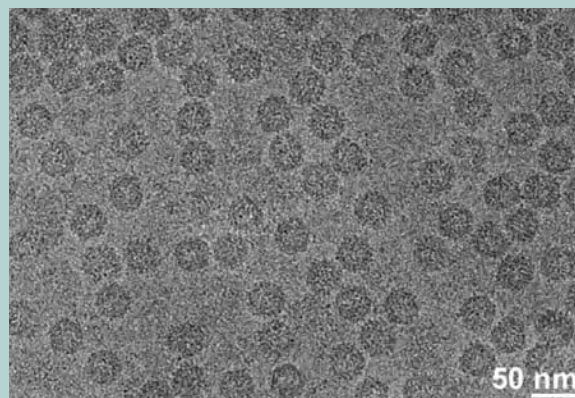
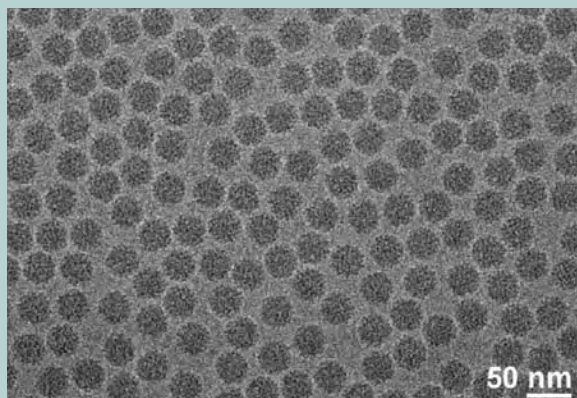


# JEOL news

July 2005 Vol. **40** No. **1**



# Three-Dimensional Reconstruction of Biological Macromolecular Complexes Using Cryoelectron Microscopy on Frozen-Hydrated Samples

Eric Larquet and Nicolas Boisset

Department of Structural Biology at the «Institut de Minéralogie et de Physique des Milieux Condensés»

## Contents

Three-Dimensional Reconstruction of Biological Macromolecular Complexes Using Cryoelectron Microscopy on Frozen-Hydrated Samples . . . . .	2
Direct Analysis in Real Time (DART™) Mass Spectrometry . . . . .	8
High Energy Backscattered Electron Imaging of Subsurface Cu Interconnects . . . . .	13
Recent Development of TEM for Advanced Ceramics . . . . .	18
Advanced Analysis Technology Supporting SiP . . . . .	24
FT NMR New Technical Introduction . . . . .	29
● Introduction of Fully Automatic NMR Measurement Tool "GORIN" for Protein Solution	
● 100 Sample Auto Sample Changer and Tubeless NMR	
● Windows Delta	
● Latest Information and Future for ALICE2 Software	
Features and Applications of Newly-Developed GC-TOFMS "The AccuTOF GC" . . . . .	38
Development of Ion Slicer (Thin-Film Specimen Preparation Equipment) . . . . .	46
Introduction of Wafer Edge SEM Review . . . . .	50

## Cover micrograph

CryoEM applications to a swollen Tomato Bushy Stunt Virus (TBSV). TEM images of TBSV (taken with JEM-2100F with minimum dose system) and its 3D reconstructed structures obtained using image processing techniques. (See pages 2 to 7)

Courtesy of Dr. Nicolas Boisset, Department of Structural Biology at the «Institut de Minéralogie et de Physique des Milieux Condensés»

Most regulation mechanisms of living organisms occur at molecular level through large molecular assemblies. Such "molecular machines" are usually in the range of 10 to 100 nanometers scale and their architecture can be studied by cryoelectron microscopy (cryoEM) in a frozen-hydrated state. This article gives a short introduction to this field of structural biology and describes some steps of image processing techniques used in conjunction with cryoEM. For a more complete introduction to 3D cryoEM and image processing techniques we recommend the new edition of Joachim Frank's book [1].

## Introduction

Observing biological macromolecular complexes in a frozen-hydrated state has been one of the most exciting challenges of electron microscopy. Preserving biological molecules in water and putting them into the high vacuum of an electron microscope might look like a crazy idea, but when this water is frozen into a vitreous state and when the electron dose is kept to a minimal amount (sufficient to create an image, but not strong enough to destroy the sample), this approach works beautifully. However, the low signal-to-noise ratio (SNR) generated in cryoelectron microscope images imposes *a posteriori* image processing, to retrieve the structural information on the observed macromolecules. This necessity was the beginning of a strong partnership between cryoEM and image processing in structural biology of macromolecular assemblies. The present article is a short introduction to this specific field where intangible and transient biological structures are observed with minimal electron doses and later processed to compute 3D averaged structures.

## Preparation of Biological Samples

### Freezing in vitreous ice

Beam damage was observed since early days on electron sensitive samples and biological specimens under the electron beam [2-6]. The ideas of using higher voltage [7], lower

electron dose [8] and of freezing the specimen [9, 10] to prevent propagation of unstable chemical species were proposed successively. However, the spreading of cryoelectron microscopy occurred when vitreous ice was obtained and observed in an electron microscope [11-13], and when biological objects such as a water suspension of viruses could be observed [14]. For review see [15].

The easiest way to produce amorphous ice at normal atmospheric pressure is to make a thin water layer (typically 60 to 100 nanometers), and to freeze it below -156°C as fast as possible. The plunging apparatus shown in **Fig. 1** was designed by Marc Adrian to prepare vitreous ice, using liquid ethane as cryogen. Ethane is used here as the large gap ( $\Delta=94.7^\circ\text{C}$ ) between its melting ( $-183.45^\circ\text{C}$ ) and evaporating ( $-88.75^\circ\text{C}$ ) temperatures allows the absorption of heat from the sample without formation of vapors. Indeed, evaporation prevents a good contact and a fast heat exchange with the sample (Leidenfrost effect). This is the case of liquid nitrogen which is used throughout the process to keep instruments and frozen samples cooled. At atmospheric pressure, liquid nitrogen has a very small gap ( $\Delta=14.2^\circ\text{C}$ ) between its melting ( $-210.05^\circ\text{C}$ ) and evaporating ( $-195.85^\circ\text{C}$ ) temperatures, inducing a strong Leidenfrost effect. This explains why nitrogen cannot be used under normal atmospheric conditions as an efficient cryogen. As visible in **Figs. 1b-d**, a simple Styrofoam box partially filled with liquid ethane is used to create a cooling chamber, and the central metal cup is filled with liquid ethane. In fact the metal cup has two cylindrical walls with a small gap in between, to slow down the cooling from outer liquid nitrogen. Therefore, one has enough time to flow

I.M.P.M.C., UMR 7590 CNRS, Universities P6, P7, and IPGP, 4 Place Jussieu, case postale 115 - 75252 Paris cedex 05, France  
E-mail: Nicolas.Boisset@impmcjussieu.fr



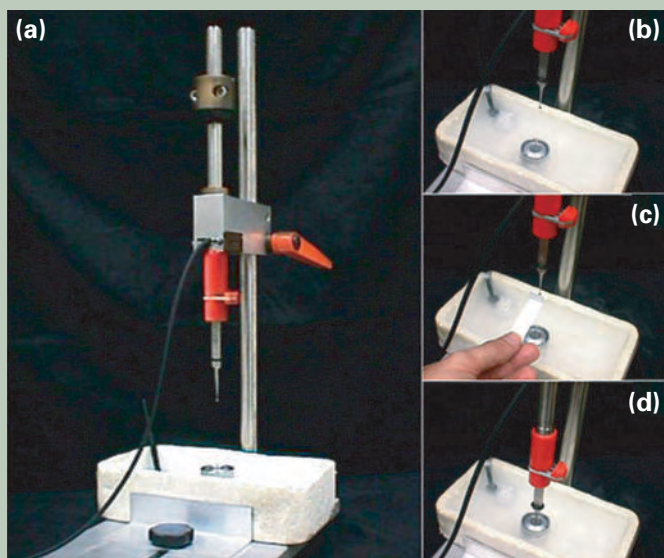


**Fig. 1** Plunging device designed by Marc Adrian for rapid freezing of sample solutions. (a) A grid on tweezers is maintained by the plunger just above a double-layered metal cup containing liquid ethane. The cup is itself within a Styrofoam box containing liquid nitrogen. (b) A 4  $\mu\text{l}$  droplet of sample solution is put on the holey-carbon grid. (c) The excess of solution is removed by applying a blotting paper on one side of the grid. (d) Rapid plunging of the grid within the liquid ethane cup rapidly freezes the thin water layer remaining within holes of the holey-carbon film. Then, the frozen sample is transferred to liquid nitrogen.

gaseous ethane, let it liquefy in the inner cup, and freeze one or two grids before the ethane starts to solidify. Flowing more gaseous ethane in the central cup provides enough heat to melt the frozen ethane and freeze additional grids. The freezing process in itself is very simple. A copper 200-400 mesh grid covered with a holey carbon film is placed on the plunger a few centimeters above the metal cups (**Fig. 1a**). A droplet of 4  $\mu\text{l}$  of sample solution is then applied on the side of the grid facing the operator (**Fig. 1b**), and a filter paper is used by the operator to remove the excess of solution (**Fig. 1c**). This so called “blotting” is crucial to form the thin liquid layer of water within the holes of the holey carbon film, and it is followed by a rapid plunging in the liquid ethane cup to vitrify the sample (**Fig. 1d**). Once frozen, the grid is rapidly transferred from liquid ethane to liquid nitrogen, where it remains until observation in the electron microscope. This remarkably efficient method was mainly designed by Marc Adrian and colleagues [15], and is still under investigation, using stroboscopic photography to evaluate how fast water vitrification occurs on the grid [16]. An other point concerns the strong evaporation of water during the split second between blotting and freezing, producing local temperature drop down before freezing and salt concentration effects that can be problematic when observing ionic strength sensitive molecular assemblies like microtubules [17], lipid vesicles [18] or DNA [19, 20]. For such samples and for time-resolved cryoelectron microscopy, more sophisticated plunging devices were designed with controlled temperature and humidity, [21-23], and with caged molecules [24, 25] or computer controlled-spraying devices [26].

### Preventing contamination and keeping the electron dose to a minimum

The role of a cryoholder and of the cold stage is to keep the frozen-hydrated sample in its vitreous state in the microscope and to limit water sublimation under the electron beam. For review see [27]. A cold metal plate or box is also placed in the microscope close the specimen to act as a cold trap and prevent contamination of the grid during observation [28]. Many cold stages and cryotransfer system were designed for transmission electron microscopy including helium cooled stages [29, 30] providing very impressive results. In **Fig. 2**, the simpler case of a nitrogen-cooled side-entry cryoholder is shown before (**Fig. 2b**) and after insertion in the electron microscope, a JEOL JEM-2100F (**Figs. 2a, c**). Once in the microscope, the electron dose is kept to a minimum level to prevent sample damage. For this purpose, the new Minimal Dose System (MDS) allows the rapid beam blanking and switching between three observation modes (**Fig. 3**). A first mode corresponds to a low magnification close to  $\times 2,000$  (**Fig. 3a**) and allows the rapid screening of a grid. Within one grid square, the holey carbon film presents many holes, some of which are empty, or with too thick ice or with good ice thickness but presenting cracks (**Fig. 3b, arrows**). Once a good hole is detected, the observer switches to the focus mode, corresponding to a higher magnification (close to  $\times 120,000$ ), and with a deflected and shifted beam less than two microns away from the zone of interest. The beam deflection can be rotationally modified in order to hit a zone corresponding to some carbon on the side of the



**Fig. 2** Sample transfer to the electron microscope. (a) Side-entry Gatan 626 cryoholder inserted in goniometer of a JEOL JEM-2100F electron microscope. The sample stage of the microscope is nitrogen cooled (arrow), to prevent contamination. (b) cryo-transfer station, with cryoholder Gatan 626 inserted in the transfer chamber. Such device allows the positioning of the grid on the tip of the cryoholder under liquid nitrogen. The Dewar of the cryoholder is also filled with liquid nitrogen to maintain the sample cooled, even during the insertion of the cryoholder in the electron microscope. (c) Close view of the cryoholder once inserted into the electron microscope.

hole (**Fig. 3c**). There, the observer can find the focus, even if the ice is totally blown up by the electron beam. Finally, the Photoset mode corresponds to an automatic sequence of beam blanking, suppression of beam tilt and shift (to hit the selected zone of interest), and film exposing for a limited amount of time at a magnification close to  $\times 50,000$ . The whole purpose of the MDS is to limit to a strict minimum the exposure under the electron beam of the zone of interest. Even if it is always difficult to measure the electron dose hitting the sample, we try to keep it between 10 and 20 electrons per  $\text{\AA}^2$ .

### Biological objects observed in cryoelectron microscopy

Many biological objects can benefit from cryoelectron microscopy. Among these, lipid vesicles are easy to observe (**Fig. 4a**) and can be used to check environmental freezing conditions. When a strong evaporation induces salt concentration, the vesicles loose their smooth spherical shapes. As shown in **Fig. 4b**, lipid membranes produce a typical double black line separated by a white  $\sim 7$  nm white gap that corresponds to the aliphatic chains of the lipids (schematic representation). Another type of macromolecule that can be imaged by cryoelectron microscopy is DNA. For example, small super-coiled DNA plasmids can be imaged in three dimensions, using the stereopair technique [31]. For this, the same field is imaged twice, with the specimen grid tilted by  $+15^\circ$  and  $-15^\circ$ , respectively (**Fig. 4c**). One can see in these two image fields three plasmids clearly individualized along a diagonal starting from the upper-left to lower-right corner of the field. Even though they look quite similar,

these two images contain enough information to compute the outer shape of DNA in three-dimensions [32]. The three modeled DNA circles appear in wire representation at the forefront of Fig. 4c. Finally, large complexes such as the Tobacco Mosaic Virus (TMV) are widely used as test macromolecular assemblies for cryoelectron microscopy techniques. The 23 Å pitch of these helical structures are clearly visible at the outer edges of the tubes (Fig. 4d) and produce a strong unmistakable layer line when imaging the power spectrum of such image. Therefore, TMV is often mixed in small quantities within other biological sample preparations, as it provides an internal reference to accurately calibrate the magnification of the microscope. Moreover, if TMV is poorly imaged in a given cryoEM grid, there is a good chance that other biological samples will be even less visible. Therefore, getting reproducibly good images of TMV in vitreous ice is a good quality check when practicing cryoelectron microscopy. Finally, TMV is also used for testing new sample preparation techniques. For example, Fig. 4e shows a field of TMV prepared with the cryonegative staining technique designed by Marc Adrian [33]. In this technique, a saturated ammonium molybdate solution is used as contrasting agent and mixed with the sample solution before blotting and plunging the grid into liquid ethane. Although, this technique rises some questioning about respective contribution of amplitude and phase contrasts involved in the image formation, it greatly enhances the contrast and allows the observation of small macromolecular complexes (300 kDa and smaller), that would otherwise be difficult to see in vitreous ice.

## Image Processing

Cryoelectron microscopy of macromolecular complexes is often used in conjunction with image processing. This grouping of techniques results from the low contrast (absence of heavy metal staining) and from the low signal-to-noise ratio (low electron dose) of cryoelectron microscope images. In fact, image processing, by computing 2D and 3D average maps from a series of low dose images of similar complexes, regains a strong signal to noise ratio without destroying biological samples with a higher electron dose. The strategies of single particle 3D reconstruction depend on the homogeneity of the complexes, on their internal symmetries, and on their ability to produce all possible orientations within the vitreous ice layer. For review on image processing techniques see the new edition of Joachim Frank's book [1], the review of Marin van Heel [34], and two special issues of the Journal of Structural Biology [35] and [36].

## Strategies for single particles

There are numerous image processing software's devoted to single particle analysis, such as IMAGIC [37], EMAN [38], XMIPP [39, 40], FREALIGN [41] etc... It would be impossible to quote all of them here, and we therefore restrict this section to the description of one 3D reconstruction method called the "random conical tilt series" developed by Michael Radermacher [42, 43] within the SPIDER software [44]. In this particular program, each experimental image is considered as the 2D

projection of a single object in a specific direction characterized by a set of three Eulerian angles (Fig. 5a). Depending on software's, angular conventions change but the main idea remains the same. Once digitized and boxed into a fixed frame, each experimental cryoEM image of a single particle is characterized by a set of five parameters: (X-shift and Y-shift) necessary to center the particle within the defined frame, and (three Eulerian angles  $\varphi$ ,  $\theta$ ,  $\psi$ ) defining the direction of projection of the particle in all possible orientations. Once these five parameters are known for a sufficient number of experimental images corresponding to as many different directions of projection, a 3D map is computed. In Fig. 5b, the random conical tilt series 3D reconstruction method is illustrated on a small phantom head. First, several copies of the phantom head are disposed in a "standing-up" orientation on a support plane, and 2D projection images are produced when the support plane is tilted by 0° and 45° (Fig. 5b, left). A similar set of images is obtained in experimental conditions when the specimen grid is tilted in the electron microscope. The 0° images are identical with each other except for in-plane rotations, while 45° images correspond to a conical tilt series (Fig. 5b, middle). If one would try to visualize the 3D Fourier transform of the phantom head, the conical tilt series would correspond to a series of centered disks orthogonally oriented with respect to their direction of projection (Fig. 5b, right). Figure 5c shows an application of this technique on a large respiratory pigment, the hemocyanin of the snail *Helix Pomatia* [45]. In the upper part of Fig. 5c the same specimen field is imaged twice with tilt angles of 45° and 0°, respectively. After digitization, pairs of tilted- and untilted-specimen images are interactively selected, using the WEB display program (white circles) [44]. At this stage the locations of particles in both specimen fields provide a mean for computing the tilt angle ( $\theta$ ) and the in-plane direction of tilt axis ( $\psi$ ). A series of 0° and 45° image pairs is shown in Fig. 5c, lower-left part. While 45° images change according to a conical tilt geometry, 0° images are all identical except for an in-plane rotation corresponding to the last Eulerian angle ( $\varphi$ ). At this stage, after a centering procedure, the tilted-specimen images are used to compute the 3D reconstruction volume of the particle (Fig. 5c, lower right).

## Correcting the contrast transfer function of the microscope

Dialogue between physicists and biologists about contrast transfer function (CTF) and its correction can be misleading. In fact this comes from the fact that we are not speaking of the same type of contrast and we are not using the same defocus ranges. As most of the contrast in a cryoEM images comes from the phase contrast, one has to make a compromise between defocus and visibility of isolated particles in the ice layer. While in material sciences a reasonable defocus is close to Scherzer, in cryoEM most people use defocus values 10 to 100 times bigger to produce enough contrast. The price to pay for this is that the CTF oscillates far more and even in low spatial frequencies. Figure 6 provides a crude description of the situation for a frozen-

hydrated sample, and the strategy used for CTF correction using the Wiener filtering approach. More accurate descriptions and strategies are available in [46-48].

While in real space one must consider that the true image of an object is convoluted by the point spread function of the microscope, in reciprocal space, the Fourier transform of the true image is multiplied by the CTF. Such effect is represented in Figure 6a, where the Fourier transformed true image of a little frog is multiplied in reciprocal space by a CTF corresponding to a first low defocus and to a second stronger defocus. One can see that with the first defocus the contrast is weak but small structural details are visible. Conversely, a higher defocus provides a better overall contrast but small structural details are blurred.

As shown at the top of Fig. 6b, the radial profile of the CTF1 plotting the contrast as the function of spatial frequencies (defocus 1) oscillates less than the radial profile of CTF2 (defocus 2). In these conditions, the experimental image obtained with defocus 2 crosses the horizontal line (contrast equal to zero) three times, at spatial frequencies of  $1/16\text{Å}^{-1}$ ,  $1/11\text{Å}^{-1}$ , and  $1/9\text{Å}^{-1}$ . For these spatial frequencies the signal is lost and only noise remains. Therefore, Wiener filtering was proposed to selectively regain signal from experimental images and to mimic images produced by a "perfect instrument" (CTF equal to 1 for all spatial frequencies). Radial profiles of Wiener filters 1 and 2 are designed to counterbalance oscillations of CTF1 and CTF2, respectively. These filters are also designed to keep the contrast low at spatial frequencies where contrast mainly comes from the noise. The CTF corrected average image obtained after Wiener filtering and mixing of experimental images 1 and 2 is shown in Fig. 6b. Even though this image resembles the true image of the object (Fig. 6a, right), there are still some local differences. This is understandable when looking at the radial profile of the corrected CTF function (Fig. 6b, lower right). Clearly this profile is not perfectly corrected for spatial frequency  $1/11\text{Å}^{-1}$ . However, when looking at overlapped original CTF profiles (Fig. 6b, lower left), it becomes clear that at this spatial frequency both CTF are equal to zero and therefore both images only contained noise.

## Impact of structural heterogeneity

The giant hemoglobin of the earth worm *Lumbricus terrestris* is a good example of macromolecular complex with a high molecular weight (~3 MDa). It consists of 144 globin chains packed into twelve dodecameric blocks by 36 linker chains. In the ice layer complexes are observed in all possible orientations (Fig. 7a), and after alignment and sorting, three typical top and side views (Fig. 7b) show the dodecameric units gathered in a hexagonal bilayer structure (Fig. 7c). The 3D reconstruction volume was computed with a 14.9 Å resolution, using the Wiener filtering approach for CTF correction [49]. Such large respiratory pigments are easy to reconstruct as they are structurally homogeneous. The few partially degraded complexes are easy to point out and to discard from the treatments. Conversely, for other complexes showing strong shape diversity, it is almost impossible to compute a 3D map. However, image processing of such het-

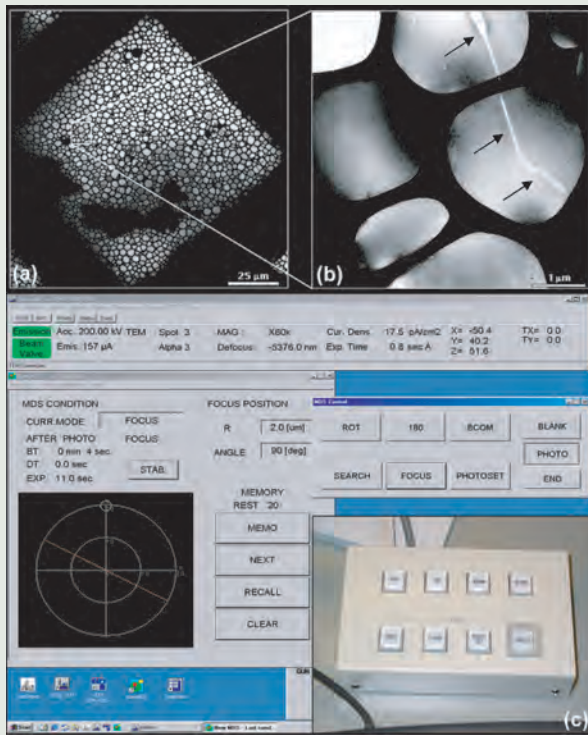


Fig. 3 Minimal dose system for recording cryo-electron microscope images. (a) Square grid of a holey carbon film observed at low magnification in "search" mode. (b) Enlarged detail of a portion of image (a) showing the ice layer within the holes of the carbon film. Holes showing defects (no ice, ice too thick, or ice with cracks) are not chosen, while other holes containing thin vitreous ice are selected for photography. (c) MDS display.

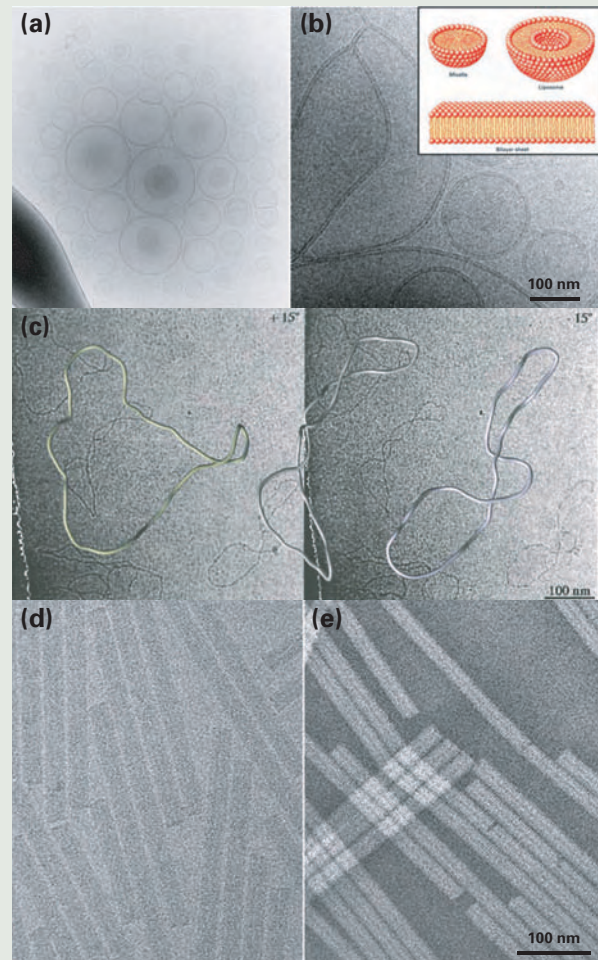


Fig. 4 Examples of biological macromolecular objects imaged by cryo-electron microscopy. (a) Lipid vesicles. (b) Visualization of the double layer of the lipid membrane as two parallel back lines separated by a white 7 nm spacing. (c) Stereo pairs of DNA circular plasmids. The same field is imaged twice with +15° and -15° tilt angles, allowing the 3D reconstruction of its outer contour (yellow wire models) [31, 32]. (d) Typical cryo-electron microscope view of Tobacco Mosaic virus with its 23 Å pitch. (e) Similar TMV sample imaged by the cryo-negative staining technique of Marc Adrian, using a saturated solution of ammonium molybdate as staining agent [33].

erogeneous samples can still provide meaningful information. A good example is the case of MalT, a transcriptional activator of the maltose regulon in *Escherichia coli*. This (~100 kDa) transcriptional activators self-associates in elongated oligomers with the DNA maltose regulon, in the presence of ATP and maltotriose (Figs. 7d-e). Image processing highlighted the significant conformational flexibility of these polymeric forms and allowed us to propose a model of functional activation of the gene based on MalT binding to the target DNA promoters [50].

### Impact of internal symmetries

Image processing strategies tend to use internal symmetries of the particles to take advantage of signal redundancy during the computation of 3D volumes. Virus capsids with helical and icosahedral symmetries repre-

sent particular cases and specific packages were developed to take advantages of their respective properties (for review on image processing packages see [35], and [36]). An example of icosahedral virus is the Tomato Bushy Stunt Virus (TBSV) (Fig. 8) present in compact (Fig. 8a) and swollen (Fig. 8b) conformations. When observing the 3D reconstruction volume of compact TBSV, the 180 copies of the protein forming the capsid are clearly visible (Fig. 8c), while inner RNA which does not follow icosahedral symmetry produces a non-descriptive spherical density distribution (Fig. 8d). Atomic coordinates of capsid protein [51] can be fitted on the compact cryoEM volume [34] (Fig. 8e), and the swelling process can be imaged by superposing compact and swollen 3D reconstruction volumes (Fig. 8f) and by hybrid approach using combined experiments with small angle X-ray scattering [52].

### Conclusion

Cryo-electron microscopy combined with image processing is an efficient tool for structural biology study of macromolecular assemblies. For some highly homogeneous and symmetrically redundant samples, resolutions below 6 Å are obtained [53-56]. However, for most single particles sub-nanometric resolution is enough to fit alpha helices, and can be obtained using CCD cameras and automation of cryoEM observations [57, 58]. Presently, the European network "3D-EM" is promoting the development of standard procedures for high resolution image processing. This network is also contributing through the work of Kim Henrick and E. B. I. (<http://www.ebi.ac.uk/>) to the development of the Electron Microscopy Data Base (<http://www.ebi.ac.uk/msd/index.html>) [59]. This bank will keep and make available the tremendous amount of

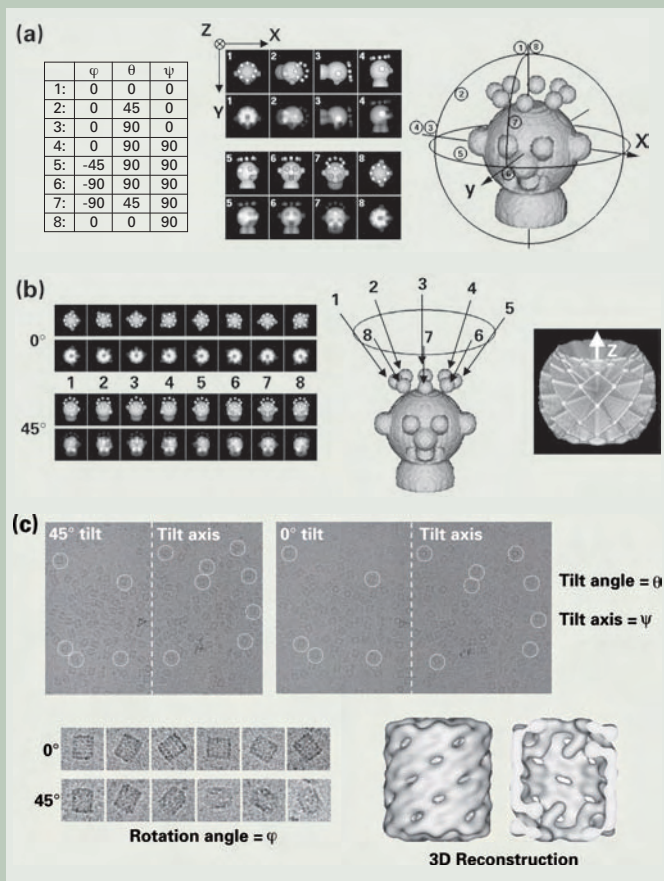


Fig. 5 The random conical tilt series 3D reconstruction technique of Michael Radermacher [42, 43]. (a) Conventions of Eulerian angles within spider software [44], where  $\varphi$  = first rotation around axis Z (before tilting),  $\theta$  = rotation around axis Y (tilting of specimen grid),  $\psi$  = final rotation around Z (after tilting). (b) Conical tilt geometry in real space and in reciprocal space according to the central projection theorem. (c) Example of a random conical tilt series 3D reconstruction of the hemocyanin of Burgundy snail *Helix pomatia* [45].

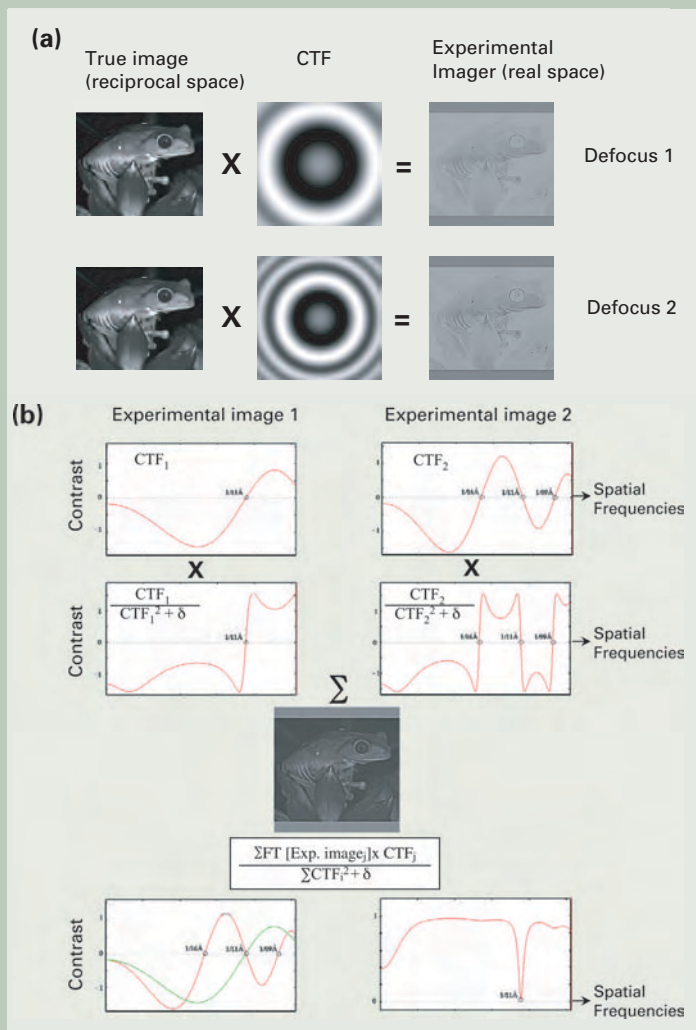


Fig. 6 Correcting CTF with the Wiener filtering approach: (a) Schematic representation of the effect of CTF when multiplied in reciprocal space with the Fourier transform of a frog image to mimic a cryoEM image at two different defoci. (b) For the two defoci, radial profiles of the CTFs are plotted as a function of spatial frequencies, with the corresponding Wiener filter. Then the CTF corrected Frog image is obtained with a new contrast function close to 1 except for spatial frequency  $1/11\text{\AA}^{-1}$ , where both original CTF curves are simultaneously close to zero.

information gained through 3D cryoEM to the structural biology community.

## Acknowledgements

The authors are grateful to the support of European commission through European network of excellence "3D-EM" contract N° LSHG-CT-2004-502828.

## References

- [1] J. Frank, Three-dimensional Electron Microscopy of Macromolecular Assemblies - Visualization of Biological Molecules in Their Native State., Oxford University Press, New York, (2005),
- [2] L. Reimer, Quantitative Electron Microscopy, Williams & Wilkins, (1965), 344
- [3] R. M. Glaeser, *J. Ultrastruct Res*, **36**, 466, (1971)
- [4] R. M. Glaeser and L. W. Hobbs, *J. Microsc*, **103**, 209, (1975)
- [5] M. Isaacson, *et al.*, *Radiat Res*, **55**, 205, (1973)
- [6] R. E. Thach and S. S. Thach, *Biophys J.*, **11**, 204, (1971)
- [7] K. Kobayashi and K. Sakaoku, Quantitative Electron Microscopy, Williams & Wilkins, (1965), 359
- [8] I. A. Kuo and R. M. Glaeser, *Ultramicroscopy*, **1**, 53, (1975)
- [9] E. Knapek and J. Dubochet, *J. Mol Biol.*, **141**, 147, (1980)
- [10] K. A. Taylor and R. M. Glaeser, *J. Ultrastruct Res*, **55**, 448, (1976)
- [11] J. Dubochet and A. W. McDowell, *J. Microsc.*, **124**, 3, (1981)
- [12] J. Dubochet, *et al.*, *J. Microsc.*, **128**, 219, (1982)
- [13] J. Dubochet, *et al.*, *Cryo-Letters*, **4**, 233, (1983)
- [14] M. Adrian, *et al.*, *Nature*, **308**, 32, (1984)
- [15] J. Dubochet, *et al.*, *Q Rev Biophys*, **21**, 129, (1988)
- [16] S. Kasas, *et al.*, *J. Microsc.*, **211**, 48, (2003)
- [17] R. H. Wade and D. Chretien, *J. Struct Biol.*, **110**, 1, (1993)
- [18] P. M. Frederik and D. H. Hubert, *Methods Enzymol.*, **391**, 431, (2005)
- [19] J. Bednar, *et al.*, *J. Cell Biol.*, **131**, 1365, (1995)
- [20] J. Dubochet, *et al.*, *Methods Enzymol.*, **211**, 507, (1992)
- [21] H. D. White, *et al.*, *J. Struct Biol.*, **121**, 306, (1998)
- [22] J. F. Menetret, *et al.*, *J. Mol Biol.*, **219**, 139, (1991)
- [23] Y. Talmon, *et al.*, *J Electron Microscop Tech.*, **14**, 6, (1990)
- [24] T. Funatsu, *et al.*, *J. Cell Biol.*, **121**, 1053, (1993)
- [25] K. Hirose, *et al.*, *Biophys J.*, **65**, 397, (1993)
- [26] J. Berriman and N. Unwin, *Ultramicroscopy*, **56**, 241, (1994)
- [27] A. W. Robards and U. B. Sleytr, Low Temperature Methods in Biological

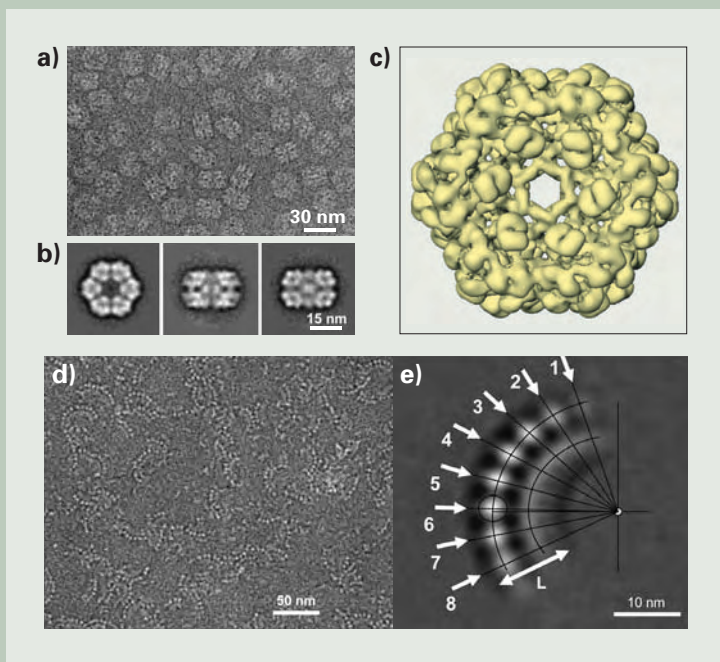


Fig. 7 Examples of single particles: (a) Giant hemoglobin from *Lumbricus terrestris* observed in a JEOL JEM-2010F electron microscope at 200 kV, and under low electron dose conditions. (b) Selected 2D average maps of hexagonal top views and rectangular bilayered side views. (c) Reconstruction volume at 14.9 Å resolution obtained after CTF correction using the Wiener filtering approach [49]. (d) Oligomeric assemblies of MalT transcriptional activator complexed with DNA primers. (e) Average 2D map obtained from image processing and automatic classification of heterogeneous oligomeric forms.

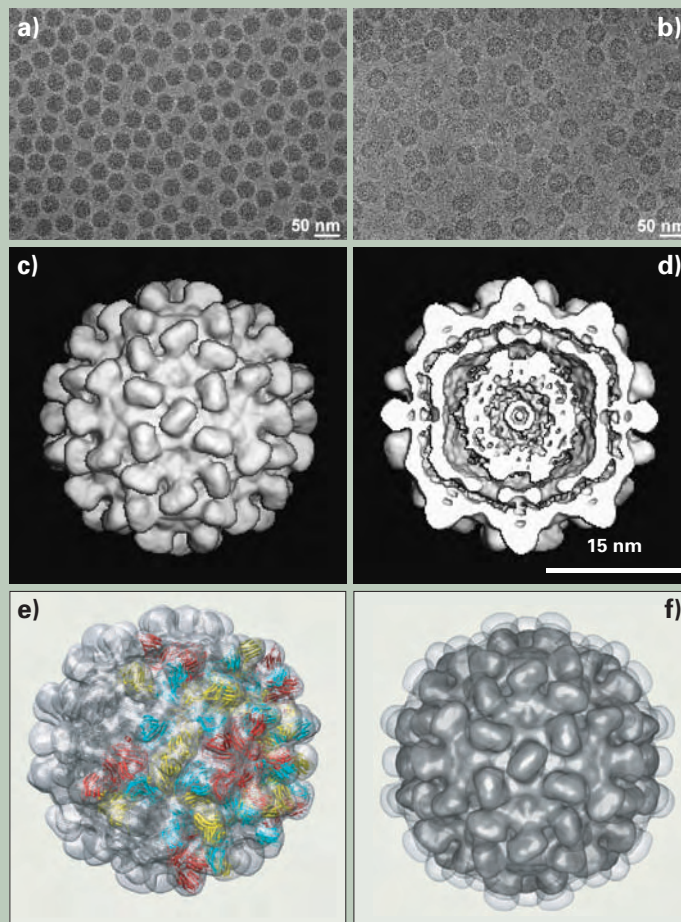


Fig. 8 The swelling of Tomato Bushy Stunt Virus (TBSV): (a) TBSV in its compact conformation observed on a JEOL JEM-2010F with an acceleration voltage of 200 kV with the MDS system. (b) TBSV in its swollen conformation after pH modification from 6.5 to 7.4 and calcium removal using EDTA as chelating agent. (c) Reconstruction volume of compact TBSV at 13 Å resolution. (d) Same volume as (c) but after removing the front half to see inner features and RNA radial location. (e) Fitting of atomic structures of capsid proteins on the 3D cryoEM maps. (f) Surface rendering of the compact (dark grey) and the swollen (semi-transparent) TBSV 3D cryoEM maps.

- Electron Microscopy., Elsevier, Amsterdam, New York, Oxford., (1985),
- [28] J. C. Homo, et al., *J. Microsc.*, **136**, 337., (1984)
- [29] F. Zemlin, et al., *Science*, **229**, 461, (1985)
- [30] Y. Fujiyoshi, *Adv Biophys.*, **35**, 25, (1998)
- [31] I. Dustin, et al., *J. Struct Biol.*, **107**, 15, (1991)
- [32] E. Larquet, et al., *J. Biomolec. Struct. Dynamics*, **12**, a134, (1995)
- [33] M. Adrian, et al., *Micron.*, **29**, 145, (1998)
- [34] M. van Heel, et al., *Q Rev Biophys.*, **33**, 307, (2000)
- [35] B. Carragher and P. R. Smith, *J. Struct. Biol.*, **116**, 2, (1996)
- [36] B. Carragher and P. Penczek, *J. Struct. Biol.*, **144**, 1, (2003)
- [37] M. van Heel, et al., *J. Struct Biol.*, **116**, 17, (1996)
- [38] S. J. Ludtke, et al., *J. Struct Biol.*, **128**, 82, (1999)
- [39] C. O. Sorzano, et al., *J. Struct Biol.*, **148**, 194, (2004)
- [40] R. Marabini, et al., *J. Struct Biol.*, **116**, 237, (1996)
- [41] A. Stewart and N. Grigorieff, *Ultramicroscopy*, **102**, 67, (2004)
- [42] M. Radermacher, et al., *J. Microsc.*, **146** (Pt 2), 113, (1987)
- [43] M. Radermacher, *J. Electron Microsc. Tech.*, **9**, 359, (1988)
- [44] J. Frank, et al., *J. Struct Biol.*, **116**, 190, (1996)
- [45] O. Lambert, et al., *J. Mol Biol.*, **248**, 431, (1995)
- [46] Z. Huang, et al., *J. Struct Biol.*, **144**, 79, (2003)
- [47] J. A. Velazquez-Muriel, et al., *Ultramicroscopy*, **96**, 17, (2003)
- [48] S. J. Ludtke, et al., *Structure (Camb)*, **12**, 1129, (2004)
- [49] F. Mouche, et al., *J. Struct Biol.*, **133**, 176, (2001)
- [50] E. Larquet, et al., *J. Mol Biol.*, **343**, 1159, (2004)
- [51] C. Chauvin, et al., *J. Mol. Biol.*, **124**, 641, (1978)
- [52] R. Aramayo, et al., *Biochim. Biophys. Acta*, (in press). (2005)
- [53] A. Miyazawa, et al., *J. Mol Biol.*, **288**, 765, (1999)
- [54] K. Yonekura, et al., *Nature*, **424**, 643, (2003)
- [55] F. A. Samatey, et al., *Nature*, **431**, 1062, (2004)
- [56] A. Fotin, et al., *Nature*, **432**, 573, (2004)
- [57] B. Carragher, et al., *J. Struct Biol.*, **132**, 33, (2000)
- [58] C. R. Booth, et al., *J. Struct Biol.*, **147**, 116, (2004)
- [59] K. Henrick, et al., *J. Struct Biol.*, **144**, 228, (2003)

# Direct Analysis in Real Time (DART<sup>™</sup>) Mass Spectrometry

Robert B. Cody<sup>†</sup>, James A. Laramée<sup>††</sup>,  
J. Michael Nilles<sup>†††</sup>, and H. Dupont Durst<sup>††††</sup>

<sup>†</sup>JEOL USA, Inc.

<sup>††</sup>EAI Corporation

<sup>†††</sup>Geo-Centers Inc.

<sup>††††</sup>Edgewood Chemical Biological Center

## Introduction

Mass Spectrometry (MS) is one of the fastest-growing areas in analytical instrumentation. The use of mass spectrometry in support of synthetic, organic, and pharmaceutical chemistry is well established. Mass spectrometry is also used in materials science, environmental research, and forensic chemistry. It has also evolved into one of the core methods used in biotechnology. However, currently available ion sources place extreme restrictions on the speed and convenience of sample analysis by mass spectrometry. Here we report a method for using mass spectrometry to instantaneously analyze gases, liquids, and solids in open air at ground potential under ambient conditions.

Traditional ion sources used in mass spectrometry require the introduction of samples into a high vacuum system. Traditional ion sources operated in vacuum include electron ionization (EI)[1], chemical ionization (CI)[2], fast atom bombardment (FAB)[3], and field desorption/field ionization (FD/FI)[4]. These techniques have been used successfully for decades. However, the requirement that samples be introduced into a high vacuum for analysis is a severe limitation. Gas or liquid samples must be introduced through a gas chromatograph or a specially designed inlet system. Solid samples must be introduced by using a direct insertion probe and a vacuum lock system. Direct insertion probes can result in vacuum failure and/or contamination of the

ion source if too much sample is introduced.

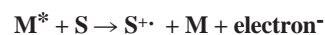
Atmospheric pressure ion sources such as atmospheric pressure chemical ionization (APCI)[5], electrospray ionization (ESI)[6-8], matrix-assisted laser desorption ionization (MALDI)[9-10] and atmospheric pressure photoionization (APPI)[11] have broadened the range of compounds that can be analyzed by mass spectrometry. However, these ion sources require that samples be exposed to elevated temperatures and electrical potentials, ultraviolet irradiation, laser radiation, or a high-velocity gas stream. Safety considerations require that the ion source be fully enclosed to protect the operator from harm.

The new ion source reported herein overcomes these limitations. The new technique, referred to as Direct Analysis in Real Time (DART<sup>™</sup>), has been coupled to the AccuTOF-LC<sup>™</sup> atmospheric pressure ionization mass spectrometer to permit high-resolution, exact mass measurements of gases, liquids, and solids[12,13]. DART successfully sampled hundreds of chemicals, including chemical agents and their signatures, pharmaceuticals, metabolites, pesticides and environmentally significant compounds, peptides and oligosaccharides, synthetic organics, organometallics, drugs of abuse, explosives, and toxic industrial chemicals. These chemicals were detected on a variety of surfaces such as concrete, human skin, currency, airline boarding passes, fruits and vegetables, body fluids, cocktail glasses, and clothing. The composition of drug capsules and tablets was directly analyzed.

sources used in hand-held detectors for chemical weapons agents (CWAs), drugs, and explosives. The discovery that DART could be used for positive-ion and negative-ion non-contact detection of materials on surfaces, as well as for detection of gases and liquids, led to the development of a commercial product.

DART is based on the atmospheric pressure interactions of long-lived electronic excited-state atoms or vibronic excited-state molecules with the sample and atmospheric gases. The DART ion source is shown in **Figure 1**. A gas (typically helium or nitrogen) flows through a chamber where an electrical discharge produces ions, electrons, and excited-state (metastable) atoms and molecules. Most of the charged particles are removed as the gas passes through perforated lenses or grids and only the neutral gas molecules, including metastable species, remain. A perforated lens or grid at the exit of the DART provides several functions: it prevents ion-ion and ion-electron recombination, it acts as a source of electrons by surface Penning ionization, and it acts as an electrode to promote ion drift toward the orifice of the mass spectrometer's atmospheric pressure interface.

Several ionization mechanisms are possible, depending on the polarity and reaction gas, the proton affinity and ionization potential of the analyte, and the presence of additives or dopants. The simplest process is Penning ionization [14] involving transfer of energy from the excited gas M\* to an analyte S having an ionization potential lower than the energy of M\*. This produces a radical molecular cation S<sup>•+</sup> and an electron (e<sup>-</sup>).



Penning ionization is a dominant reaction mechanism when nitrogen or neon is used in the DART source. Nitrogen or neon ions are effectively removed by the electrostatic lenses and are never observed in the DART back-

## Background and Principle of Operation

DART grew out of discussions at JEOL USA, Inc. between two of the authors (Laramée and Cody) about the possibility of developing an atmospheric pressure thermal electron source to replace the radioactive

<sup>†</sup>11 Dearborn Road, Peabody, Massachusetts, USA.

<sup>††</sup>1308 Continental Drive, Suite J, Abingdon, MD 21009

<sup>†††</sup>Box 68 Gunpowder Branch, APG, MD 21010

<sup>††††</sup>Aberdeen Proving Grounds, Maryland USA

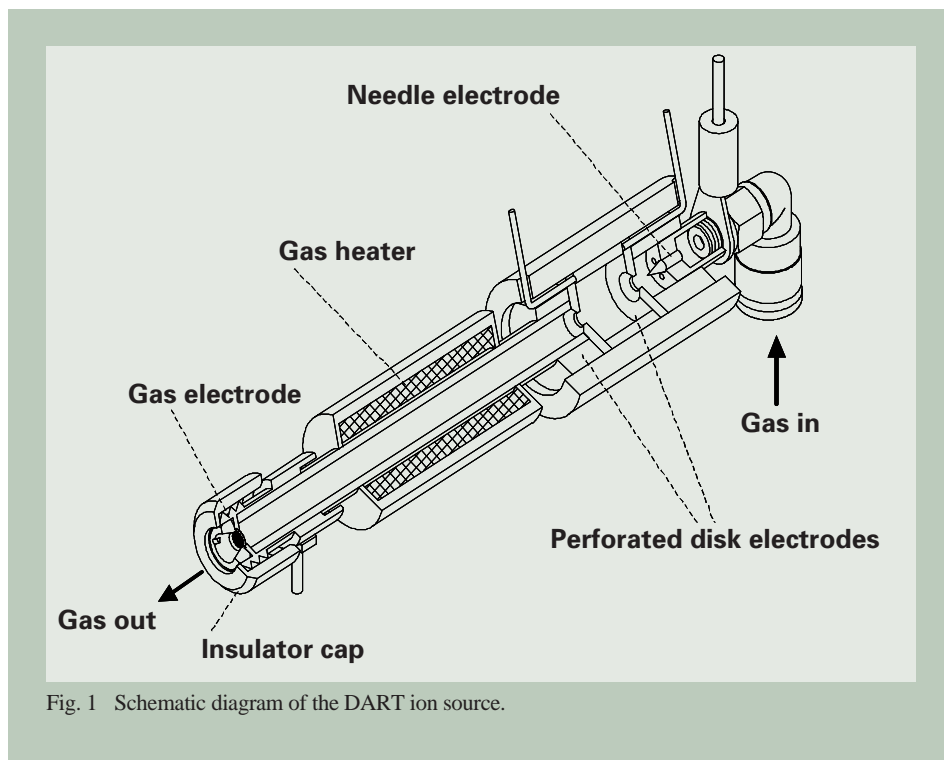
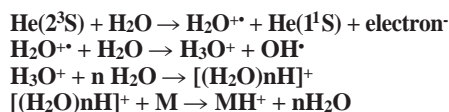


Fig. 1 Schematic diagram of the DART ion source.

ground mass spectrum.

When helium is used, the dominant positive-ion formation mechanism involves the formation of ionized water clusters followed by proton transfer reactions:



The helium  $2^3\text{S}$  state has an energy of 19.8 eV. Its reaction with water is extremely efficient [15] with the reaction cross section estimated at  $100 \text{ \AA}^2$ . Because of this extraordinarily high cross section, DART performance is not affected by humidity.

Negative-ion formation occurs by a different mechanism. Electrons ( $e^-$ ) are produced by Penning ionization or by surface Penning ionization:



These electrons are rapidly thermalized by collisions with atmospheric pressure gas



Thermal electrons undergo electron capture by atmospheric oxygen



to produce  $\text{O}_2^-$ , which reacts with the analyte to produce anions. The DART negative-ion reagent mass spectra are virtually identical for nitrogen, neon, and helium. However, negative-ion sensitivity increases for DART gases in the following order:



This is due to the increased efficiency in forming electrons by Penning ionization and

surface Penning ionization as the internal energy of the metastable species increases.

The polarity of the DART ion source is switched between positive-ion mode and negative-ion mode by changing the polarity of the disk electrode and grid. The polarity of the discharge needle is not changed, so the plasma is not interrupted. This permits rapid switching between positive and negative modes.

Other reactions are possible. The presence of traces of dopants such as ammonium (e.g. from ammonium hydroxide headspace vapor) or chloride (e.g. from methylene chloride vapor) can modify the chemistry allowing the chemist to tailor the experiment for specific analyses.

DART produces relatively simple mass spectra characterized by  $\text{M}^+$ ; and/or  $[\text{M}+\text{H}]^+$  in positive-ion mode, and  $\text{M}^-$  or  $[\text{M}-\text{H}]^-$  in negative-ion mode. Fragment ions are observed for some compounds. The degree of fragmentation can be influenced by the choice of gas, the temperature, and the AccuTOF orifice 1 potential. Alkali metal cation attachment and double-charge ions are not observed.

The mechanism involved in desorption of materials from surfaces by DART is less well characterized. Thermal desorption plays a role if the gas stream is heated. However, the analysis by DART of inorganic materials such as sodium perchlorate or organic salts having little or no vapor pressure is evidence of other processes. It is postulated that the transfer energy to the surface by metastable atoms and molecules facilitates desorption and ionization.

In contrast with other ion sources that use metastable species [16-23], the DART ion source does not operate under reduced pressure, apply a high electrical potential to the analyte, or expose the analyte directly to the discharge plasma. Argon, used in many of these ion sources, is not well suited for use with DART because argon metastables are rapidly quenched in the presence of water vapor [20] by a reaction involving homolytic

cleavage of the water bond without concomitant ion formation. None of these ion sources are designed for direct analysis of gases, liquids, and solids in open air under ambient conditions.

## Experimental

A DART<sup>tm</sup> source [24] was installed on a JEOL AccuTOF LC<sup>tm</sup> time-of-flight mass spectrometer. The DART source replaces the standard electrospray ionization (ESI) source supplied with the AccuTOF. No vacuum vent is required. The ion sources can be exchanged and made operational within minutes.

The mass spectrometer operates at a constant resolving power of approximately 6000 (FWHM definition). Typical atmospheric pressure interface conditions are: orifice 1 = 30V, and both orifice 2 and ring lens are set to 5V. The AccuTOF ion guide voltage is varied as needed depending on the lowest  $m/z$  to be measured. Orifice 1 temperature is typically kept warm (80 degrees C) to prevent contamination. Although there is some electrical potential on the exposed orifice 1, the voltage and current are so low that there is absolutely no danger to the operator, even with prolonged direct contact.

The DART source is operated with typical gas flows between 1.5 and 3 liters per minute. Gas temperature is programmable from ambient temperature up to approximately 350 degrees C (gas heater temperature from OFF to a maximum of 550 degrees C). Typical potentials are: discharge needle 2 kV to 4 kV, electrode 1: 100V, grid: 250 V. Gas, liquid, or solid samples positioned in the gap between the DART source and mass spectrometer orifice 1 are ionized.

Because the mass spectrometer orifice is continually bathed in hot inert gas, the DART source is remarkably resistant to contamination and sample carryover. Mass scale calibration is easily accomplished by placing neat poly-

ethylene glycol average molecular weight 600 (PEG 600) on a glass rod or a piece of absorbent paper in front of the DART source. In positive-ion mode, this produces a series of  $[M+H]^+$  and  $[M+H-H_2O]^+$  peaks from  $m/z$  45 up to beyond  $m/z$  1000. By including background peaks, the calibrated mass range can be extended down to  $m/z$  18 or 19. Negative-ion spectra of PEG are characterized by  $[M+O_2-H]^-$  and  $[(C_2H_4O)_n+O_2-H]^-$  ion series.

The reference spectrum can be acquired within seconds. There is no memory effect or carryover of the reference compound -- the PEG peaks do not persist after the reference standard is removed. For these reasons, a full reference mass spectrum can be quickly and easily included in each data file, and accurate mass measurements are routinely acquired for all samples.

## Applications

The DART ion source has been used to analyze an extremely wide range of analytes, including drugs (prescription, over-the-counter, veterinary, illicit, and counterfeit) in dose form or in body fluids or tissues, explosives and arson accelerants, chemical weapons agents and their signatures, synthetic organic or organometallics compounds, environmentally important compounds, inks and dyes, foods, spices and beverages. An important benefit of DART is that materials can be analyzed directly on surfaces such as glass, TLC plates, concrete, paper, or currency without requiring wipes or solvent extraction.

Drugs can be detected in pill form by placing the pill in front of the DART source for a few minutes. An example is shown below (Figure 2) for the rapid detection of illicit drugs in pills confiscated by a law-enforcement agency. The intact pills were simply placed in front of the DART source and analyte ions were observed within seconds. Exact mass and isotopic measurements confirmed the elemental compositions of the labeled components. All labeled assignments in the following examples were confirmed by exact mass measurements.

Drug counterfeiting is becoming a serious and widespread public health problem. Counterfeit drugs are not only illegal, but dangerous; they may contain little or no actual drug content, or they may contain completely different drugs with potentially toxic consequences.

DART can be used to rapidly screen for counterfeit drugs. An example is shown below in Figure 3 where DART was used to analyze a sample of a real drug containing the anti-malarial dihydroartemisinin, and a counterfeit drug containing no active ingredients.

DART has been applied to the direct detection of drugs and metabolites in raw, unprocessed body fluids, including blood, urine, perspiration, and saliva. An example is shown below in Figure 4 for the negative-ion analysis of the urine of a subject taking prescription ranitidine. No extraction or other processing was used: a glass rod was dipped in raw urine and placed in front of the DART source.

For easy viewing, only abundant components are labeled in this figure. A more complete list of assignments is given in Table 1. Assignments are made for compounds com-

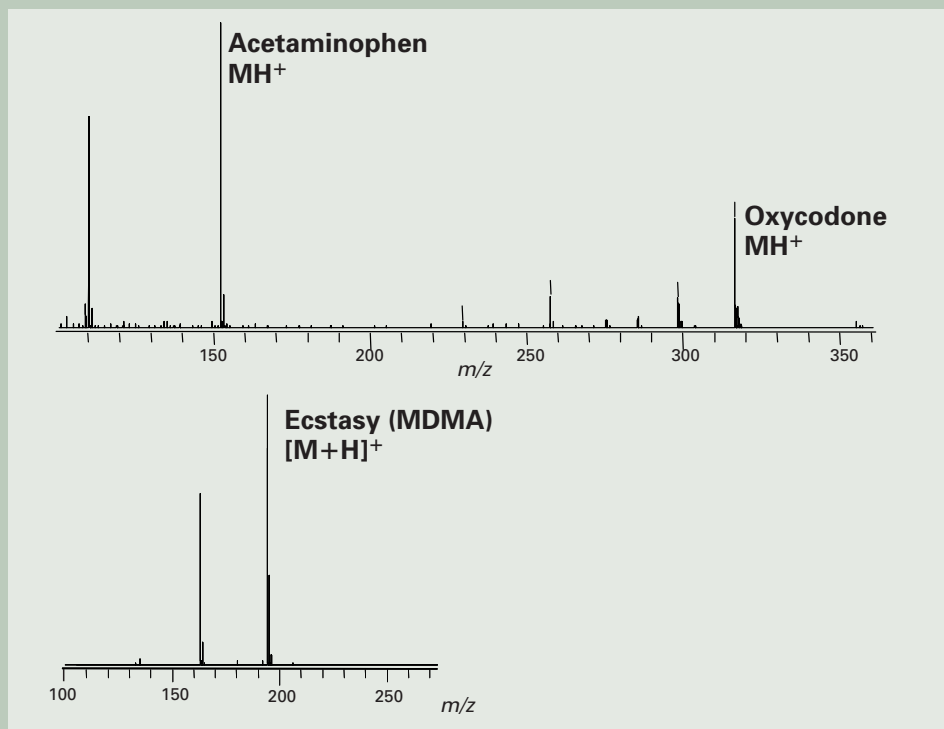


Fig. 2 DART mass spectra of two pills: An analgesic containing acetaminophen plus oxycodone (top) and methylenedioxyamphetamine ("ecstasy", bottom).

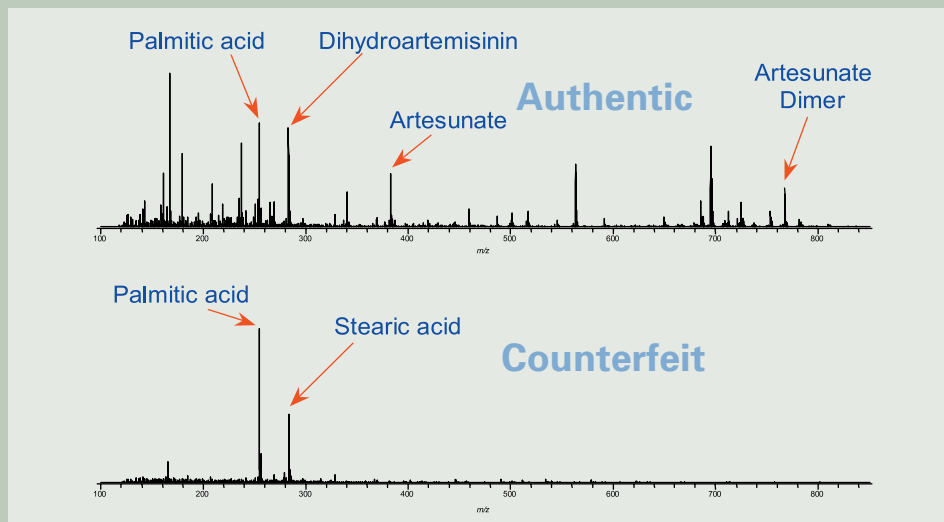


Fig. 3 Rapid detection of counterfeit drug. The top mass spectrum shows the authentic drug and the bottom mass spectrum shows the counterfeit drug.

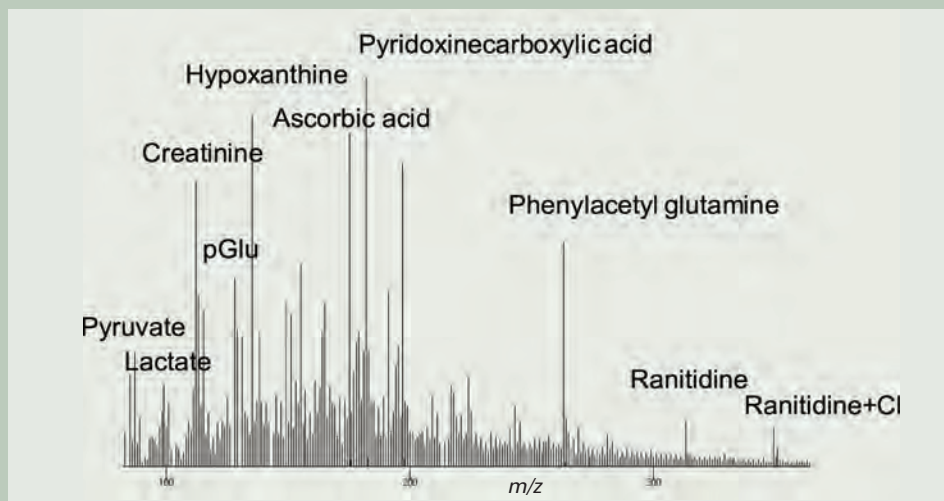


Fig. 4 Negative-ion DART analysis of the urine of a subject taking prescription ranitidine.

Table 1 Assignments for Compounds Detected in Negative-Ion DART Mass Spectrum of Raw Urine.

Name	Meas.	Calc.	Diff(u)	Abund.
GBL	85.0295	85.0290	0.0006	11.0317
Pyruvic_acid	87.0084	87.0082	0.0002	7.1700
Lactic_acid	89.0236	89.0239	-0.0002	8.3658
Cresol	107.0492	107.0497	-0.0004	.9294
Uracil	111.0153	111.0195	-0.0041	14.3328
Creatinine	112.0513	112.0511	0.0002	81.6851
Purine	119.0354	119.0358	-0.0004	31.9510
Niacin	122.0277	122.0242	0.0035	3.1489
Dihydro_methyluracil	127.0486	127.0508	-0.0021	23.3773
pGlu	128.0353	128.0348	0.0006	59.2337
Methylmaleic_acid	129.0212	129.0188	0.0024	37.1191
Me_succinate/diMe_malonate	131.0368	131.0358	0.0010	19.3593
Deoxyribose	133.0489	133.0501	-0.0012	28.3521
Hypoxanthine	135.0306	135.0307	-0.0001	100.0000
Adipic_acid	145.0469	145.0501	-0.0032	11.7389
Methyl_hypoxanthine	149.0454	149.0463	-0.0009	37.5243
Hydroxymethyl_methyl_uracil	155.0453	155.0457	-0.0003	55.5832
a-aminoadipic_acid	160.0568	160.0610	-0.0042	9.5885
Methionine_sulfoxide	164.0419	164.0381	0.0037	11.7609
Methylxanthine	165.0408	165.0412	-0.0004	32.4341
Formiminoglutamic_acid	173.0536	173.0562	-0.0027	12.3531
Ascorbic_acid	175.0285	175.0243	0.0042	23.1998
Hippuric_acid	178.0513	178.0504	0.0009	66.4487
Glucose	179.0552	179.0556	-0.0004	39.7499
Dimethylxanthine	179.0552	179.0569	-0.0017	39.7499
Pyridoxinecarboxylic_acid	182.0479	182.0453	0.0026	34.7913
Hydroxyindoleacetic_acid	190.0542	190.0504	0.0037	5.4133
Dimethyluric_acid	195.0527	195.0518	0.0009	23.7577
AAMU (caffeine metabolite)	197.0667	197.0675	-0.0007	79.6617
Cinnamalidinemalonic_acid	217.0483	217.0501	-0.0017	60.5399
AFMU (caffeine metabolite)	225.0643	225.0624	0.0019	21.9092
Cytidine	242.0801	242.0777	0.0024	3.4545
Uridine	243.0641	243.0617	0.0024	21.1156
Phenylacetyl_glutamine	263.1033	263.1032	0.0001	48.9665
Adenosine	266.0861	266.0889	-0.0028	1.4869
Ranitidine	313.1321	313.1334	-0.0013	8.7459
Ranitidine+Cl	349.1113	349.1101	0.0011	11.7296

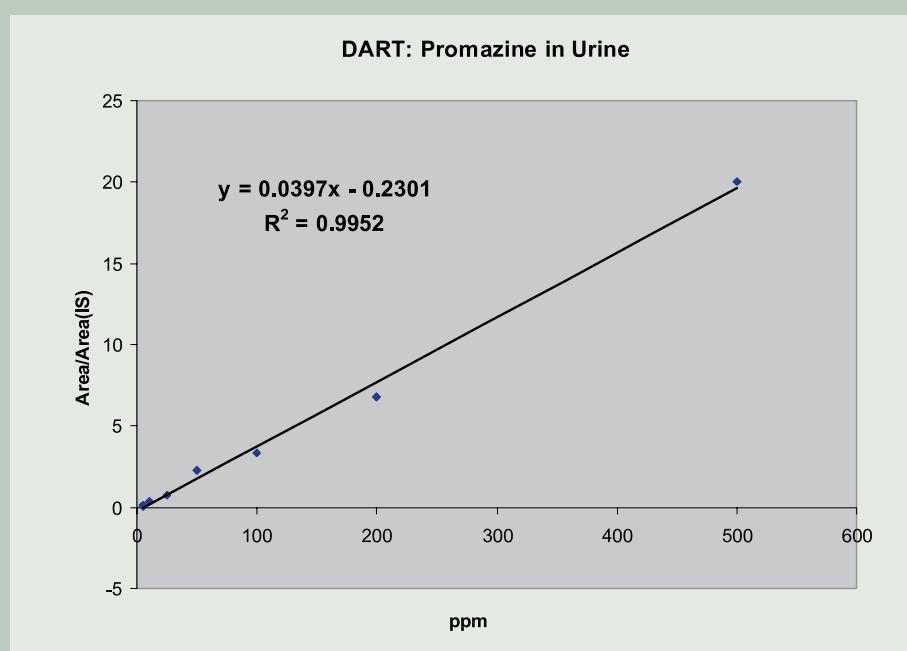


Fig. 5 Rapid quantitative analysis by DART of promazine in urine. Chlorpromazine was added as an internal standard.

monly encountered in urine that have elemental compositions that match the measured  $m/z$  values. It is interesting to note that the basic drug, ranitidine, is observed as an  $[M-H]^-$  species in the negative-ion mass spectrum as well as an abundant  $[M+H]^+$  species in the positive-ion mass spectrum. Ranitidine metabolites are also observed [11] in the positive-ion mass spectrum (not shown).

DART can be used for quantitative analysis. The absolute abundance of ions produced by DART depends on the positioning of the target in the gas stream. However, the use of an internal standard permits rapid quantitative analysis of drugs in urine, plasma, or other body fluids. Figure 5 shows a working curve obtained for urine samples spiked with promazine at the 1 to 500 ppm level. Chlorpromazine (50 ppm) was added as an internal standard. Undiluted urine samples were applied to a glass rod. Each analysis was complete within seconds of placing the rod in front of the DART source. This approach has also been used to screen for the "date rape" drug gamma hydroxy butyrate (GHB) in urine [24] and for the rapid quantitative analysis of developmental drugs in plasma.

The detection of explosives is important for forensics and security. DART has been applied to the detection of nitro explosives such as nitroglycerine, TNT, and HMX, inorganic explosives such as ammonium nitrate, perchlorate and azide, and peroxide explosives such as TATP and HMTD. Examples are shown in Figures 6 and 7.

The high dynamic range of the DART-AccuTOF combination can permit the identification of trace-level impurities for quality control and similar applications. An example is shown in Figure 8 and Table 2 for the exact-mass analysis of 1% propazine and 0.2% simazine in a sample of the herbicide atrazine.

## Conclusion

A new ion source has been developed that permits the analysis of gases, liquids, and solids in open air under ambient conditions. No solvents or high-pressure gases are used. The sample is not directly exposed to high voltages, laser beams or radiation or plasma. The combination of this source with a high-resolution time-of-flight mass spectrometer permits rapid qualitative and quantitative analysis of a wide variety of materials.

## Acknowledgment

Technical assistance and keen scientific insight were unselfishly provided by (in alphabetical order) Daniel Banquer, Ted Boileau, William Creasy, Daniel Evans, Drew McCrady, Michael McKie, Michael Nilles, Edward Owen, Gary Samuelson, Philip Smith, John Stuff, and Dean Tipple. The authors would like to thank Prof. Facundo Fernandez of Georgia Tech University for the dihydroartemisinin and counterfeit drug sample.

## Additional Information

Additional applications and digital videos showing DART analysis are available on the internet at <http://www.jeolusa.com/ms/msprod->

saccutof\_dart.html. Chemical agent data is available from the authors upon request.

## References

- [1] Dempster, A. J. *Phys. Rev.*, **11**, 316-324, (1918).
- [2] Munson, M. S. B.; Franklin, F. H. *J. Am. Chem. Soc.*, **88**, 2621, (1966).
- [3] Barber, M.; Bordoli, R. S.; Elliott, G. J.; Sedgwick, R. D.; Tyler, A. N. *J. Chem. Soc. Chem. Commun.*, **325**, (1981).
- [4] Beckey H. D. *Research/Development*, **20**(11), 26-29, (1969).
- [5] Horning, E. C.; Horning, M. E.; Carroll, D. I.; Dzidic, I.; Stilwell, R. N.; *Anal. Chem.*, **45**, 936-943, (1973).
- [6] Dole, M. Mack, L. L. Hines, R. L.; Mobley, R. C.; Ferguson, L. D. Alice, M. *J. Chem. Phys.*, **49**, 2240, (1968).
- [7] Aleksandrov, M. L.; Gall, L. N. Krasnov, N. V. Nikolaev, V. I. Pavlenko, V. A.; Shkurov, V. A. *Dokl. Akad. Nauk. SSSR*, **277**, 379-383, (1984).
- [8] Fenn, J. B.; Mann, M.; Meng, C. K.; Wong, S. F. *Science*, **246**, 64-71, (1989).
- [9] Tanaka, K.; Waki, H.; Ido, Y.; Akita, S.; Yoshida, Y. *Rapid. Commun. Mass Spectrom.*, **2**, 151-153, (1988).
- [10] Karas, M.; Hillenkamp, F. *Anal. Chem.*, **60**, 2299-2301, (1988).
- [11] Robb, D. B.; Covey, T. R.; Bruins, A. P. *Anal. Chem.*, **72**, 3653-3659, (2000).
- [12] Cody, R. B.; Laramee, J. A.; Durst, H. D. *Anal. Chem.*, **77**(8), 2297 - 2302, (2005).
- [13] Patents pending.
- [14] Penning, F. M. *Naturwissenschaften*, **15**, 818, (1927).
- [15] Mastwijk, H. C. Cold Collisions of Metastable Helium Atoms, Ph.D. Thesis, University of Utrecht, Netherlands, (1997).
- [16] Faubert, D.; Paul, G.J.C., Giroux, J.; Bertrand, M. J. *Int. J. Mass Spectrom. Ion Proc.*, **124**, 69, (1993).
- [17] Faubert, D.; L'Heureux, A.; Peraldi, O.; Mousselmal, M.; Sanchez, G.; Bertrand, M. J.; "Metastable Atom Bombardment (MAB) Ionization Source: Design, Optimization and Analytical Performances" in *Adv. Mass Spectrom.: 15th International Mass Spectrometry Conference*, Wiley: Chichester, UK, 431-432, (2001).
- [18] [http://www.jeol.com/ms/docs/map\\_note.pdf](http://www.jeol.com/ms/docs/map_note.pdf).
- [19] Tsuchiya, M. Kuwabara, H.; *Anal. Chem.*, **56**, 14, (1984).
- [20] Tsuchiya, M. *Mass Spectrom. Rev.*, **17**, 51, (1998).
- [21] Tsuchiya, M. *Analytical Sciences.*, **14**, 661-676, (1998).
- [22] Hiraoka, K.; Fujimaki, S.; Kambara, S.; Furuya, H.; Okazaki, S. *Rapid Commun. Mass Spectrom.*, **18**, 2323-2330, (2004).
- [23] McLuckey, S. A.; Glish, G. L.; Asano, K. G.; Grant, B. C., *Anal. Chem.*, **60**, 2220, (1988).
- [24] Guzowski, J. P., Jr.; Broekaert, J. A. C.; Ray, S. J.; Hieftje, G. M. J. *Anal. At. Spectrom.*, **14**, 1121-1127, (1999).
- [25] IonSense, Inc., 11 Dearborn Road, Peabody, MA USA 01960.
- [26] Jagerdeo, E.; Cody, R. B. unpublished results.

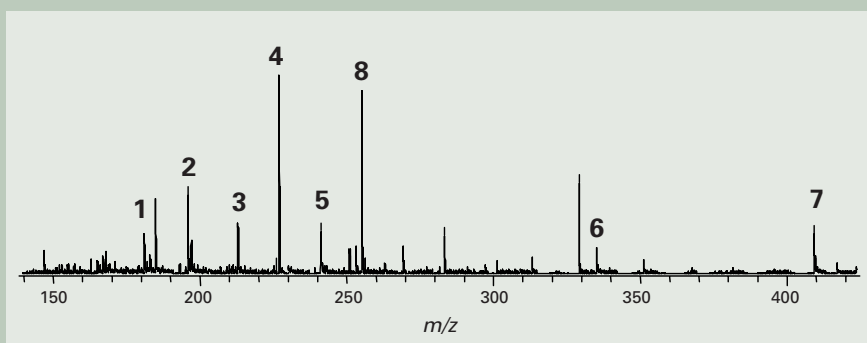


Fig. 6 3 ppm explosives spiked into muddy water. 1=DNT, 2=amino-DNT, 3=trinitrobenzene, 4=TNT, 5=RDY+TFA, 6=Tetryl, 7=HMX+TFA, 8=palmitate in the water background (used as lock mass). Headspace vapor from a 0.1% aqueous solution of trifluoroacetic acid was used to produce TFA adducts.

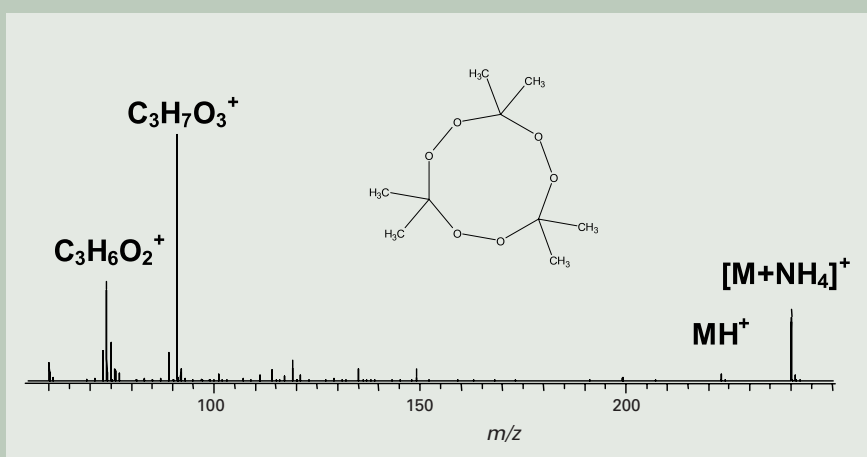


Fig. 7 Positive-ion DART mass spectrum of triacetone triperoxide (TATP). Ammonium hydroxide headspace vapor provided a source of  $\text{NH}_4^+$ .

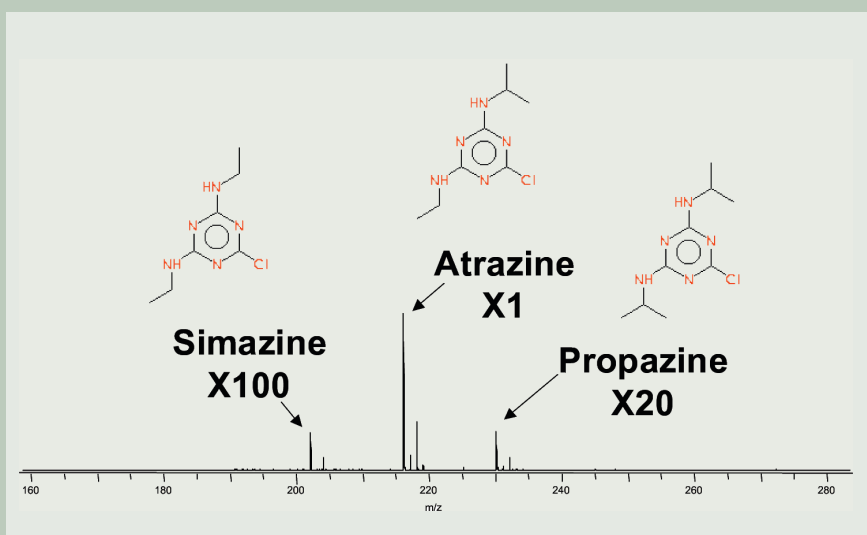


Fig. 8 Exact-mass analysis of trace simazine and propazine in a sample of the herbicide atrazine.

Table 2 DART measured masses for  $[\text{M}+\text{H}]^+$  from atrazine and trace impurities.

Compound	Composition	Measured	Calculated	Diff. (mmu)
Atrazine	$\text{C}_8\text{H}_{15}\text{N}_5\text{Cl}$	216.10159	216.10160	-0.01
Propazine	$\text{C}_9\text{H}_{17}\text{N}_5\text{C}$	230.11760	230.11725	+0.35
Simazine	$\text{C}_7\text{H}_{13}\text{N}_5\text{Cl}$	202.08440	202.08595	+1.60

# High Energy Backscattered Electron Imaging of Subsurface Cu Interconnects

Lynne M. Gignac<sup>†</sup>, Masahiro Kawasaki<sup>††</sup>, Steven H. Boettcher<sup>†††</sup> and Oliver C. Wells<sup>††††</sup>

<sup>†</sup>IBM T. J. Watson Research Center

<sup>††</sup>JEOL USA, Inc.

<sup>†††</sup>IBM Microelectronics Division

<sup>††††</sup>IBM T. J. Watson Research Center, Emeritus

In bulk Si integrated circuit devices, passivated copper interconnects that were located 0.65-2.7  $\mu\text{m}$  below the surface were imaged in two different transmission electron microscopes with scanning attachments by detecting backscattered electrons (BSEs) using incident beam energies that ranged from 150 keV to 400 keV. Since the BSE yield was strongly dependent on atomic number, voids in the subsurface Cu interconnects could be detected without having to alter the sample by cross-sectioning or delayering even when the voids were located under complex, dielectric surface topography or upper level Cu lines or vias. Because the electron beam broadens from low angle, elastic scattering events during the initial stages of penetration into the sample, the subsurface image resolution depended on the depth below the surface where the electrons were backscattered, the composition of the overlayer material(s) and the incident beam energy. Beam spreads were measured at several incident beam energies from BSE images of Cu interconnects buried under varying thicknesses of  $\text{SiO}_2\text{-SiN}_x$  dielectric. Tilt series tomography was attempted on passivated, 2-level Cu interconnects but increased beam spread and decreased signal with tilt allowed imaging up to only  $\pm 40^\circ$ .

## Introduction

The scanning electron microscope (SEM) is a critical tool for in-line defect characterization, critical dimension measurements and failure analysis of semiconductor devices. As devices continue to shrink, the trend in imaging fine semiconductor structures in the SEM has been to use field emission electron sources at low beam energies,  $< 5$  keV, and to detect secondary electrons (SE). This small spot, low beam current configuration can produce high resolution images of the sample surface with minimal sample charging. However, when higher energy incident electron beams are employed and backscattered electrons (BSEs) are detected, images can be obtained with high topographic or atomic number (Z) contrast and detail below the sample surface can be detected [1-5]. A specific application for BSE subsurface imaging is for the characterization of multi-level Cu interconnects passivated with  $\text{SiO}_2$  or low dielectric constant amorphous dielectrics [6-22]. Here the low Z surface dielectric does not greatly scatter the electron beam allowing the higher Z, Cu-Ta containing subsurface lines to be imaged with BSEs. Defects such as voids in Cu interconnects or metal extruded out of the interconnect can be imaged with one, topdown BSE image, even if the defect is buried under complex, dielectric surface topography or upper level metal. BSE imaging has potential as a technique that is able to characterize subsurface device struc-

tures without having to physically alter the sample by cross-sectioning or delayering though electron beam induced damage of devices has been reported [11-12].

Initial work on BSE subsurface imaging of interconnect structures was published in the 1990's where both SEMs [6-8, 10-15] and transmission electron microscopes (TEMs) with scanning attachments [6, 9, 17] were used to image Al interconnects passivated with  $\text{SiO}_2$  or  $\text{SiN}_x$ . Since the image resolution was dependent on the beam spread caused by scattering by sample atoms, higher energy incident electron beams were used to reduce beam broadening and to improve the resolution of the BSE images.

Energy filtered BSE imaging has been studied as a microtomography technique where a series of images representing specific BSE energies were collected for a given incident electron beam energy [13-15]. Since BSEs which have lost a certain amount of energy are typically generated from a given depth in the sample, an energy-filtered image series represents two-dimensional slices of the sample at various points below the sample surface. Since interconnects are non-uniform in composition laterally, an energy-filtered image can suffer from contrast inversion where a low atomic number layer that is located deep below the surface can have higher intensity than a high atomic number layer located closer to the surface. Therefore, a given BSE energy image will represent a variety of depths below the surface making the microtomography reconstruction difficult.

In recent years, there has been renewed interest in using BSE to image subsurface

interconnect structures [18-21]. In this paper, subsurface imaging of multi-level Cu interconnects with BSEs is demonstrated by using transmission electron microscopes with scanning attachments with beam energies of 150 keV to 400 keV. The BSE images were used to detect voids in subsurface Cu interconnects and to characterize beam spread at various depths below the surface.

## Experimental Procedure

High voltage BSE imaging of bulk, passivated Cu- $\text{SiO}_2\text{-SiN}_x$  interconnects was performed at 150 keV and 400 keV using a JEOL JEM-4000FX TEM with a  $\text{LaB}_6$  thermionic source and at 300 keV in a JEOL JEM-3000F TEM with a Schottky field emission source. Both TEMs were equipped with scanning attachments and BSE detectors. The JEM-4000FX had a rectangular shaped, 2-piece Si solid state BSE detector located under the objective polepiece, 4 mm above the sample surface with a hole in the center to allow passage of the electron beam. The detector solid angle was  $\sim 1.3$  sr and it detected electrons backscattered at angles of  $27\text{-}54^\circ$  from the incident beam direction. The JEM-3000F had a microchannel plate (MCP), annular shaped, center hole detector located above the objective polepiece, 46 mm above the sample surface. The detector solid angle was  $\sim 0.14$  sr and detected BSE at angles of  $3\text{-}12^\circ$  from the incident beam direction. The MCP detector could be biased allowing the detection of either BSEs or SEs. In addition to the solid state BSE detector, the JEM-4000FX had an Everhart-Thornley SE detector.

Bulk samples could be inserted in both microscopes using standard sample holders if they were cored into 3 mm discs and backside polished to reduce the sample thickness. In the JEM-4000FX, a bulk specimen holder was also available and could be used to study chips that had dimensions less than  $4 \times 8$  mm. In both microscopes, electronic BSE images could be acquired using digital image capture systems.

Free lens control was used to create higher current probes than the standard probes used for scanning transmission electron microscope (STEM) bright field or dark field imaging of thin samples. The high current conditions were produced by weakening the first condenser lens strength so that a larger sized probe was formed with increased total current. A Faraday cup was not available to measure the probe current in the JEM-4000FX but a value of  $\sim 13$  nA was estimated for the free lens generated BSE probe. For the JEM-3000F, a Faraday cup measured the high current BSE probe to be 10 nA; a current  $\sim 20\times$  greater than the standard 1 nm STEM probe.

Various multilevel, passivated Cu interconnects were studied in this work. All samples were produced using Cu single or dual Damascene processing [22] where a blanket dielectric layer was initially deposited on the wafer. Lines and vias were patterned in the dielectric using photolithography and reactive ion etching and then metal was deposited to fill the open lines and vias. Chemical-mechanical polishing (CMP) was used to remove the excess metal and to planarize the layer. The deposited metal layers consisted of a thin, sputtered deposited TaN/Ta liner [23] followed by a sputtered Cu seed layer and then electroplated Cu. The dielectric material consisted primarily of  $\text{SiO}_2$  but all Cu levels were capped with a thin  $\text{SiN}_x$  film. All samples were passivated with dielectric so that the Cu interconnects were located below the sample surface. The samples contained between 1-3 Cu levels.

## Results and Discussion

When the high voltage BSE imaging technique was initially being developed in the JEM-4000FX, a standard "L" STEM probe was selected that was typically used for bright field imaging of thin samples. In **Fig. 1a**, a TEM micrograph of a two-level Cu interconnect is shown in cross-section where the top M2 Cu line is located under  $0.65 \mu\text{m}$  of  $\text{SiO}_2\text{-SiN}_x$  dielectric, the lower M1 Cu line is located  $1.60 \mu\text{m}$  below the surface and an Al bond pad is seen on the dielectric surface. In **Fig. 1b**, a low magnification BSE image of this 2-level Cu interconnect structure is seen at 400 keV with a standard JEM-4000FX "L" STEM probe. Though an image was obtained showing the Al bond pad and the subsurface M2 and M1 Cu levels, the image was very noisy and not very informative. When free lens control was used to generate a higher incident beam current, a sharper BSE image was obtained with significantly lower noise, see **Fig. 1c**. The sample studied in **Fig. 1** was produced using a non-standard processing condition that caused a high density of stress voids to be produced in the Cu conductors. These voids are seen as regions of dark contrast in both the M2 and M1 Cu lines in **Fig. 1c**.

In **Fig. 1c**, the sensitivity of BSE imaging to atomic number (Z) contrast is shown not only in large signal intensity differences between the voided and non-voided regions in the Cu lines but also by the intensity differences in areas with TaN/Ta liner, Cu, and  $\text{SiO}_2/\text{SiN}_x$  dielectric. Since previous studies have shown that the BSE signal intensity can be directly related to the thickness of a single level thin film, [4-5, 24-25] the signal intensity in the Cu line regions of the BSE image can be related to the amount of Cu in that region. The M2 and M1 Cu conductors were both  $0.35 \mu\text{m}$  thick and the individual M2 and M1 regions had similar signal intensity levels in **Fig. 1c**. The M2/M1 overlap regions had much greater signal intensity than the individual layers. Though multilevel Cu interconnect samples are more complex than single layer films, BSE imaging, with the aid of Monte Carlo simulations and sophisticated image analysis routines, could be developed as a quantitative ana-

lytical technique where void volume or film thickness could be measured from a single BSE image without having to cross-section the sample.

**Fig. 2** shows TEM and BSE images of a 3-level Cu electromigration (EM) test structure. **Fig. 2a** is a TEM cross-section image of the anode end of an untested structure showing an upper M3 Cu level under  $0.65 \mu\text{m}$  of  $\text{SiO}_2\text{-SiN}_x$ , a middle level M2 Cu electromigration test structure  $1.75 \mu\text{m}$  below the surface, and a M1 Cu fill structure  $2.70 \mu\text{m}$  below the surface. A V2 Cu via connects the M3 line to the M2 test structure. In **Figs. 2b** and **2c**, BSE images of the anode end of a stressed electromigration test structure are shown at 150 keV and 400 keV. All three Cu levels are seen in both images, even the lowest level M1 fill structure. There is a large void in the top level M3 line near the V2 contact and this void was imaged with greater contrast at 150 keV than at 400 keV. In both BSE images, the edges of

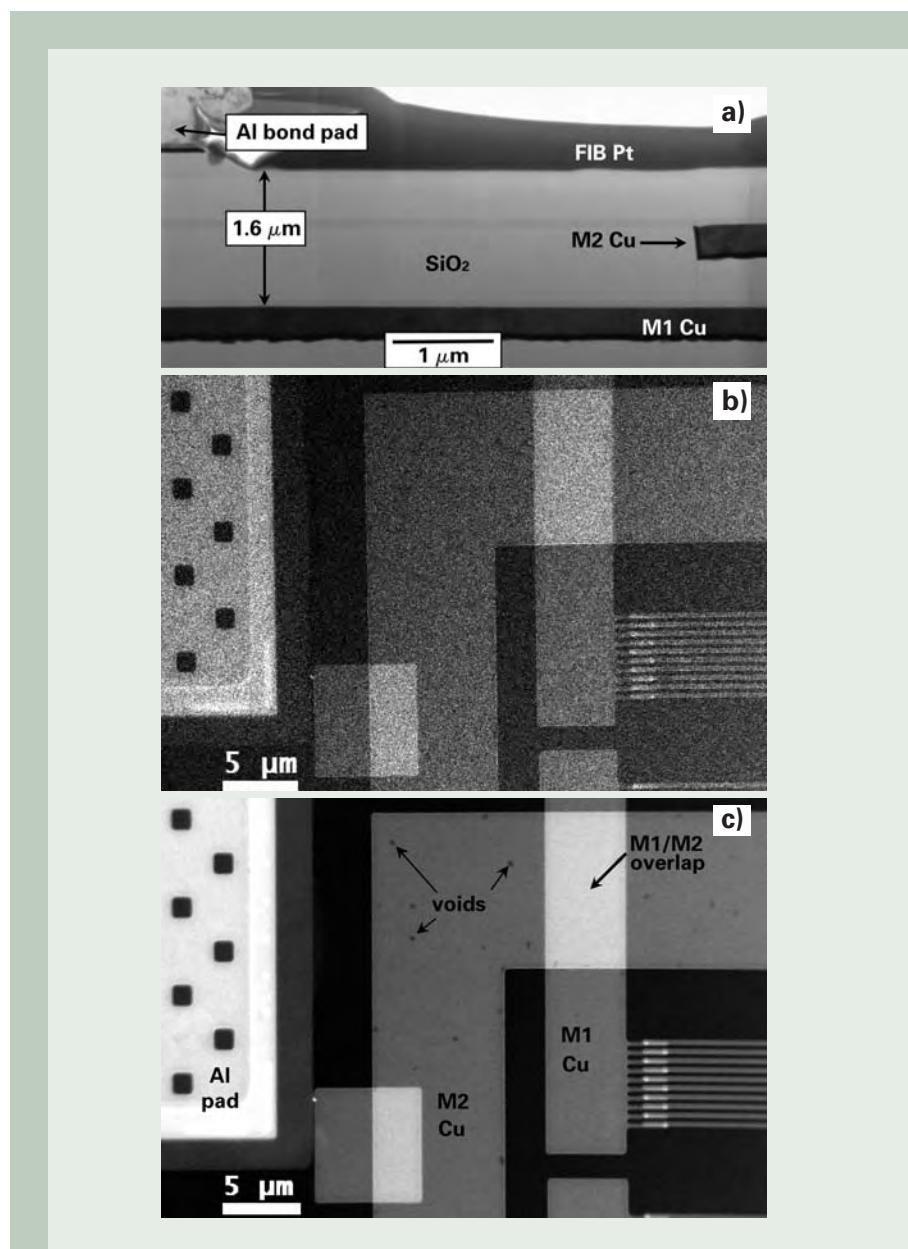


**Fig. 1** Passivated, 2-level Cu interconnect structure with stress voids: a) TEM cross-section micrograph, and 400 keV BSE images taken with b) a standard "L" STEM probe and c) a free lens generated high current BSE probe.

the M3 lines have a band of brighter intensity due to Z contrast from the fine TaN/Ta liner that encased the Cu lines. The edges of all the lines are sharper at 400 keV than at 150 keV showing that the subsurface 400 keV BSE image had better resolution. During the initial stages of penetration into the sample, the beam spreads due to small angle Rutherford scattering while intensity is lost from that compact part of the beam from wide angle Rutherford scattering events. At a given depth, a 400 keV electron beam will be narrower than a 150 keV beam and will produce a better resolution, subsurface BSE image. However, the 400 keV electron beam will penetrate deeper into the sample than the 150 keV beam and will generate fewer BSEs in the upper layers. Thus, the Z contrast generated by the void in the M3 layer was less at 400 keV than 150 keV [4].

The ability to detect Z contrast from the TaN/Ta liner was dependent on the liner thickness and the beam spread. The beam diameter

varied depending on the incident electron energy, the overlayer material and the depth below the surface where the structure was located. The beam diameter at various depths below the surface after passing through SiO<sub>2</sub>-SiN<sub>x</sub> dielectric was measured from BSE images taken at 30 keV, 150 keV and 400 keV by taking an intensity line scan across the edge of wide Cu lines where the intensity changed from a low signal in the SiO<sub>2</sub>-SiN<sub>x</sub> dielectric to a high signal in the Cu line. The 30 keV data was obtained from BSE images taken on a cold field emission SEM. The derivative of the line scan was plotted and the beam diameter was estimated from the full-width half maximum (FWHM) of the derivative peak. When there was TaN/Ta-Cu Z contrast, the beam diameter was calculated as twice the half-width at full maximum where the half-width was taken from the side of the derivative peak going from dielectric to TaN/Ta.

In Fig. 3, the measured values of the beam

diameters (solid symbols) are plotted versus the dielectric overlayer thickness. A least squares fit to the measured data is shown as dashed lines. For comparison, a theoretical estimate of the beam spread is given as solid lines. The theoretical values were obtained by using Goldstein et al.'s [26] beam broadening relation for a single Rutherford scattering event through SiO<sub>2</sub>. The theoretical and experimentally determined subsurface beam diameters agreed for overlayer thicknesses less than 0.65 μm. As the SiO<sub>2</sub> overlayer thickness increased, the measured diameters were less than the theoretical values and, for 150 keV, the beam spread began to level off at SiO<sub>2</sub> overlayer thicknesses greater than 2 μm. Even though the Goldstein et al. relation was derived from a single electron scattering event and these BSE images resulted from multiple scattering events, the experimentally derived diameters were less than the measured diameters. The leveling off of the beam spread with

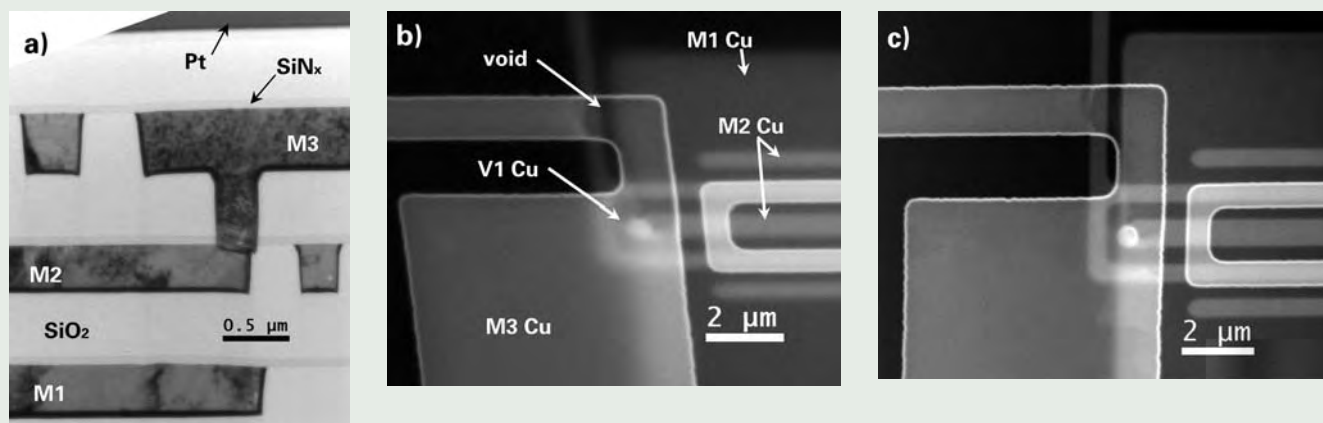


Fig. 2 Anode end of a passivated, 3-level electromigration test structure: a) TEM cross-section micrograph of an unstressed structure and BSE images of a stressed structure taken at b) 150 and c) 400 keV, respectively.

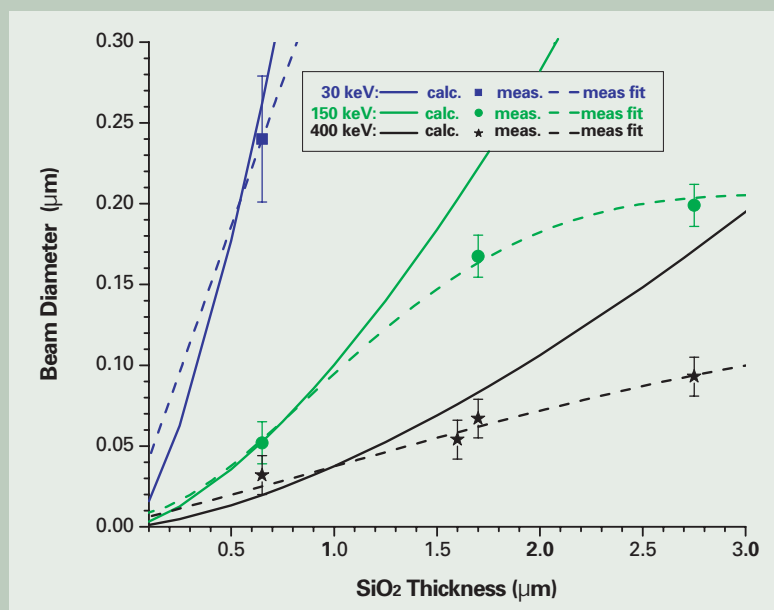


Fig. 3 A plot of beam spread versus SiO<sub>2</sub> overlayer thickness: symbols are measured values, dotted lines are least squares fits to the measured data and solid lines are theoretical predictions of the beam spread.

thick overlayers was predicted from Monte Carlo simulations by Rau and Reimer [18]. Their simulations showed that an incident electron could not deviate greatly from the incident beam position to be able to make it to a great depth below the surface and at that depth, the electron had equal probability of making it out of the sample or being absorbed. Thus, at large depths, the actual beam spread was less than theoretical predictions. It may be difficult to take advantage of the reduced beam spread at great depths below the surface because the detectable BSE signal also decreases with depth.

In the BSE images in **Figs. 2b-c**, TaN/Ta-Cu Z contrast is seen for the top M3 Cu level at both 150 keV and 400 keV. The M3 level was located 0.65  $\mu\text{m}$  below the sample surface and the liner sidewall thickness varied from 0.05 to 0.08  $\mu\text{m}$ . From **Fig. 3**, it is expected that the high energy incident electron beams would produce TaN/Ta-Cu Z contrast since the beam diameter was 0.05  $\mu\text{m}$  and 0.03  $\mu\text{m}$  at 150 keV and 400 keV. Here the beam size was less than or equal to the liner thickness. At 30 keV, the beam spread to 0.24  $\mu\text{m}$  at M3 level and, in the SEM BSE image, no liner-Cu Z contrast was observed. In **Figs. 2b-c**, liner-Cu Z contrast was not seen at the M2 level for 150 keV and 400 keV but was just barely distinguished at the M1 level for 400 keV only. Previous studies have shown that TaN/Ta to Cu Z contrast is seen when the beam diameter is  $\leq 1.5$  times the liner thickness [20].

BSE imaging can be used to image voids in

Cu lines below complex, dielectric surface topography. Damascene interconnect processing involves creating open trenches and vias in dielectric and then filling the open regions with TaN/Ta and Cu metals. The vias connect one metal level to another and there can be 9 or more Cu levels in advanced chips. When there is a problem with voiding in an existing Cu line when processing the next metal level, a complex surface structure of open trenches and vias can obscure the imaging of the lower level Cu. An example of this surface structure is shown in **Fig. 4a** where a 150 keV SE image of open dual Damascene M2 trenches and V1 vias is shown. In this sample, there is a Cu M1 level under the open V1 vias and the sample was subjected to a Cu etch solution to partially remove M1 Cu. Below the M1 Cu lines, there are tungsten CA vias that connect the M1 level to Si. In the SE image, the open M2 trenches and V1 vias are clearly seen along with some subsurface M1 Cu lines and CA W vias.

In **Fig. 4b**, a 150 keV BSE image of the same region shown in **Fig. 4a** is given and an ion-induced secondary electron cross-section image taken at 45° with a focused ion beam microscope is shown in **Fig. 4c**. The region of the chip that was sectioned is shown as dotted lines in **Figs. 4a-b**. The BSE image differed from the SE image in that the surface dielectric and open structures were not seen but the subsurface M1 lines and W CA vias were clearly distinguished. The SiO<sub>2</sub>-SiN<sub>x</sub> dielectric was composed of low Z elements which did not produce many BSE. Thus, there was not much

BSE signal intensity difference between full thickness dielectric regions and the open M2 trench regions.

In the BSE image in **Fig. 4b**, the voids that were intentionally produced by etching the M1 Cu were detected as dark regions in the M1 Cu lines and the W CA vias were visible as bright round circles. These features can also be seen in the cross-section in **Fig. 4c**. It would be difficult to find voids in M1 lines under open M2/V1 structures by any other top-down imaging or inspection technique. A SE image would be confounded by the open surface structures and optical inspection methods would suffer from light scattering off these structures in addition to being limited by resolution when imaging sub-0.1  $\mu\text{m}$  wide lines.

Since a high energy BSE image is a planar composite of multiple metal levels, BSE imaging could be used to verify the alignment on or inspect defects in various subsurface metal layers. However, it would be difficult to analyze very large regions on a chip since high energy BSE imaging must be done in a TEM that typically can only hold samples that are 3 mm diameter. It is not difficult to imagine the usefulness of a high energy SEM with a large sample stage that could be used for wafer inspection and failure analysis especially since defects such as voids in Cu lines can be detected without having to physically damage a wafer. However, development of this type of tool may be hindered by the fear of electron beam induced semiconductor device defects.

A final example of subsurface, high energy

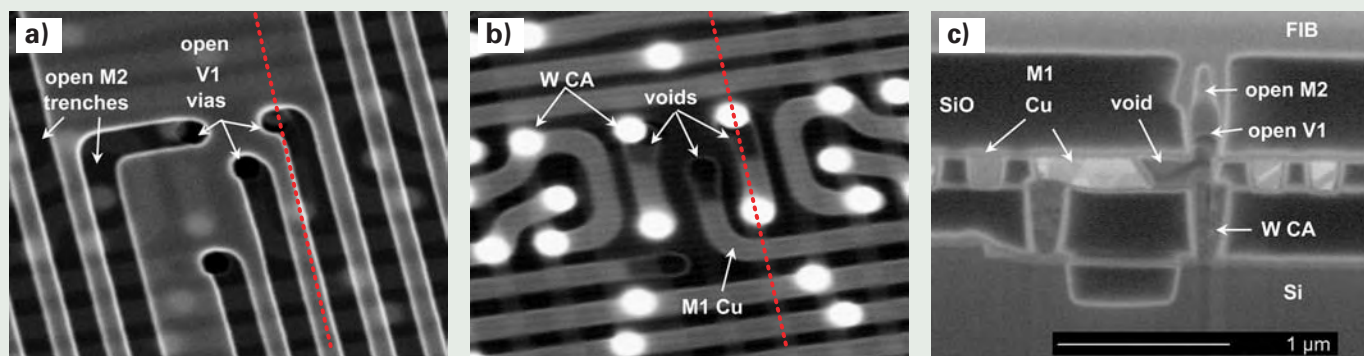


Fig. 4 A chip with open dual Damascene M2 trenches and V1 vias over M1 Cu lines and W CA vias: a) 150 keV SE image, b) 150 keV BSE image, and c) 45° focused ion beam cross-section image of the dotted line region seen Fig. 4a-b.

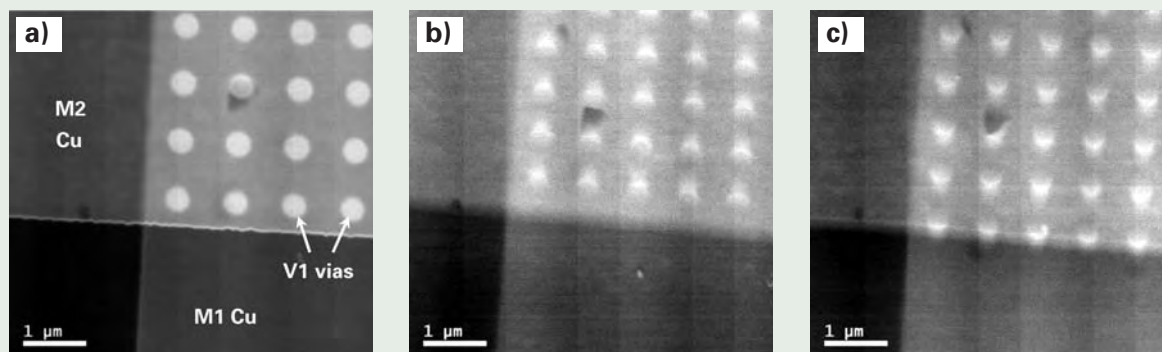


Fig. 5 300 keV BSE images of a passivated, 2-level Cu interconnect structure with stress voids where a 5  $\mu\text{m}$  wide M2 Cu line is connected to a 5  $\mu\text{m}$  wide M1 line through a sea of V1 vias: a) 0° tilt, b) +40° tilt, and c) -40° tilt.

BSE imaging is an attempt to do BSE tilt series tomography on the stress voided, 2-level Cu chip shown in **Fig. 1**. The region of the chip that was imaged for tilt tomography contained a 5  $\mu\text{m}$  wide M2 Cu line connected to a 5  $\mu\text{m}$  wide M1 Cu line through a sea of V1 vias. This stress voided chip was a good initial candidate for tomography to be able to visualize the depth and location of the voids near vias. A BSE image of this region of the chip that was taken in the JEM-3000F field emission TEM at 300 keV is shown at 0° tilt in **Fig. 5a**. The intention of this experiment was to take a series of images at a range of tilts from  $\pm 70^\circ$  and then use tomography software to construct three-dimensional representations. However, as the tilt increased, the beam traveled through increased sample thicknesses which caused the beam to broaden. In addition, the signal significantly decreased with tilt and images could only be recorded at maximum tilt values near  $\pm 40^\circ$ , see **Figs. 5b-c**. At high tilts, BSE were forward scattered away from the fixed detector which was situated below the polepiece, 90° from the flat sample surface. BSE tilt series tomography initially seemed to be a good idea since minimal sample preparation was required and a large imaging volume could be sampled but the problems of beam spread and signal loss defeated this initial attempt. Improved BSE tilt tomography could probably be accomplished with a moveable or variable position BSE detector but typically there is limited space in a TEM polepiece.

## Conclusions

BSE imaging of passivated Cu interconnect structures was used to image voids in Cu lines even when the lines were buried 1.6  $\mu\text{m}$  below the surface or under complex, dielectric surface topography. The subsurface image resolution and TaN/Ta-Cu Z contrast were limited by the spreading of the beam that occurred from small-angle elastic scattering of the incident electron beam with atoms in the sample. The beam broadening was measured for various SiO<sub>2</sub> surface layer thicknesses and incident beam energies. Tilt series BSE tomography was attempted but was not successful because the beam spread increased and the signal significantly decreased as the sample was tilted away from the fixed detector which was located below the objective polepiece. Commercial development of a SEM with both high incident beam energy and large sample stage capabilities could be beneficial to decreasing cost and increasing yield in a semiconductor fab since defect inspection and failure analysis could be performed on a full wafer without having to scrap the wafer. However there are several deterrents that could hinder tool development which include beam spread and image resolution on the order of the sub-0.1  $\mu\text{m}$  Cu line dimension, low dielectric constant dielectrics that shrink when imaged with an electron beam, increased fill structures at each Cu level that improves CMP uniformity but obstructs BSE subsurface imaging and electron beam induced semiconductor device defects.

## Acknowledgements

The authors would like to thank Tom Shaw for initiating research in high energy BSE

imaging at IBM T.J. Watson Research Center, John Bruley for helpful technical discussions, and Eric Liniger for providing EM test structures for this study.

## References

- [1] D. McMullan, "An improved scanning electron microscope for opaque specimens," *Proc. IEE-London* **100**, 245-259 (1952).
- [2] S. Kimoto and H. Hashimoto, "Stereoscopic observation in scanning microscopy using multiple detectors," *The Electron Microprobe, Proc. Symp., Washington D. C., Eds. T. D. McKinley et al., 480-489 (John Wiley & Sons, New York, NY, 1964).*
- [3] O. C. Wells, "Effects of collector take-off angle and energy filtering on the BSE image in the SEM," *Scanning*, **2**, 199-216 (1979).
- [4] H. Neidrig, "Electron backscattering from thin films," *J. Appl. Phys.*, **53**, R15-R49 (1982).
- [5] O. C. Wells, R. J. Savoy and P. J. Bailey, "Backscattered electron (BSE) imaging in the scanning electron microscope (SEM)-measurement of surface layer mass-thickness," *Electron Beam Interactions with Solids, SEM, Inc, AMF O'Hare (Chicago) 287-298 (1982).*
- [6] D. M. Follstaedt, J. A. Van Den Avyle, A. D. Romig, and J. A. Knapp, "High-energy backscattered electron imaging of voids in aluminum metallizations," *Mat. Res. Soc. Proc.*, **225**, 223-230 (1991).
- [7] E. Castano, J. Maiz, P. Flinn and M. Madden, "In situ observations of dc and ac electromigration in passivated Al lines," *Appl. Phys. Lett.*, **59**, 129-131 (1991).
- [8] P. R. Besser, M. C. Madden and P. A. Flinn, "In situ scanning electron microscopy observation of the dynamic behavior of electromigration voids in passivated aluminum lines," *J. Appl. Phys.*, **72**, 3792-3797 (1992).
- [9] M. C. Madden, E. V. Abratowski, T. N. Marieb, and P. A. Flynn, "High resolution observation of void motion in passivated metal lines under electromigration stress," *Mater. Res. Soc. Proc.*, **265**, 33-38 (1992).
- [10] H. Todokoro, D. Eng and F. Mizuno, "Observation and measurement of microstructures using a high-energy scanning electron microscope," *Hitachi Review*, **44**, 107-112 (1995).
- [11] S. Yamada, T. Ono and F. Mizuno, "Study on irradiation damage to semiconductor devices by 200 keV electrons caused by BEASTLI method," *Proc. SPIE*, **2439**, 374-382 (1995).
- [12] F. Mizuno, S. Yamada, and T. Ono, "Effects of 50 to 200-keV electrons by BEASTLI method on semiconductor devices," *IEICE Trans. E79-C*, 392-397 (1996).
- [13] V. V. Aristov, E. I. Rau and E. B. Yakimov, "'Apparatus' electron beam microtomography in SEM," *Phys. Stat. Sol. (a)*, **150**, 211-219 (1995).
- [14] E. I. Rau and V. N. E. Robinson, "An annular toroidal backscattered electron analyzer for use in scanning electron microscopy," *Scanning*, **18**, 556-561 (1996).
- [15] H. Neidrig and E. I. Rau, Information depth and spatial resolution in BSE microtomography in SEM," *Nuc. Instr. Meth. Phys. Res. B*, **142**, 523-534 (1998).
- [16] J. R. Lowney, M. T. Postek, S. Jones, S. Mayo and M. Creswell, "Simulation and measurement of subsurface features in scanning electron microscope metrology," *Scanning*, **30**, 219-220 (1998).
- [17] J. C. Doan, S. Lee, S.-H. Lee, N. E. Meier, J. C. Bravman and P. A. Flinn, "A high-voltage scanning electron microscopy system for *in situ* electromigration testing," *Rev. Sci. Instr.*, **71**, 2848-2854 (2000).
- [18] E. I. Rau and L. Reimer, "Fundamental problems of imaging subsurface structures in the backscattered electron mode in scanning electron microscopy," *Scanning*, **23**, 235-240 (2001).
- [19] L. M. Gignac, M. Kawasaki, and S. H. Boettcher, "Imaging of subsurface Cu interconnects using high energy backscattered electrons," *Electronic Proc. 8<sup>th</sup> Asia-Pacific Conf., Electron Microscopy, 727-728 (2004).*
- [20] L. M. Gignac, M. Kawasaki, S. H. Boettcher and O. C. Wells, "Imaging and analysis of subsurface Cu interconnects by detecting backscattered electrons in the scanning electron microscope," *J. Appl. Phys.*, in press, tentative volume **97** (2005).
- [21] M. Matsui, S. Machida, H. Todokoro, T. Otaka, and A. Sugimoto, "Observation of subsurface structures using high-energy SEM," *Metrology, Inspection and Process Control for Microlithography XIX, R. M. Silver, Ed., Proc. SPIE vol., 5752 in press, tentative page 798-805 (2005).*
- [22] D. Edelstein, J. Heidenreich, R. Goldblatt, W. Cote, C. Uzoh, N. Lustig, P. Roper, T. McDevitt, W. Motsiff, A. Simon, J. Dukovic, R. Wachnik, H. Rathore, R. Schulz, L. Su, S. Luce, and J. Slattery, "Full copper wiring in a sub-0.25  $\mu\text{m}$  CMOS ULSI technology," *IEDM Tech Digest*, 773-776 (1997).
- [23] D. Edelstein, C. Uzoh, C. Cabral, P. DeHaven, P. Buchwalter, A. Simon, E. Cooney, S. Malhotra, D. Klaus, H. Rathore, B. Agarwala and D. Nguyen, "A high performance liner for copper damascene interconnects," *Proc. IEEE Int., Interconnect Tech., Conf.*, 9-11 (2001).
- [24] H. Neidrig, "Backscattered electrons as a tool for film thickness determination," *scanning electron microscopy 1978/I, SEM Inc., Chicago, 841-858 (1978).*
- [25] O. S. Rajora and A. E. Curzon, "The use of electron image contrast to measure the thickness and composition of thin films of light binary alloys," *Thin Solid Films*, **123**, 235-238 (1985).
- [26] J. I. Goldstein, J. L. Costley, G. W. Lorimer and S. J. B. Reed, "Quantitative x-ray analysis in the electron microscope," *Proc. 10<sup>th</sup> An. SEM Symp. (O. Johari ed.) SEM Inc., Chicago, IL 1, 315-324 (1977).*

# Recent Development of TEM for Advanced Ceramics

Yuichi Ikuhara

Institute of Engineering Innovation,  
The University of Tokyo

This paper reviews several recent improvements in new transmission electron microscopy (TEM) to characterize advanced ceramics. As theoretical calculations are getting popular, quantitative analyses for high resolution electron microscopy (HREM) and electron energy loss spectroscopy (EELS) are performed to determine the grain boundary atomic structures and chemical bonding state in ceramics. TEM in-situ straining technique has been also developed to directly characterize the atomic structures of crack walls in structural ceramics by using the crack induced tension (CIT) method which uses the micro-indenter driven by a piezo actuator. Ultra high resolution electron microscopy (UHREM) is a powerful technique to discriminate the species of atoms which are located closer to each other within 0.1 nm, and therefore light elements such as nitrogen and oxygen can be directly observed in the structure image. Low electron dose HREM can be applied to characterize soft ceramics such as zeolite and biomaterials by using a slow-scan CCD camera system. Scanning transmission electron microscopy (STEM) has been recently developed to directly obtain the atomic image by high angle annular dark field (HAADF) technique and also STEM-EELS-EDS (energy dispersive X-ray spectroscopy) combined technique to map the chemical composition and bonding state with a high spatial resolution. Ceramic sciences will be further developed by the newly developed TEM methods demonstrated here.

## Introduction

Transmission electron microscopy (TEM) is a powerful technique to characterize the microstructures, and has been intensively applied for advanced ceramics [1]. High resolution electron microscopy (HREM), energy dispersive X-ray spectroscopy (EDS) and electron energy loss spectroscopy (EELS) are the main techniques to characterize atomic structures, chemical composition and chemical bonding state in microstructures. These techniques have successfully provided many important information to understand the properties in advanced ceramics, i.e., grain boundary and interface phenomena are one of the key factors to understand the nature of the properties, and hence TEM has been widely used to elucidate the nature [2]. TEM has thus long since become an integral part of ceramic research. However, the capability of TEM analysis is not always perfect. We frequently need the microstructural information, which cannot be obtained by a conventional TEM, to further understand the properties and microstructures in advanced ceramics. In this article, some of recent improvements in TEM analyses are demonstrated.

One of the most striking development for TEM characterization is that theoretical calculations get popular and can be applied to quantitatively analyze the atomic and electronic structures. Combining with the theoretical calculations, complex and distorted atomic structure are possible to be determined by HREM

[3,4], and the origin of chemical shifts that appeared in EELS can be quantitatively interpreted [5,6]. Quantitative analyses for grain boundary structures and energy loss near edge structures (ELNES) are shown as the examples. In-situ observation in a TEM has contributed to the development of materials science and also played an important role for the basic knowledge of material phenomena. However, most of results obtained by the in-situ observation are of metals. This is because the specimen treatment was difficult for brittle ceramics. Although ceramics are expected as the structural materials, the atomic structure of the cleavage plane has even not been clarified. In-situ HREM observation can reveal the atomic structure on the cleavage plane, and an example of  $\text{Si}_3\text{N}_4$  observation will be demonstrated in this paper [7,8]. The resolution of conventional HREM is 0.17-0.20 nm at 200-300 kV, however, the resolution of about 0.1 nm can be achieved by using atomic resolution high voltage electron microscopy (ARHVEM) [9]. It will be shown here that ARHVEM can be applied to discriminate Ga and N in the GaN thin film. Electron irradiation damage is sometimes very serious in characterizing soft materials by TEM. In this case, low electron dose HREM is possible to reduce the density of electron dose by using a slow-scan CCD camera system. An example of direct observation of the channel structures in zeolite was demonstrated [10]. Scanning Transmission Electron Microscopy (STEM) has been recently paid much attention for direct atomic imaging and also STEM-EELS-EDS combined technique has emerged to characterize the chemical composition and bonding state at very narrow region such as grain boundaries and interfaces [11]. Several examples will be

shown in this paper.

## Quantitative Analysis

### HREM for ceramic grain boundary

HREM has been intensively applied to investigate the atomic structures in ceramics, and it has successfully provided important information on microstructural factors such as grain boundary, interface, lattice defect and so on. The macroscopic properties of ceramic materials are strongly influenced by the presence of grain boundaries. Therefore, quantitative characterization of the grain boundaries is needed to obtain materials with better or novel properties. In order to quantitatively evaluate the grain boundary atomic structures, well-defined specimens and theoretical calculations are needed in addition to HREM observations [3]. We have characterized many kinds of ceramic grain boundaries so far [12-15], and a result for zirconia grain boundary will be introduced as an example of quantitative analysis [15]. In this study,  $\Sigma=9$  [110] symmetric tilt grain boundary was fabricated by the hot-joining technique as a model specimen.

In order to predict the grain boundary atomistic structures theoretically, the systematic lattice statics calculations were performed using the GULP program code [16]. It has been well demonstrated that the lattice statics calculations were effective method for predicting the stable grain boundary structures in many kinds of ceramic materials [17,18]. In the calculation, the atomistic interactions are described by a potential function which divides the interatomic forces into long-range interactions (described by Coulomb's Law and summated by the Ewald method) and short-range interactions treated by a pairwise function of the

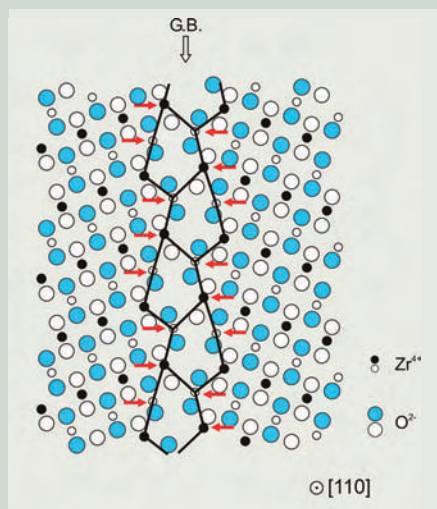


Fig. 1 The lowest energy structure of the  $\Sigma = 9$ ,  $\{221\}$  grain boundary obtained by the lattice statics calculations. Note that high density of cation sites with seven-fold coordination are formed along the boundary, as indicated by the small solid arrows.

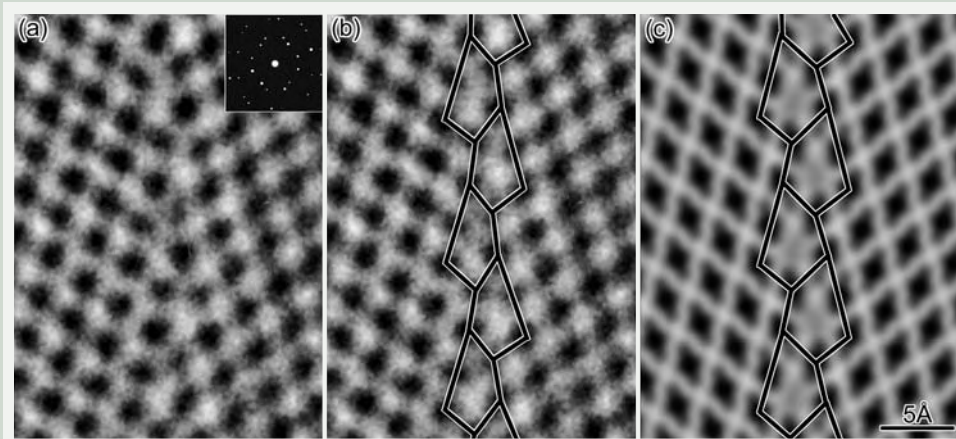


Fig. 2 The experimental ARHVEM image of the  $\Sigma = 9$ ,  $\{221\}$  grain boundary. In this condition, the black dots in the image correspond to the position of the cation column in the crystal. (b) Asymmetric structure units were drawn by the solid lines on the experimental image in (a). (c) The simulated ARHVEM image using the structure model shown in Fig. 1. The image simulation was performed on the condition that the defocus value is  $-38$  nm and a film thickness is  $4$  nm.

Buckingham. The potential parameters used in this study were taken from the literature reported by Lewis and Catlow [19]. The lattice energies were calculated summing all the potentials of constituent ions in the calculation cells. The grain boundary excess energies were estimated by subtracting the calculated lattice energy for the single crystal cell with the same number of ions from the calculated lattice energy for the cell including the grain boundary. The calculated energies were then evaluated as a function of the translation states, and the atomic configurations with local energy minima were subsequently selected as the equilibrium structures.

Figure 1 shows thus obtained the lowest energy grain boundary structure predicted by the lattice statics calculations [15]. The grain boundary excess energy was calculated to be  $3.01$  J/m<sup>2</sup>, and the lowest energy grain boundary structure had a rather large boundary expansion of  $1.00\text{\AA}$ , resulting in the formation of slightly large free volumes at the core of the boundary. The open spaced structures at the boundary core in real material may arise as channeling contrast on the HRTEM image where there are no atomic columns. Such contrast would make the interpretation of experimental HRTEM image be complicated, and require extensive image simulation in various kinds of possible structure models to determine the real atomistic core structures. To avoid such ambiguity, the atomic-resolution high-voltage electron microscopy (ARHVEM) was applied to directly determine the atomic column of cation sublattice at the present grain boundary. Cross-sectional HRTEM observations were then mainly carried out by a JEOL JEM-ARM1250 (1250 kV) transmission electron microscope to directly image the atomic column structure of the boundary. In this case, the thickness of the sample specimen was controlled to be as thin as about  $4$  nm, and the image was taken under near the Scherzer defocus of about  $-38$  nm, so that the atomic

columns can be imaged as black dots reflecting their potentials.

Figure 2(a) shows the ARHVEM image of the  $\Sigma = 9$ ,  $\{221\}$  grain boundary [15]. As can be seen in the image, the black dots were imaged slightly elongated in the  $[001]$  directions. This is because the anion sites are located very close to the cation sites in this direction. Since the open spaced cation sublattice structure can be directly observed in the micrograph, this boundary is confirmed to have a periodical array of asymmetrical structure units along the grain boundary, as indicated by the solid lines in Fig. 2 (b). Fig. 2(c) shows the calculated HRTEM image based on the predicted model as shown in Fig. 1. The simulated image approximately agrees with the experimental image, as for the periodical array of asymmetrical structure units. The cation sites with different coordination state are accumulated along the calculated  $\Sigma = 9$  grain boundary structure, indicated by the solid arrows in Fig. 1. These sites have seven-fold coordination of oxygen ions, and almost keep the cubic polyhedra. The density of the coordination deficient sites is considered to be related to the grain boundary energy in zirconia ceramics.

### ELNES interpretation

Microscopy approach is very useful for obtaining information about the projected atomic structure of the specimen, but EELS is also useful to analyze, not only structures but also chemical composition and bonding states from the electron illuminated area. Typically, the near edge fine structure of the EEL spectrum (ELNES) is used for the fine scale characterizations. Since ELNES arises from the electron transition from a core-orbital to the unoccupied bands, the spectral features of ELNES reflect the unoccupied partial density of states (PDOS) of the objective atom. ELNES therefore contains a wealth of information on the bonding and electronic structure

around the target atom. In order to quantitatively interpret ELNES, theoretical calculations using a first principles method are needed. To obtain the wave function at the initial state and the final state, a first-principles band structure calculation using the orthogonalized linear combinations of atomic orbitals (OLCAO) method was employed. The OLCAO method is a density functional theory (DFT) based on the local density approximation (LDA) [20]. In the electron transition process, an electronic hole is generated at a core orbital, which is called core-hole. The attractive potential from the nucleus becomes intense and the wave-function is more localized at the nucleus by the presence of the core-hole. The core-hole effect has been shown to greatly affect the accuracy of which the EEL spectral features can be reproduced [21,22]. In this study, the core-hole effect was fully taken into account in the self-consistent iterations by removing an electron at the core orbital and putting it at the lowest band. In order to introduce the core-hole, only the core orbital of the core-holed atom is excluded from the orthogonalized process. A sufficiently large supercell is also necessary to minimize the interaction of neighboring core-holed atoms in the adjacent cells. Figure 3(a) shows the experimentally obtained O-K ELNES for  $\text{SiTiO}_3$ . Supercells of 135 atoms were constructed by the  $3 \times 3 \times 3$  of the unit cells for  $\text{SrTiO}_3$ . By employing such supercells, approximately  $10\text{\AA}$  distance can be made among the core-holed atoms. The four irreducible k-points were used for the self-consistent iteration for the  $\text{SrTiO}_3$  electronic structure, respectively. Both the final and the ground states were separately calculated. The theoretical transition energy was evaluated by the subtraction of the total energy at the ground state from that of the final state. Each transition probability is broadened using the Gaussian function of  $\Gamma = 1.0$  eV for comparison with the experimental spectrum. In order to calculate the high resolution spectrum, eight

k-points were employed.

To demonstrate the importance of a sufficiently large supercell while using the core-hole methodology, the size dependence of the supercell on the calculated O-K ELNES spectra of SrTiO<sub>3</sub> is shown in Fig. 3(b) [6]. All spectra were calculated using the above method. A small supercell results in the inaccuracy of both the peak positions and relative intensities of the peaks. Agreement is satisfactorily achieved at a size of 135 atoms. The calculated spectrum at the ground state is also shown in Fig. 3(c). The spectrum at the ground state is calculated from the transition probability between the core-orbital to the conduction band both at the ground state. It is found that the spectral features change by the introduction of the core-hole. A sufficiently large supercell and the introduction of core-hole are thus the key for the accurate reproduction of ELNES spectra through first principles calculations.

### TEM In-Situ Characterization

It is important to clarify the internal structure of crack tips in ceramics for a fundamental understanding of fracture phenomena. A so-called process zone is considered to exist at the crack tip. However, the nature of the zone and also the atomic structure of the crack wall have not been clarified. It is quite possible that, using static methods to observe a pre-cracked tip by TEM, the structure of the crack tip changes during specimen preparation, for example by ion-beam thinning. In contrast, in-situ TEM methods for observing the fracture behavior are very effective in clarifying the microstructure of a crack wall, because the crack can be dynamically produced to form a fresh surface in a TEM. TEM in-situ straining experiments have already been accomplished to obtain very valuable information. There are, however, few reports on experimental TEM studies of the crack tip and wall in brittle ceramics.

In this study, a crack was introduced in silicon nitride ceramics by in-situ TEM straining experiments [7,8]. The method for the observations was the crack-induced tension (CIT) method [23]. This method employs the micro-indentation in a TEM, which means that the compressive force of the indenter makes a tensile force perpendicular to the crack. Figure 4 shows the TEM holder with CIT method. A tensile force is applied to the specimen by the nano-indenter. The introducing rate of the indenter is driven by a micro-step motor or piezo actuator which can be precisely controlled outside of the TEM. When the stress intensity factor  $K_I$  reaches to the critical value  $K_{IC}$ , the crack propagates.

Figure 5 (a) shows a bright field image of a typical transgranular crack in Si<sub>3</sub>N<sub>4</sub> ceramics obtained by the present in-situ straining TEM experiment [7]. The corresponding selected area electron diffraction pattern (SADP) taken from this grain is shown in Fig. 5 (b), indicating that the Si<sub>3</sub>N<sub>4</sub> grain was observed along the [0001] direction. It can be seen that no dislocations were observed around the crack and the fractured surfaces are sharp and straight, as can be expected from the brittle fracture. Figure 5 (c) shows the HREM micrograph of the crack walls shown in Fig. 5 (a). In the observed

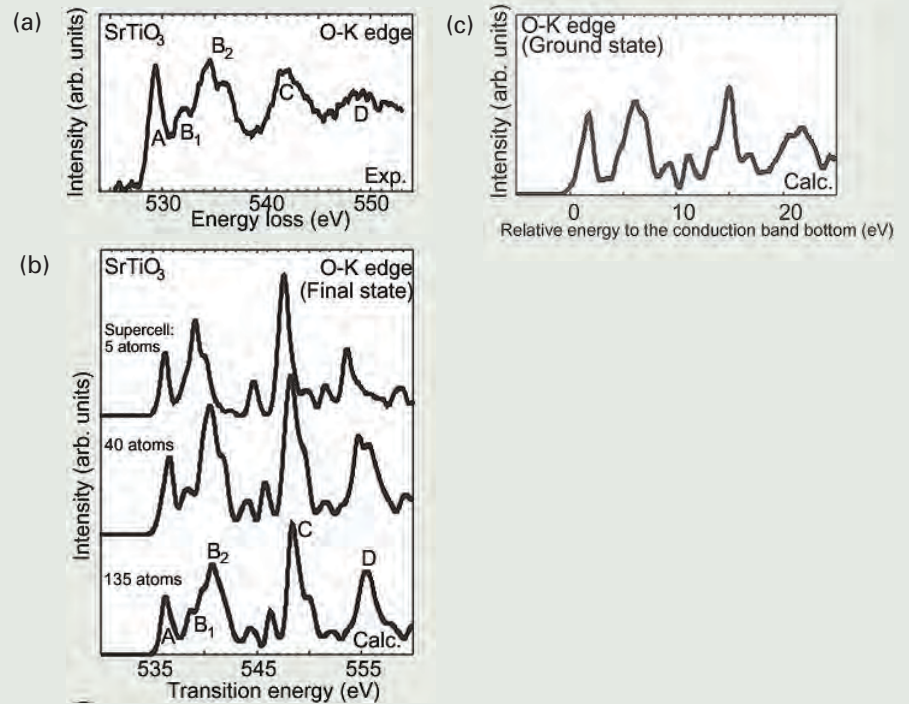


Fig. 3 Effect of calculation size and core-hole to the O-K ELNES from SrTiO<sub>3</sub>. (a) The experimental O-K ELNES from SrTiO<sub>3</sub>. (b) The calculated spectra at the final state using 8 atom, 40 atom, and 135 atom supercells. (c) The calculated spectrum at the ground state.

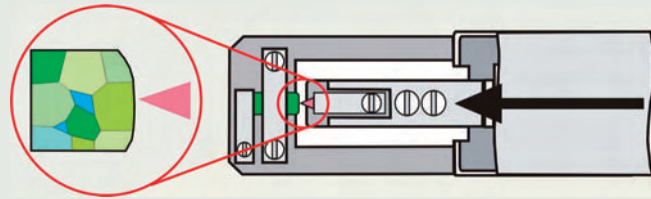


Fig. 4 TEM in-situ straining holder to apply stress to a specimen by introducing the nano-indentation which is precisely controlled by a piezo actuator (CIT method).

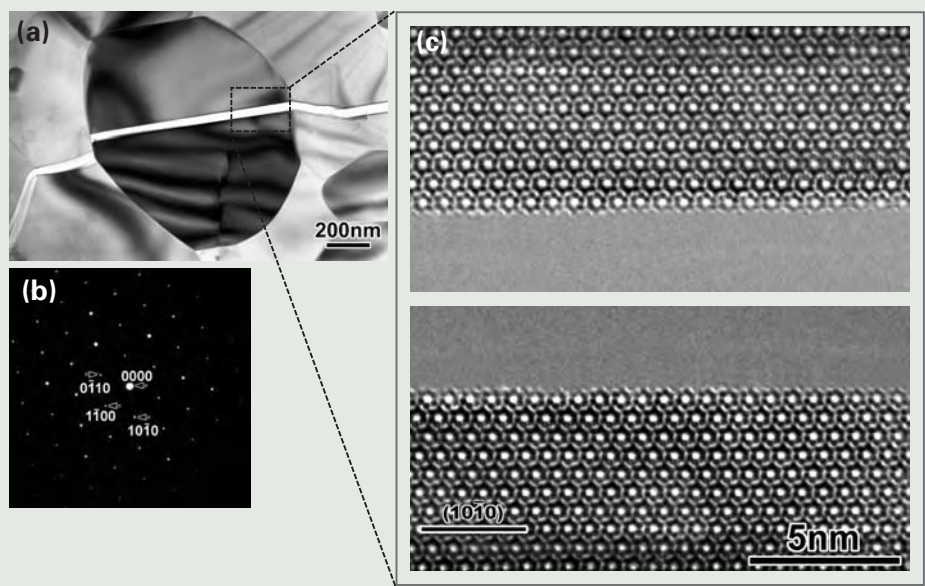


Fig. 5 (a) Bright field image of a transgranular crack in Si<sub>3</sub>N<sub>4</sub> ceramics, (b) the selected area electron diffraction pattern from the Si<sub>3</sub>N<sub>4</sub> grain at the center of this figure and (c) HREM micrograph of the crack walls in Si<sub>3</sub>N<sub>4</sub>, indicating that the crack propagated toward [1̄120] and the cleavage plane was parallel to the (1̄100) plane.

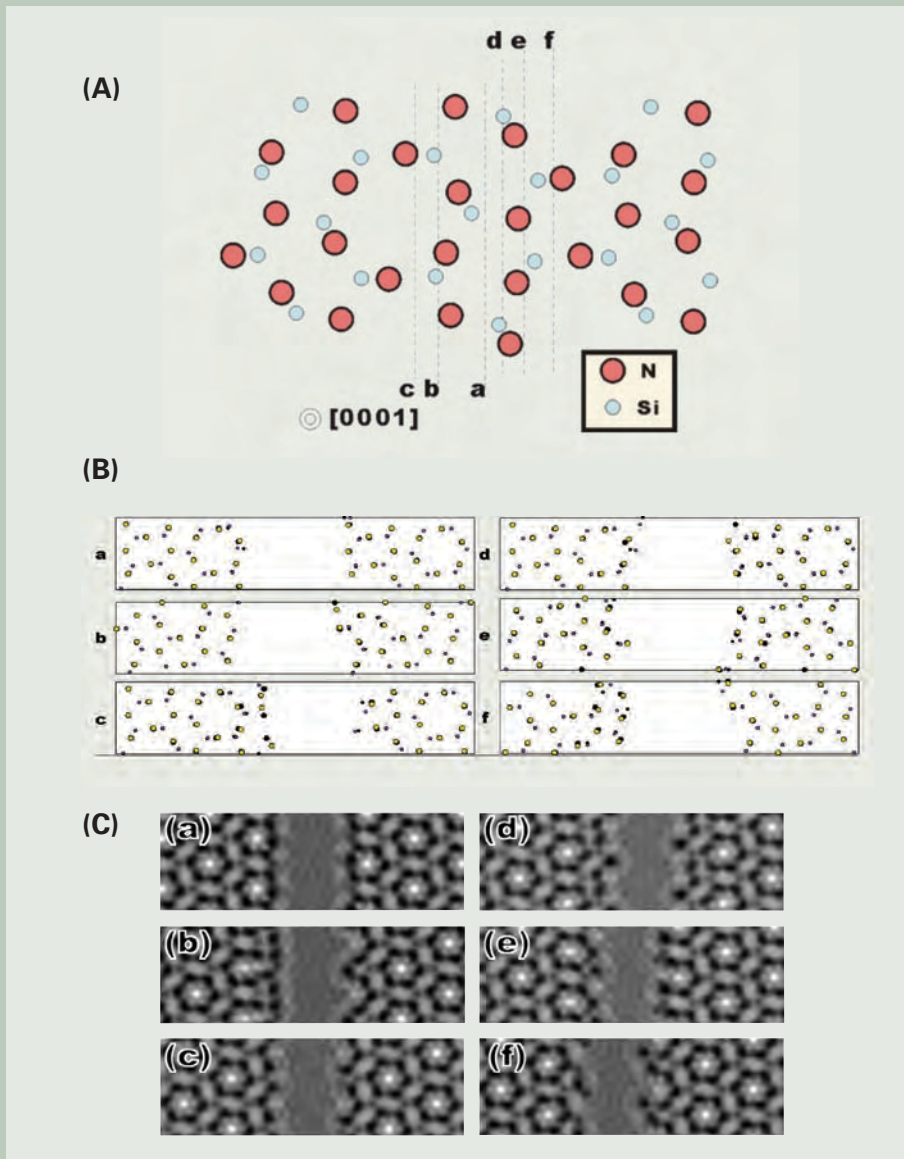


Fig. 6 (A) Schematic illustration of Si<sub>3</sub>N<sub>4</sub> crystal projected along the [0001] direction, indicating six possible models (a-f) for the cleavage fracture. (B) The most stable surface structures which were predicted by a first principles calculations, corresponding to the respective 6 kinds of fracture models. (C) HREM simulated images based on the respective fracture models of (a) to (f) in (B).

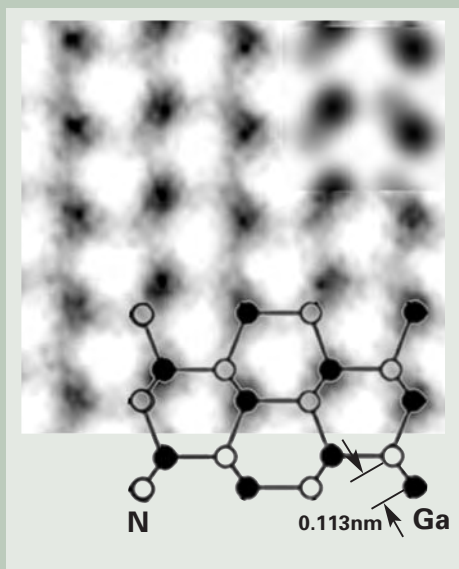


Fig. 7 HREM micrograph of GaN taken by ARHVEM, showing that Ga and N can be resolved in the image. Insets are the simulated image obtained at -35 nm defocus and 3.2 nm thickness, and a schematic of the atomic structure model.

region, the crack walls are atomically flat and atomic steps were not observed on either side. It is found that the transgranular fracture in Si<sub>3</sub>N<sub>4</sub> grain propagated toward  $[\bar{1}\bar{1}20]$  and the resultant crack walls were parallel to (1 $\bar{1}00$ ) plane. In the transgranular fracture, several kinds of (1 $\bar{1}00$ ) planes can be considered as the atomic planes. In order to be considered as the fracture plane. In order to determine the detailed structures of the crack walls at an atomic level, 6 kinds of fracture models along (1 $\bar{1}00$ ) planes can be considered as shown in Fig. 6A (a) to (f) [7]. In the schematic illustration of Si<sub>3</sub>N<sub>4</sub> crystal shown in Fig. 6 (A), large and small circles correspond to Si and N atoms, respectively. Fig. 6 (B) show the most stable (1 $\bar{1}00$ ) surface structures which were predicted by the first principles calculations, corresponding to the respective 6 kinds of fracture models. The atomic relaxation is thus taken into account in all models. The HREM simulated images obtained from these models are shown in Fig. 6 C(a) to (f). The conditions of crystal thickness and defocus values for HREM simulation were 3 nm and -47 nm, respectively. As can be seen in Figs. 6 C (a) to (f), the image contrasts near the cleaved surfaces were different between these possible cleavage planes. In addition, from close comparison between the experimental and simulated images, it is confirmed that the model "a" shown in Fig. 6 (A) was in good agreement with the experimental image. That is, the cleavage fracture occurs along the double silicon layers on the (1 $\bar{1}00$ ) plane. The terminated atomic structure can be thus evaluated by directly observing the crack wall just after crack is propagated.

## Ultra HREM

As mentioned above, HREM is very useful to characterize the atomic structures in ceramics. However, the point-to-point resolution of a conventional HREM is usually 0.17-0.20 nm, and it is impossible to distinguish the species of atoms which are located closer within the resolution. In the recent nano-characterization, we sometimes need to directly observe light elements such as oxygen, carbon and nitrogen which are main constituent atoms in ceramics. The light elements are frequently bonded to neighboring cations at the interatomic distance less than 0.1 nm, and the ultra high resolution is, therefore, needed to discriminate the atoms.

GaN films are the potential candidates to be applied to optical and electronic devices [24]. An epitaxial wurtzite GaN (0001) film grown on a sapphire (0001) substrate has a polar structure of which the axis is parallel to the growth direction. Recently, control of the lattice polarity in III-nitride films has become a topic of interest due to its significant influence on the optical and electrical properties of the films. The polarity in GaN films is one of the important keys to determine the properties, however, the polarity cannot be identified by conventional TEM technique. In order to determine the polarity, coaxial impact collision ion scattering spectra (CAICISS), reflection high-energy electron diffraction (RHEED) and convergent beam electron diffraction (CBED) have been applied, however, they provide only average information about the lattice polarity in the illuminated area. To discriminate

between Ga and N, and hence to determine the absolute polarity, a resolution of 0.113 nm is needed. We proposed the application of ARHVEM to characterize the GaN film [9, 25]. The point-to-point resolution of the electron microscope is about 0.1 nm. ARHVEM, therefore, can be used to directly observe the Ga atoms and N atoms on only one image and determine the absolute polarity without the complicated image analysis required in conventional HREM.

**Fig.7** shows HREM image of GaN sample observed by ARHVEM (JEOL JEM-ARM1250) at an accelerating voltage of 1250 kV. Spherical and chromatic aberration constants of the objective lens are designed to be  $C_s=1.4$  mm and  $C_c=2.4$  mm, respectively. The HREM image was observed along the  $\langle 11\bar{2}0 \rangle$  zone axis. The smallest intercolumn distance between Ga and N in this orientation is 0.113 nm. Initially, the condition of GaN imaging was systematically checked, because there has been no report on the direct imaging of Ga and N atoms in GaN. In Fig. 7, the inset at the upper right in the micrograph is a simulated image obtained using an electron microscopy software. The simulated image with Scherzer defocus and 3.2 nm thickness suggests that Ga and N atomic columns can be imaged as darker and lighter spots, respectively. The experimental image in Fig. 7 was taken under the similar defocus and thickness conditions as the calculation. In the experiment, a focus series around the Scherzer condition was taken, and the thickness of the sample was systematically checked by comparing the experimental and calculated images depending on the amount of defocus. The experimental image is in good agreement with the calculated image and it was found to be possible to discriminate between Ga and N atoms by ARHVEM.

## Low Electron Dose HREM

Recently, some soft ceramics such as zeolites, bioceramics and so on have been paid much attention because of their special functional properties for environmental assessment. The properties of such soft materials are also related to their atomic structures, and HREM is one of the most effective methods to characterize such materials. However, it has been hard to characterize the soft materials by HREM, because the soft materials are usually very sensitive to electron beam irradiation. They have metastable structures and weak chemical bonding and quite easily damaged by electron irradiation to form an amorphous structure. Then, it is usually impossible to record an image under ordinary conditions of HREM observations (beam current density  $>10$  A/cm<sup>2</sup>). Several researches have been performed on zeolites using ordinary HREM with a special technique [26]. However, this technique involves taking a picture with film very quickly before irradiation damage occurs and cannot be used for normal observation.

A recording technique for TEM images with a slow-scan charge-coupled-device (CCD) camera (SSC camera) has been developed so far, which makes it possible to observe using HREM with a low electron beam dose [27]. An example of observation of the channel structures in zeolite Y is introduced here. HREM observations were performed on a con-

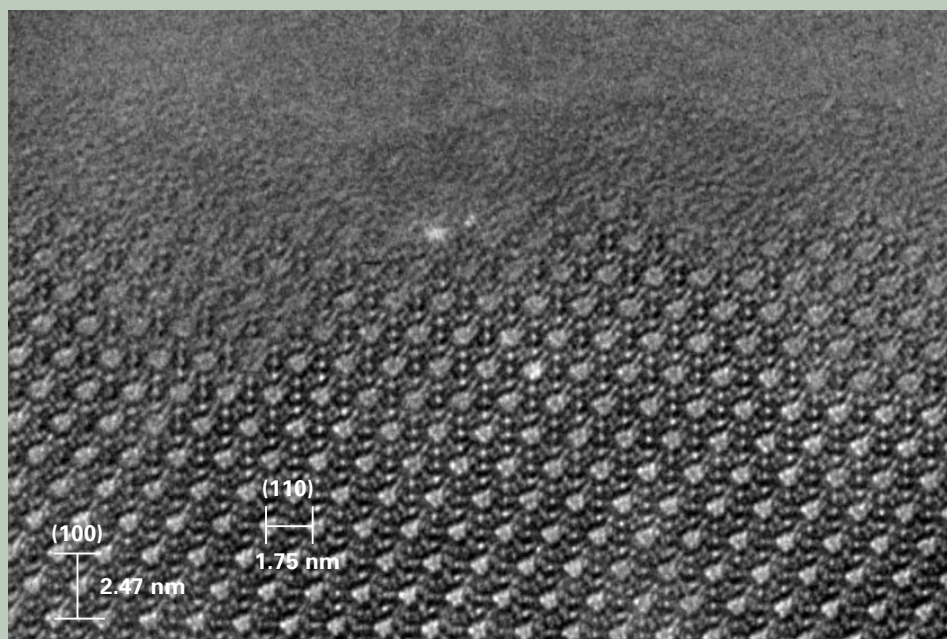


**Fig. 8** HREM micrograph of the channel structure in zeolite Y with the incident beam parallel to the  $[110]$  zone axis, showing the presence of 12-member rings as large bright spots.

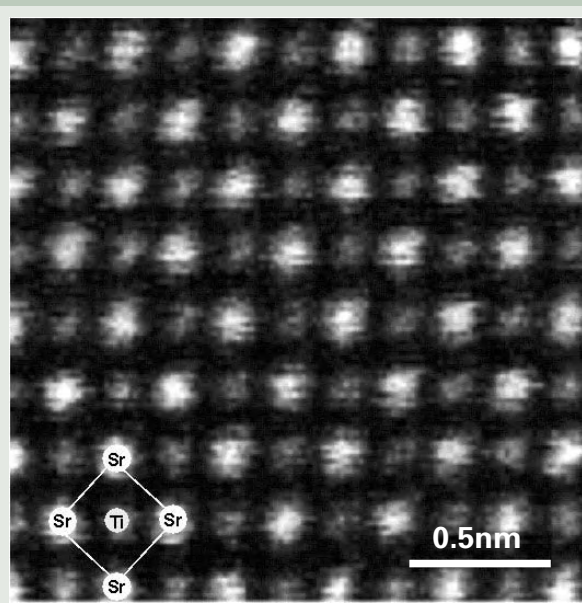


**Fig. 9** HAADF-STEM (Z-contrast) image for SrTiO<sub>3</sub> projected along  $[001]$  direction, in which bright and gray contrasts correspond to Sr and Ti, respectively (taken by JEOL JEM-2200FS with Cs corrector).

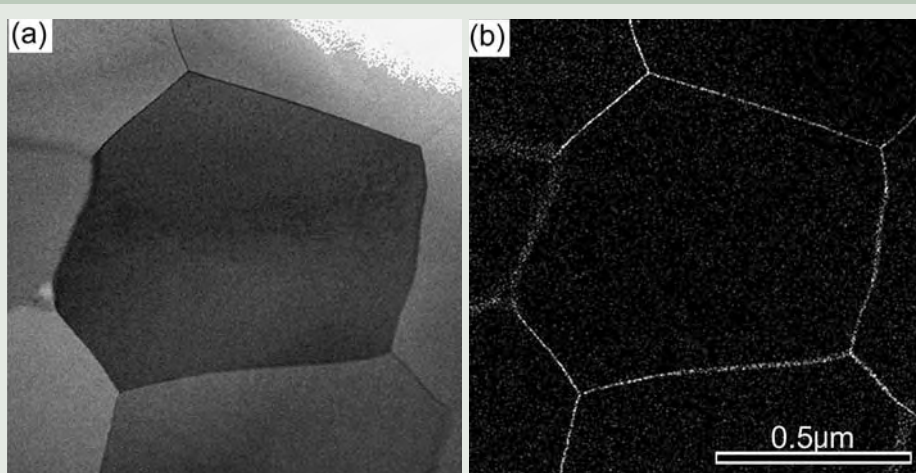


**Fig. 10** (a) STEM image and (b) Lu-K $\alpha$  image obtained by STEM-EDS mapping with the probe size of 0.5 nm using a small Cs pole-piece for the grain boundary in the Lu<sub>2</sub>O<sub>3</sub> doped Al<sub>2</sub>O<sub>3</sub>.

ventional HREM operating at 200 kV. A SSC camera was attached to the microscope, and the images were recorded to the computer in real time. The SSC camera has a sensitivity more than several ten times greater than that of ordinary film and is designed in such a way that the readout noise is less than 1 count rms (at 350k pixel/s sampling rate) by cooling the CCD to  $-30^{\circ}$  to  $-40^{\circ}\text{C}$ . Furthermore, its dynamic range is as wide as 4000, and the linearity for the recording is quite accurate with an error less than 1% of full range. The electron dose used for the present HREM studies was less than about  $0.2\text{A}/\text{cm}^2$ , which corresponds to 1/50 of that for the ordinary HREM observations. **Fig.8** shows a HREM micrograph for zeolite Y (FAU) taken along the [110] direction [10]. Several sizes of white dots are seen in the figure. The zeolite Y has zinc-blend structure consisting of  $\beta$ -cages, and is stacked as ...ABCABC... in the [111] direction. The  $\beta$ -cages are bonded with 6-member rings to form 12-member rings with a diameter of 0.74nm in the [111] direction. Since these 12-member rings lie along the [110] direction to make a large channel, observation of the channel in zeolite Y was performed with the incident beam parallel to the [110] direction. The biggest white dots correspond to the channels of 12-member rings. Thus, it is found that the small dots around the biggest white dots correspond to 4- and 6-member rings in the  $\beta$ -cage.

## Scanning Transmission Electron Microscopy

STEM has been developed to obtain finely focused electron probe less than 0.2 nm, and has been applied for characterizing materials. Particularly, a high-angle dark-field STEM (HAADF-STEM) has been used as a kind of atomic-resolution imaging [28-32]. The contrast obtained by HAADF-STEM reflects the atomic number (Z), and hence the contrast is called Z-contrast. In addition, recent development of Cs correction technique enables us to obtain further fine probe size less than 0.1 nm, and has been paid much attention for materials scientists [31,32]. **Figure 9** shows an example of Z-contrast obtained by STEM with Cs-corrector for  $\text{SrTiO}_3$  projected along [001] direction, in which bright and gray contrasts correspond to Sr and Ti, respectively. Z-contrast is thus expected to be very powerful technique rather than HREM for characterizing ceramics, however, one of the weak points is in observing light elements such as oxygen, nitrogen and carbon because the scattering factor of these elements are small. So far, ARHVEM has been superior to Z-contrast on this point, but very recently, the group of Pennycook experimentally showed that light elements also can be directly imaged by BF-STEM image using a Cs corrector [11].

In order to obtain a nano probe smaller than 1 nm in a transmission electron microscope, the field emission gun is needed because the size of illumination is small and the brightness is high. Grain boundary composition and chemical bonding state for several ceramics have been successfully investigated by the nano-probe using the small Cs pole-piece. **Fig.10** shows (a)STEM image and (b) Lu-K $\alpha$  image obtained by STEM-EDS mapping with

the probe size of 0.5 nm for the grain boundary in the  $\text{Lu}_2\text{O}_3$  doped  $\text{Al}_2\text{O}_3$  [33]. It can be clearly seen that the continuous segregation layer is formed along the grain boundary. The thickness of the segregation layer is about 1 nm. This kind of EDS mapping is also an advantage of STEM technique.

## Summary

TEM is a very powerful technique to characterize microstructures in advanced ceramics. However, we frequently encounter difficulties which cannot be solved by conventional techniques. The difficulties are in quantitative analysis, resolution of in-situ HREM, limitation of atomic resolution, spatial resolution and so on. In this case, we need to overcome the difficulties by developing and contriving the method to procure essential information on microstructures at the necessary conditions. In this article, some attempts were demonstrated to show quantitative analysis for grain boundary atomic structures and ELNES, in-situ straining TEM, ultra HREM, low dose HREM, high spatial analytical STEM. Now, TEM has thus many functions, and will add another functions in the near future. Taking account of recent improvements, TEM is not only a microscope, but also plays a role as a nanolaboratory to process nano-materials and to characterize microstructures in dynamic environments. That is, the fields of TEM is gradually transferring from "Seeing is believing" to "Seeing is creating". This approach will create a new field of TEM characterization, and contribute to the development for the nano-technology in the near future.

## Acknowledgements

The author would like to acknowledge the collaboration of N. Shibata, C. Iwamoto, T. Mizoguchi, S. Ii, J. Buban, H. Yoshida, K. Matsunaga, T. Yamamoto (U. Tokyo), Y. Sasaki, T. Suzuki, T. Hirayama (JFCC) and H. Sawada (JEOL). A part of this work was supported by the Special Coordination Funds of the Ministry of Education, Culture, Sports, Science and Technology of the Japanese Government, and also Japan Society for the Promotion of Science, Grant-in-Aid for Scientific Research.

## References

- [1] e. g.: Proc. 14th conf. Electron Microsc. (ICEM), Cancun, Mexico, IOP Pub. Ltd, Danvers USA (1998)
- [2] Y. Ikuhara, *J. Ceram. Soc. Jpn.*, **109**, S110-S120 (2001)
- [3] K. Matsunaga, H. Nishimura, T. Saito, T. Yamamoto and Y. Ikuhara, *Philos. Mag.*, **83**, 4071-4082 (2003)
- [4] F. Oba, H. Ohta, Y. Sato, H. Hosono, T. Yamamoto and Y. Ikuhara, *Phys. Rev. B*, **70**, 125415 (2004)
- [5] T. Mizoguchi, M. Sakurai, A. Nakamura, K. Matsunaga, I. Tanaka, T. Yamamoto and Y. Ikuhara, *Phys. Rev. B* **70**, 153101-1-4 (2004).
- [6] T. Mizoguchi, J. P. Buban, K. Matsunaga, T. Yamamoto and Y. Ikuhara, *Ultra-microscopy*, In press (2005)

- [7] S. Ii, C. Iwamoto, K. Matsunaga, T. Yamamoto, M. Yoshiya and Y. Ikuhara, *Phil. Mag.*, **84**, 2767-2775 (2004)
- [8] S. Ii, C. Iwamoto, K. Matsunaga, T. Yamamoto and Y. Ikuhara, *J. Electro. Micros.*, **53** (2), 121-127 (2004)
- [9] C. Iwamoto, X. Q. Shen, H. Okumura, H. Matsuhata and Y. Ikuhara, *Appl. Phys. Lett.*, **79**, 3941-3943 (2001)
- [10] Y. Sasaki, T. Suzuki, Y. Ikuhara and A. Saji, *J. Am. Ceram. Soc.*, **78**, 1411-13 (1995)
- [11] Proc. Microscopy & Microanalysis 2004, Ed. M. Anderson, R. Price, E. Hall, E. Clark and S. Mckernan, Savannah, Georgia, Cambridge Univ. Press (2004)
- [12] Y. Ikuhara, N. Shibata, T. Watanabe, F. Oba, T. Yamamoto and T. Sakuma, *Ann. Chim. Sci. Mater.*, **27**, S21-30 (2002)
- [13] H. Nishimura, K. Matsunaga, T. Saito, T. Yamamoto and Y. Ikuhara *J. Am. Ceram. Soc.*, **Vol.86**, No. 4, 574-580 (2003)
- [14] Y. Sato, T. Mizoguchi, F. Oba, M. Yodogawa, T. Yamamoto and Y. Ikuhara, *Appl. Phys. Lett.*, **84** (26): 5311-5313 (2004)
- [15] N. Shibata, F. Oba, T. Yamamoto and Y. Ikuhara, *Phil. Mag.*, **84** (23): 2381-2415 (2004)
- [16] J. D. Gale, *J. Chem. Soc. Faraday Trans.*, **93**, 629 (1997).
- [17] D. Wolf, 1984, *J. Am. Ceram. Soc.*, **67**, 1 (1984)
- [18] S. Fabris and C. Elsässer, *Phys. Rev. B.*, **64**, 245117 (2001)
- [19] G. V. Lewis and C. R. A. Catlow, *J. Phys. C: Solid State Phys.*, **18**, 1149 (1985).
- [20] W. Y. Ching, *J. Am. Ceram. Soc.* **73**, 3135 (1990).
- [21] I. Tanaka, H. Araki, M. Yoshiya, T. Mizoguchi, F. Oba, and H. Adachi, *Phys. Rev. B* **60** (1999) 4944.
- [22] T. Mizoguchi, I. Tanaka, M. Yoshiya, F. Oba, K. Ogasawara, and H. Adachi, *Phys. Rev. B* **61** (2000) 2180.
- [23] Y. Ikuhara, T. Suzuki and Y. Kubo, *Philos. Mag. Lett.*, **66**, 323-327 (1992)
- [24] S. Nakamura, M. Senoh, S. Nagahama, N. Iwasa, T. Yamada, T. Matsushita, Y. Sugimoto and H. Kiyoku, *Appl. Phys. Lett.*, **70**, 2753-2756 (1997)
- [25] C. Iwamoto, X. Q. Chen, H. Okumura, H. Matsuhata and Y. Ikuhara, *J. Appl. Phys.*, **Vol. 93**, No.6, 3264-3269 (2003)
- [26] O. Terasaki, *Acta Chem. Scand.*, **45**, 785-90 (1991)
- [27] P. E. Mooney, G. Y. Fan, C. E. Meyer, K. V. Truong, D. B. Bui and O. L. Krivanek., p.164, Vol.1, in Proc. 12th ICEM (Seattle, WA, 1990)
- [28] S. J. Pennycook and D. E. Jesson, *Phys. Rev. Lett.*, **64**, 938 (1990)
- [29] N. D. Browning, M. F. Chisholm and S. J. Pennycook, *Nature*, **366**, 143-146 (1993)
- [30] Y. Yan, M. F. Chisholm, G. Duscher, A. Maiti, S. J. Pennycook, and S. T. Pantelides : *Phys. Rev.*, **81**, 3675-3678 (1998)
- [31] E. Abe, S. J. Pennycook and A. P. Tsai, *Nature*, **421**, 347 (2003)
- [32] N. Shibata, S. J. Pennycook, G. S. Painter and P. F. Becher, *Nature*, **428** 730-733 (2004)
- [33] H. Yoshida, Y. Ikuhara, and T. Sakuma,, *Phil. Mag. Lett.*, **79**, 249-256 (1999)

# Advanced Analysis Technology Supporting SiP

Ken Sugiura

Fukuryo Semiconductor Engineering, Inc. Analysis and Evaluation Center

## Introduction

SiP (System in a Package) is an indispensable packaging technology for achieving small sizing and high-functionality of mobile equipments. Packaging density of devices used for mobile equipment is ever increasing. For example, it is prospected that the minimum pitch of W/B (Wire Bonding) will be reduced to 20  $\mu\text{m}$  from current 40  $\mu\text{m}$  by 2008 and that the electrode pattern pitch of full grid type CSP (Chip Size Package) will also be reduced to 100  $\mu\text{m}$  from current 150  $\mu\text{m}$  by 2008 [1]. As the pattern pitch is narrowed, the sizes of bonding pad and the land on which a metal bump is placed are also reduced, thus, such failure modes as peeling of W/B, disconnection of metal bumps, imperfect plating and abnormal precipitation from plating have become a serious problem than ever before.

In this paper, we will introduce some examples of failure analysis relating to the defects in electrical connecting and plating that frequently occur in high density packaged electrical devices and also describe applications of various analysis equipments for such analytical use.

## Features of and Comparison Between the Cross Sectional Observation Methods

The cross sectional observation is a base for analyzing the failure modes in packaged devices. Various methods such as mechanical polishing, Microtome, FIB (Focused Ion Beam) and ion beam processing are utilized depending on respective purposes. Mechanical polishing method is widely utilized because it is possible to observe wide areas and the equipment is not expensive in spite that it requires high-level polishing technique like workman. Especially, when observing the

boundary state of intermetallic compound (IMC) and analyzing the composition of material, the mechanical polishing is the most convenient method and it is not technologically impossible to observe the cross-section of ultra-micro bump with a thickness less than 20  $\mu\text{m}$ . **Figure 1** shows an image of a cross-section of IMC formed at the boundary between a solder bump and an interposer. Regardless of the kind of Ni-plating, that is, regardless whether it is formed by electroless Ni-P plating or by electrolytic Ni plating, IMC with a composition of  $\text{Ni}_3\text{Sn}_4$  at the boundary between eutectic solder is formed, but their forms are totally different. In case of electroless Ni-P plating, the IMC takes a pole-like or needle-like form, while in case of electrolytic Ni plating, it takes a layer-like form. In addition, it is known that in case of electroless Ni-P plating, a P-enriched layer is formed at the surface of Ni-P plating because only Ni element is consumed for diffusive reaction with Sn element. This status can also be clearly observed by the mechanical polishing method.

Since information obtained by mechanical polishing method depends greatly on the polished aspect state, it is impossible to observe and discuss the crystal structure or cracks on the polished aspect on which mechanical damages such as dents remain.

FIB has also been established as one of the cross-sectional observation methods for analyzing the packaged devices because it gives relatively small damages to samples and it is easy to handle. Especially when discussing the metallic crystal structure, channeling images obtained from FIB method gives us very effective information. But, since the area processed by this method is limited to 100  $\mu\text{m}$  in width and 20  $\mu\text{m}$  in depth, it is not appropriate to apply this FIB method to obtain information from wide area of sample. **Figure 2** shows the channeling images obtained from various plating conditions. A method for developing the sample with a cross-section using an ion beam processing has been developed recently [2]. Since processing area of CP (Cross-section Polishing) is relatively wide, about 300  $\mu\text{m}$  in

width and 200  $\mu\text{m}$  in depth, CP method enables the wider area to be processed flatter and smoother than FIB method, especially effective for pre-processing the sample to obtain a reflected electron image or EBSP (Electron Backscatter Diffraction Pattern).

**Figures 3 and 4** show the reflected electron image and EBSP image of Au-ball, respectively. It can be observed that the crystal located at the center of the ball became enlarged by thermal stress of bonding process and that fine crystals were formed just under the capillary where a mechanical stress was applied. When processing a sample that simultaneously includes both the soft and hard materials and such metals as Sn and Ag of which etching rate is high with CP method, it should be noticed that beam damage may remain, making observation difficult.

## Identifying the Au-Al Compound

W/B using a high-purity Au wire is a method for electrically connecting the semiconductor chip to the substrate that holds the chip, and the state of Au-Al compound formed at the boundary between Au-ball and Al-pad is an important measure of reliability of devices.

Historically, EPMA (Electron Probe Micro Analysis) method has been utilized for identifying the Au-Al compound. However, since the thickness of compound layer just after bonding process is very thin, it has been very difficult to identify the compound in principle of EPMA measurement. FEAES (Field Emission type Auger Electron Spectroscopy) is good at analyzing a very small area with a diameter less than 1  $\mu\text{m}$ . Accuracy of quantitative determination of AES method is inferior to EPMA method, and it is said that AES method is not adequate to identify the IMC. But, high reliability can be obtained by executing comparative analysis against the standard materials. **Figure 5** shows a qualitative spectrum of Au-Al standard compound and Table 1 shows the results of semi quantitative determination that has corrected the relative sensi-

tivity for Au and Al.

Since, although the relative atomic ratio of Au and Al does not completely coincide with the ideal composition calculated, errors fall in the range of  $\pm$  few percents, we judged that it is possible to identify the Au-Al compound using this AES method. **Figures 6 and 7** show the composition of the compound formed after mold curing and after storage at 200°C for 168 hours, respectively.

The dominated layer after mold curing is  $Au_5Al_2$ , and there exists  $Au_4Al$  in Au side,  $Au_2Al$  and  $AuAl$  in Al side. The dominated layer after storage at 200°C for 168 hours changed to  $Au_4Al$  and there exists  $Au_2Al$  and  $Au_5Al_2$  remained around the ball. Change of the dominated layer is considered to result because a growing speed of compound by heating is limited to the diffusion speed of Au, and consequently, the  $Au_4Al$  as the most Au-rich layer was stabilized. On the other hand, defects are observed in the boundary between Au wire and  $Au_4Al$  layer, and since there exists strong Oxygen, it is considered that these defects are traces of compound's erosion caused by moisture included in mold resin. TEM (Transmission Electron Microscope) observation image of the defect is shown in **Fig. 8**. Defects are composed of three types of modes, Phase-A, Phase-B and Phase-C. AS shown by EDS profile in **Figs. 9 and 10**, it became clear that the dominant layer of Phase-B has a composition consisting of only Al and Oxygen without Au, and Phase-C that distributedly exists in Phase-B includes Au. Although it has been considered that the erosion of Au-Al compound is generally caused by Al-bromide as the result of a reaction between Br included in mold resin as a fire retarding material and  $Au_4Al$  [3].

But, in both of the above described FEAES and EDS methods, the energy positions of Br and Al overlap in the same location, it is impossible to detect the existence of Br. Therefore, we have confirmed the existence of Br in defects by EPMA analysis. **Figure 11** shows a EPMA profile. Br was not detected in **Fig. 11**. Thus, it was suggested that there is a

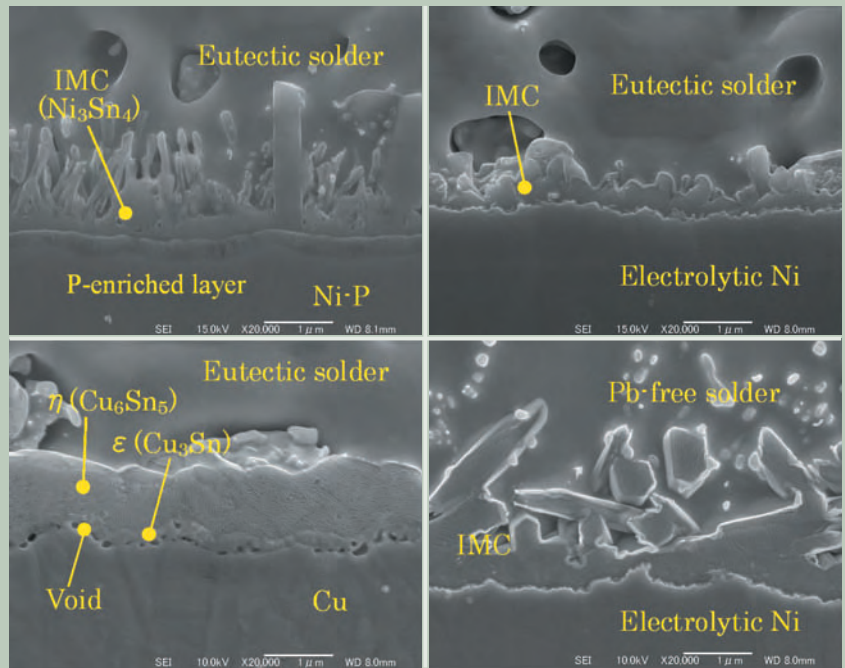


Fig. 1 State of forming of IMC (mechanical polishing  $\Rightarrow$  FE SEM).

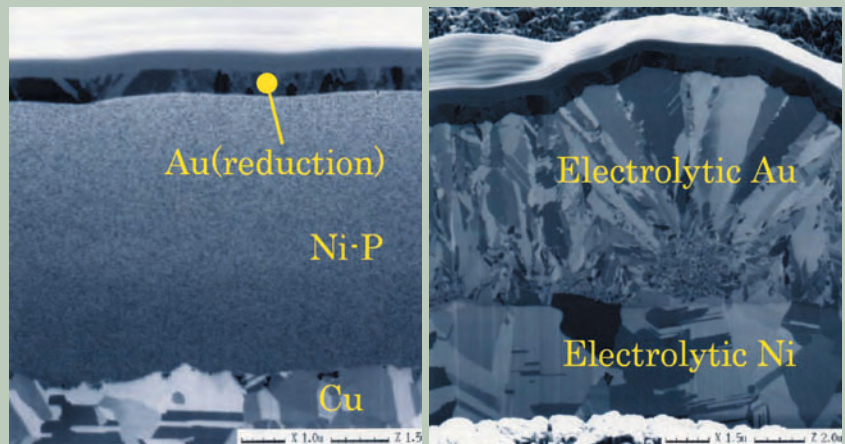


Fig. 2 Channeling images of electrode plating (FIB).



Fig. 3 Reflected electron image of Au ball (CP  $\Rightarrow$  FE SEM).

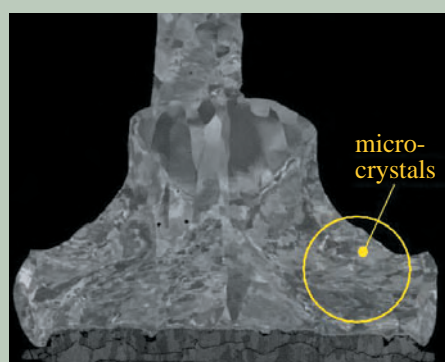


Fig. 4 BE-SEM image of Au ball.

possibility that erosion is not only accelerated by halogen element, but also promoted by just moisture as well.

### Analysis on peeling-off of electroless Au/Ni-P plating

Electroless Au/Ni-P plating is utilized for surface finishing of printed wiring boards including interposers.

Since the flash Au plating is formed by a substitution reaction with Ni, when an excess substitution reaction occurs, underlying Ni-P plating layer is pitted by corrosion causing peeling-off ultra-sonic bonding and degrada-

tion of the adhesion strength of solder [4].

**Figures 12 to 5** show the AES depth profile and the surface state of Ni-P layer after removing the flash Au, in cases of normal plating and abnormal plating, respectively. In case of abnormal Au/Ni-P plating, P-enriched layer was observed at the boundary between Au and Ni-P, and it was also known that carbon and oxygen exist in Ni-P plating layer. On the other hand, pitting corrosion was observed along the grain boundary on Ni-P surface after removal of Au.

**Figures 16 and 17** show the FIB cross-sectional images of the part where Au plating was peeled off and remained normally, respective-

ly. At the boundary between Au and Ni-P layers, an amorphous layer with 0.2  $\mu\text{m}$  thickness including a micro-void was observed, and it was confirmed that peeling off occurred at the boundary between Au plating layer and the amorphous layer.

Taking account of the state of pitting corrosion on the surface of Ni-P plating layer, AES analysis result and FIB cross-sectional image, we concluded that the amorphous layer is a Au/Ni substitution layer formed by an excess reaction and that the pitting corrosion observed at the surface of Ni-P layer after removal of Au is a trace that an excess reaction took place significantly along the grain boundary. In addi-

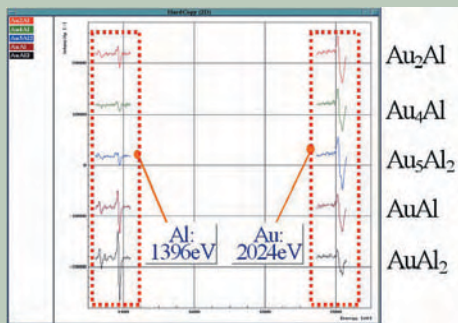


Fig. 5 Spectrum of Au-Al standard (FEAES).

Table. 1 Composition of Au-Al IMC.

Standard Sample	Atomic Concentration (at%)				IMC formation
	Ideal Concentration		Detection		
	Au	Al	Au	Al	
Au <sub>4</sub> Al	80	20	82	18	Au <sub>4</sub> Al
Au <sub>5</sub> Al <sub>2</sub>	71	29	75	25	Au <sub>5</sub> Al <sub>2</sub>
Au <sub>2</sub> Al	67	33	69	31	Au <sub>2</sub> Al
AuAl	50	50	50	50	AuAl
AuAl <sub>2</sub>	33	67	28	72	AuAl <sub>2</sub>

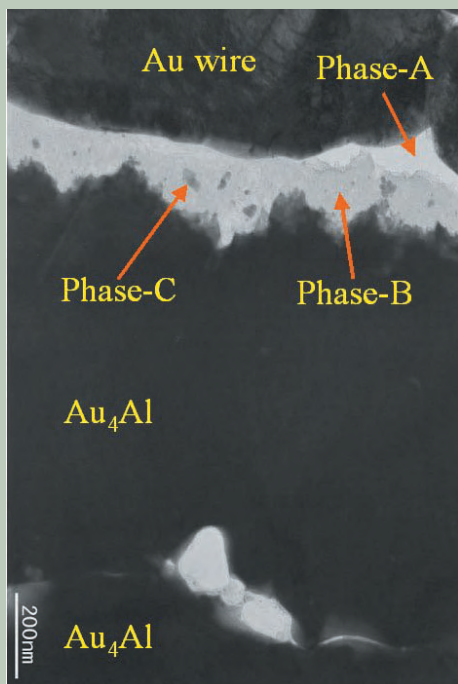


Fig. 8 TEM image of defect part.

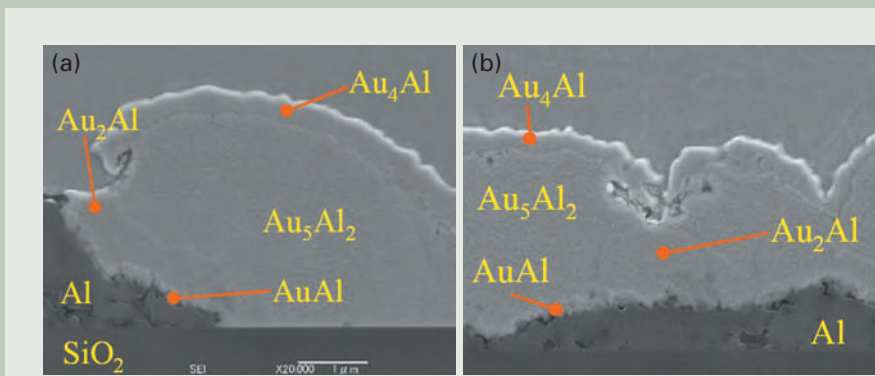


Fig. 6 (a) Compound composition around the Au ball (after molding).  
(b) Compound composition at the center area of Au ball (after molding).

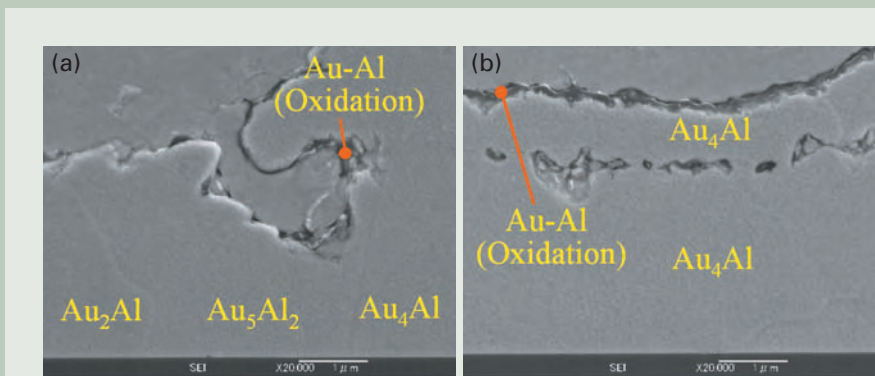


Fig. 7 (a) Compound composition around the Au ball (after 200°C × 168hrs).  
(b) Compound composition at the center area of Au ball (after 200°C × 168hrs).



Fig. 9 EDS profile of Phase-B.



Fig. 10 EDS profile of Phase-C.

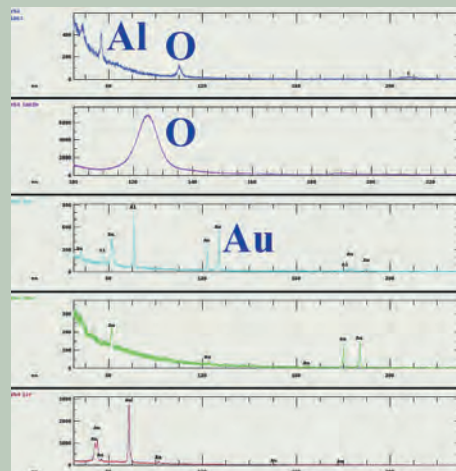


Fig. 11 EPMA profile of defect position.

tion, the excess reaction resulted from Ni-P layer including carbon. **Figure 18** shows an estimated structure of the Au exfoliated part. In order to accurately analyze the concentration distribution of carbon (C), sulfur (S) and oxide (O) of which abnormal eutectoid into Ni-P layer is concerned, we used SIMS (Secondary Ionization Mass Spectrometer) analysis. **Figures 19** and **20** show SIMS profiles of the normal and abnormal plating, respectively. The horizontal axis corresponds to concentration gradient in the depth direction. It is known that there is no difference in the concentration distribution of Au, Ni and P as the components of plating between normal

and abnormal plating, while the concentration of C, S and O elements included in abnormal plating are higher than that of normal plating.

Then, in order to clear the origin of these impurities, we tried to analyze organic components included in Ni-P solution that was used for processing the abnormal plating taking a standard Ni-P solution as a reference. As for the organic components with low boiling point, we applied GC/MS (Gas Chromatograph/Mass Spectrometer) analysis after solid-phase micro extraction. While, as for the organic components with high boiling point, we applied  $^{13}\text{C}$  FT-NMR (Fourier Transform-Nuclear Magnetic Resonance) analysis after

letting the residual material after heating and drying the plating solution dissolved into a heavy chloroform solution. **Figures 21** and **22** show the results of GC/MS and FT-NMR analysis on the used solutions.

No volatile components included regardless of the used solutions after bath-plating, and citrate, succinate, EDTA and ureic compound, etc. were detected as non-volatile components. On the other hand, from only the used solution, kinds of polyethylene-glycol-diacrylate, kinds of amino-alkyl-phenon, azobisisobutyronitrile and its resolvent were detected.

It is considered that the organic component detected from the only used solution was

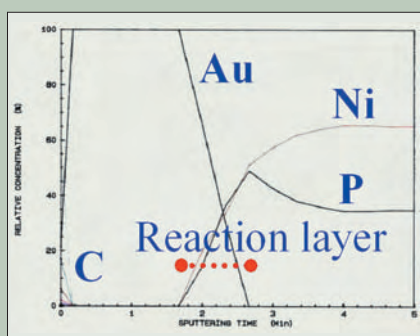


Fig. 12 Depth profile of normal plating (AES).

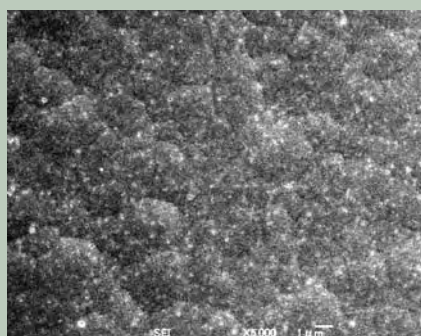


Fig. 13 Surface of normal plating (after removing Au).

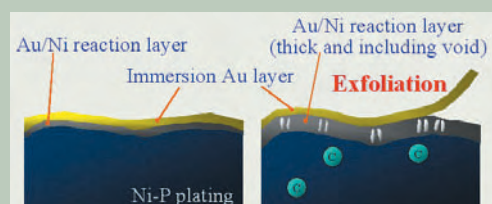


Fig. 18 Estimated structure of Au plating peeled-off part.

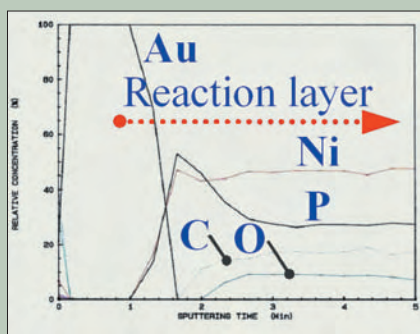


Fig. 14 Depth profile of abnormal plating (AES).

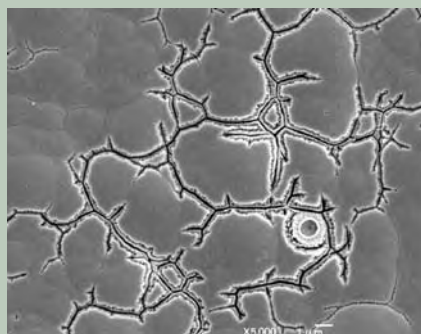


Fig. 15 Surface of abnormal plating (after removing Au).

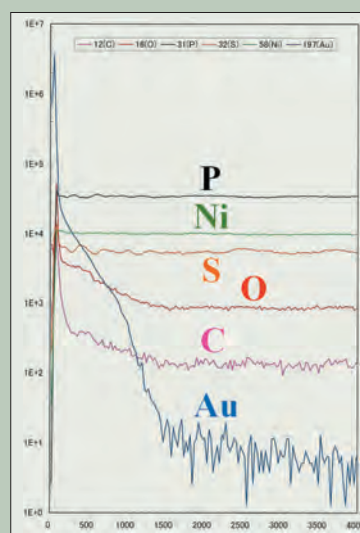


Fig. 19 Impurity concentration distribution of normal plating (SIMS).

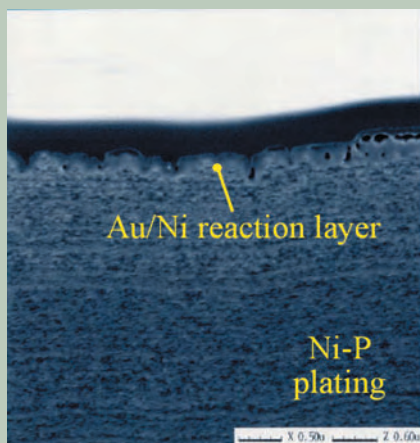


Fig. 16 Cross-sectional view of peeled-off part (FIB).

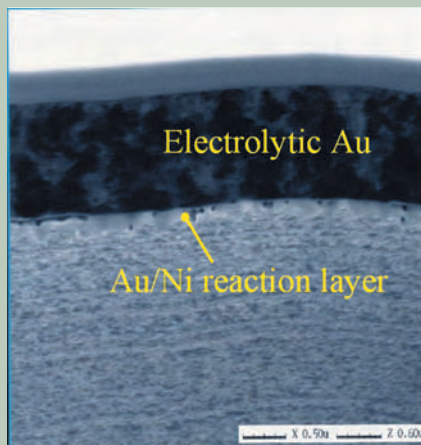


Fig. 17 Cross-sectional view of normal part (FIB).

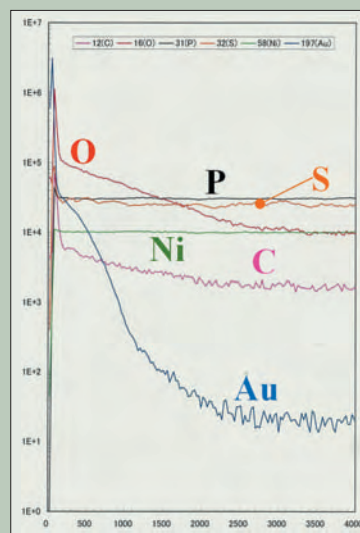


Fig. 20 Impurity concentration distribution of abnormal plating (SIMS).

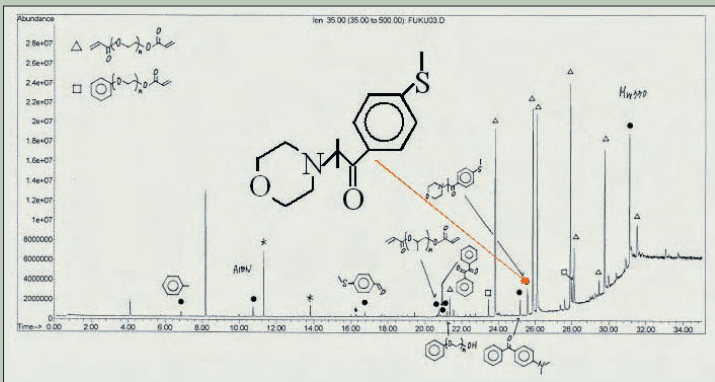


Fig. 21 Low boiling point organic component in abnormal plating solution (GC/MS).

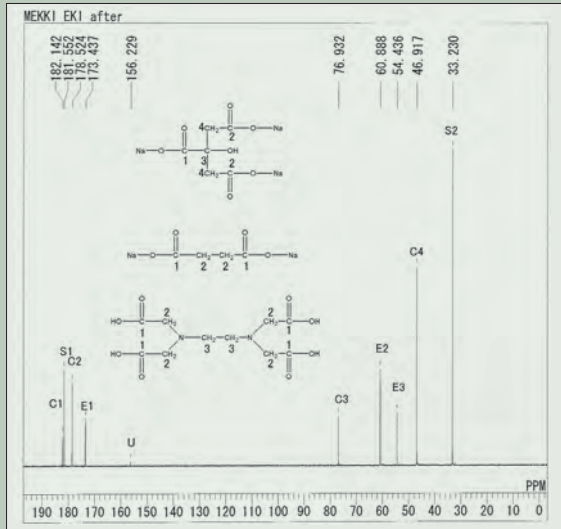


Fig. 22 High boiling point organic component in abnormal plating solution (FT-NMR).

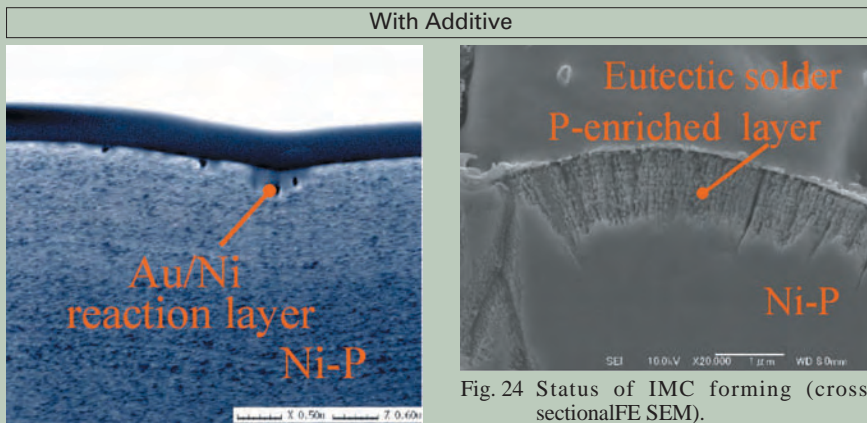


Fig. 23 Status of Au/Ni-P forming (FIB).

Fig. 24 Status of IMC forming (cross-sectional FE SEM).

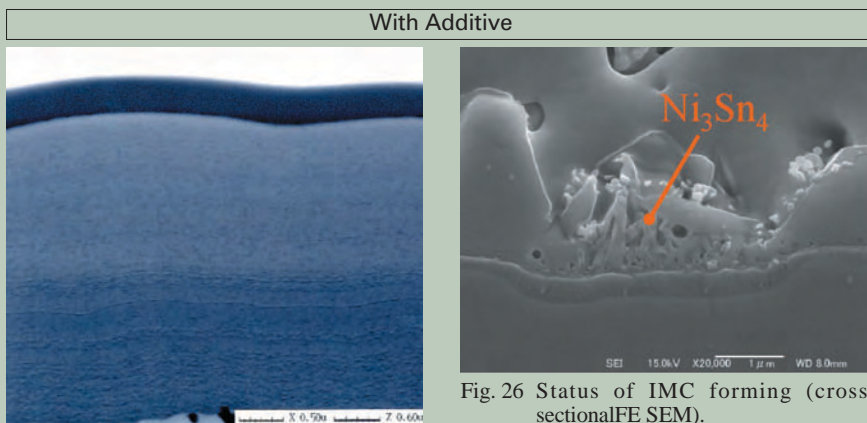


Fig. 25 Status of Au/Ni-P forming (FIB).

Fig. 26 Status of IMC forming (cross-sectional FE SEM).

brought into Ni-P solution and condensed within the bath. And it was estimated that the detected amino-alkyl-phenol, azobisisobutyronitrile and its resolvent originated from radical additive included in resin material. Actually we confirmed the status of Au/Ni-P with and without additive by FIB method and we also confirmed that the state of IMC formed at the boundary between solder and Ni-P plating after attaching the eutectic solder balls. **Figures 23 to 26** show the observed results. In case of Au/Ni-P plating with additive, an amorphous layer accompanied with voids at the surface layer of Ni-P plating was reproduced. And at the boundary between the solder and Ni-P plating, we could reproduce that no  $Ni_3Sn_4$  compounds were formed.

As described above, it was estimated that the Ni-P plating layer becomes vulnerable and the bonding power of Ni element was weakened because the organic components get mixed in Ni-P solution bath was made eutectoid. Therefore, Ni-element becomes easily to diffuse under the presence of reacting species such as Au or Sn, and it generates an excess substitution reaction in succeeding Au plating process or soldering process, but the effect of kinds of aminophenol and organic components including sulfur element is significant. The result that SIMS analysis detected highly concentrated sulfur from abnormal plating layer corresponds to this idea.

## Conclusions

We have introduced some examples relating to analysis on plating layer in packaged devices. As packaging technology advances, needs for analysis also becomes higher and more complicated. Today, analysis engineers are required not only to seek analysis technology but also to obtain an ability to give exact advices originated from empirical rules and to give so called "total solution". Essential demand in the analysis market is moving to consultation from the excellence of operation skill.

## References

- [1] ITRS2004 Update
- [2] Masateru Shibata.: Creation of cross-sectional surface specimen using an Argon beam, *Nihon Denshi News*, **Vol. 35**, No.1, pp.24-27(2003)
- [3] Tomohiro, et al.: Corrosion behavior and junction reliability of intermetallic compound phase in Au/Al junction, *J. of Japan Inst. Metals*, **vol. 63**, No.3, pp. 406-415 (1999)
- [4] Reiko Aiba, et al.: Strength of solder junction with Au plating layer formed by new non-cyan displacement type electroless plating without pitting corrosion, Digest of 19th Electronic Packaging Academic Conference on Electronic Packaging, pp. 187-188 (2005)

# Introduction of Fully Automatic NMR Measurement Tool “GORIN” for Protein Solution

## Introduction

This article explains a fully automatic NMR measurement tool “GORIN” for protein NMR. This is an optional software for the basic NMR control software “Delta V4.3” of the JNM-ECA/ECX series FT-NMR system. This software can operate only with the Delta V4.3 or later. Moreover, the HCN triple resonance probe is required in the spectrometer configuration. Since this article will describe mainly special functions, please contact the JEOL office for more details.

## Software Configuration

The following five programs are configured as the GORIN (Gorgeous Operation Routine) (Fig.1).

- MUSASHI:  
Parameter optimization tool
- OTSU:  
Continuous measurement tool
- TAQUAN DAICHOU:  
Parameter database
- IORI:  
Automatic measurement execution module
- MATA8:  
Measurement dimension transfer tool
- Others:  
Pulse programs, process lists, and templates

## MUSASHI

The parameter optimization in “MUSASHI” is mainly used to measure 90° pulse width. Accurate pulse width can be calculated from array measurement data using nonlinear least square fitting. In fully automatic measurement, this program is invoked for parameter calibration, and operated in the background (Fig. 2).

## OTSU

Continuous observation tool “OTSU” is an effective tool when measuring linearity of power amplifier output. Array measurements are performed continuously while changing the parameters such as attenuator, and this software plots the result calculated for each measurement data using MUSASHI in the graph (Fig. 3).

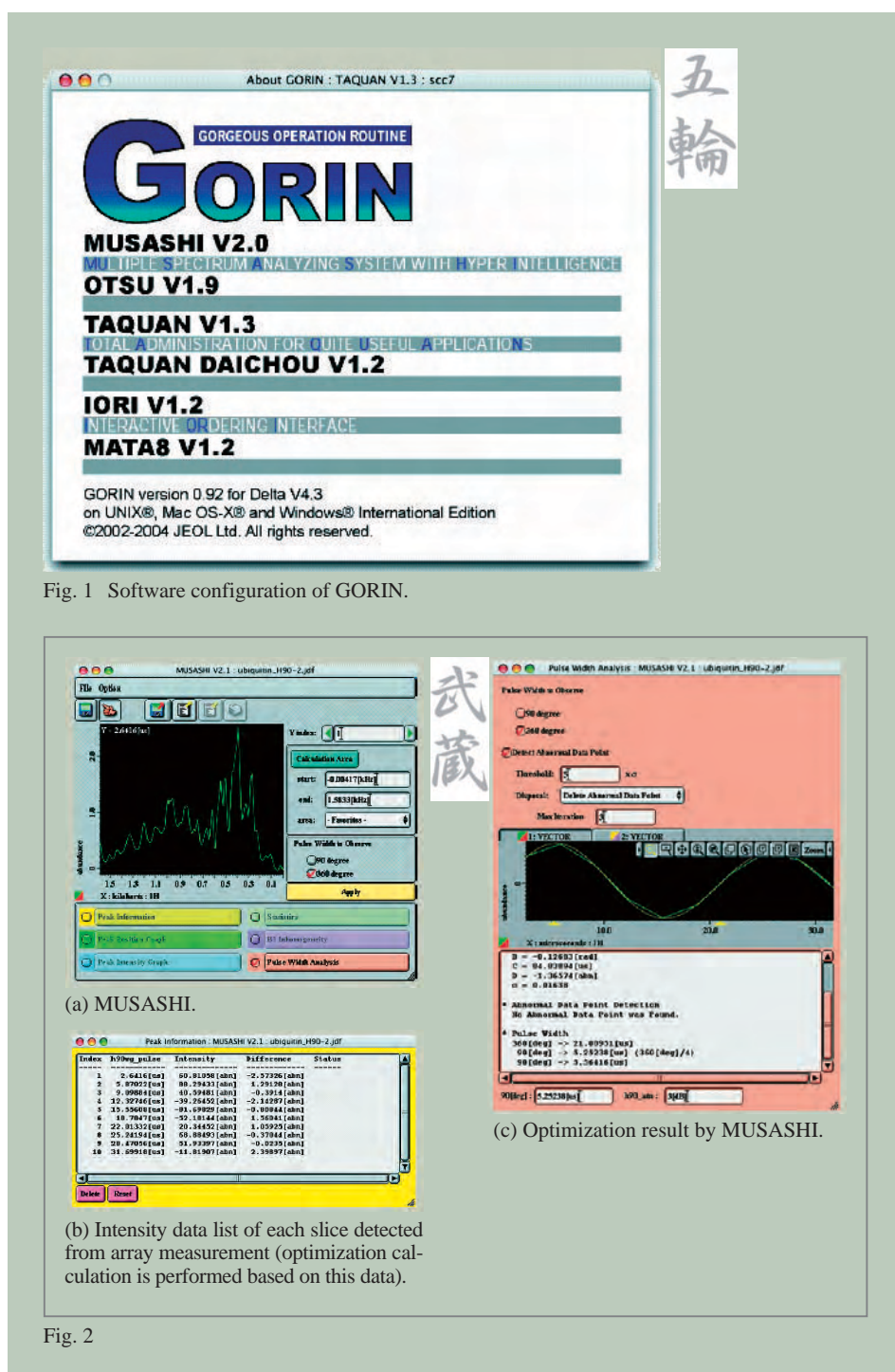


Fig. 1 Software configuration of GORIN.

Fig. 2

## TAQUAN

Automatic measurement interface "TAQUAN" (Fig. 4 (a)) is a module that performs total setting of fully automatic measurement conditions.

User can operate it by entering information on NMR sample, specifying the contents of measurement and changing parameters.

### Parameter editing

This is a window for parameter editing. NMR measurement parameters can be set. Usually, pre-selected parameter can be modified, all parameters used in the program can be changed if necessary (Fig. 4 (b)).

### Private parameter

This is a function that common parameters in every measurement such as frequency offset and observation range can be modified all together when performing two or more measurement for a sample. By this function, setting time of the parameters in every measurement can be saved, and input mistake can be minimized (Fig. 4 (c)).

### Queue editor

When running continuous measurement for two or more samples, you can check total experiment time of each measurement or the order of measurement before starting measurement, and can change the order of measurement (Fig. 4 (d)).

### E-mail Event

In TAQUAN, the spectrometer can report status or conditions to the operator by e-mail. When measurement is complete or some troubles occur in measurement, TAQUAN reports it quickly to pre-set e-mail address. By this function, you can find trouble and correspond to the problem within shorter time. Usually, since protein solution measurement may spend over a long period of time (several days), this function is implemented (Fig. 4 (e)).

## TAQUAN DAICHOU

Figure 5 (a) shows a parameter database "TAQUAN DAICHOU". It is a module, which saves and manages many kinds of parameters using automatic measurement. Information on 90° pulse widths in each channel are saved in TAQUAN DAICHOU on occasion, and applied for any kinds of measurement. TAQUAN DAICHOU detects the parameters that the instrument may be damaged such as too long pulse width based on the restriction information, and protects the instrument from damage by incorrectly-input value.

### History panel

Parameters used previously also are saved in the record. You can confirm the instrument conditions referring the record data such as pulse widths (Fig. 5 (b)).

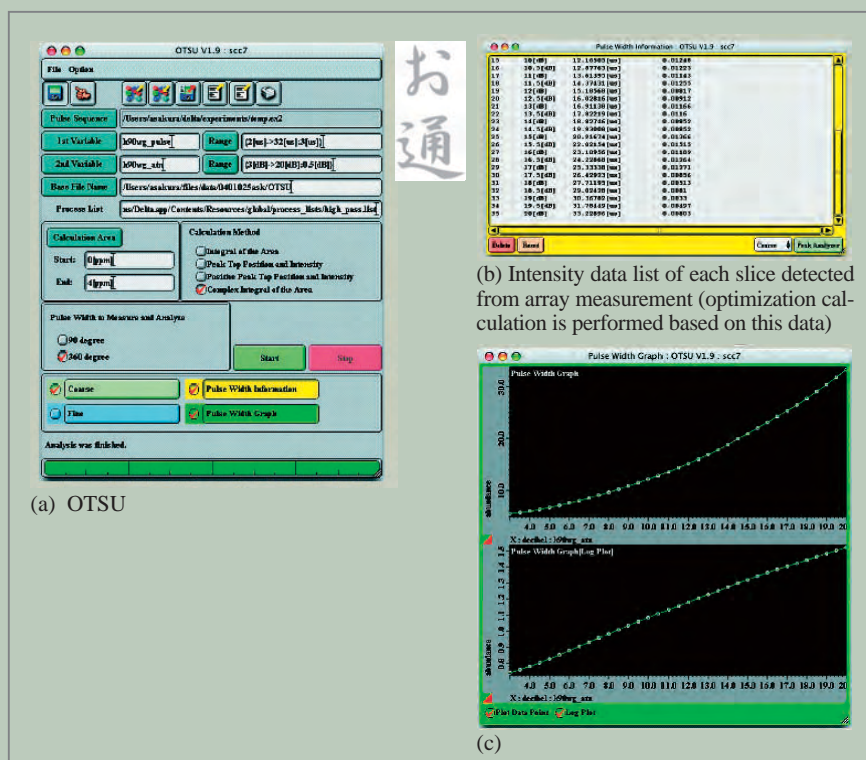


Fig. 3

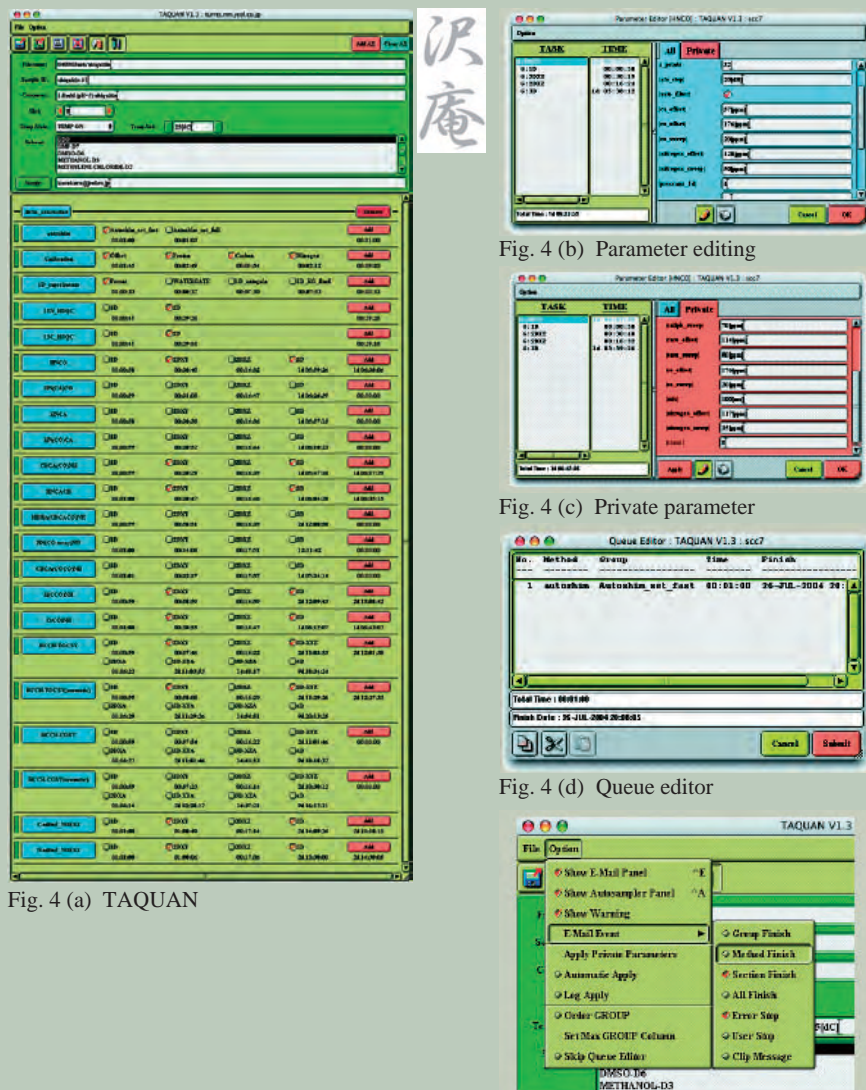


Fig. 4 (a) TAQUAN (b) Parameter editing (c) Private parameter (d) Queue editor (e) E-mail event

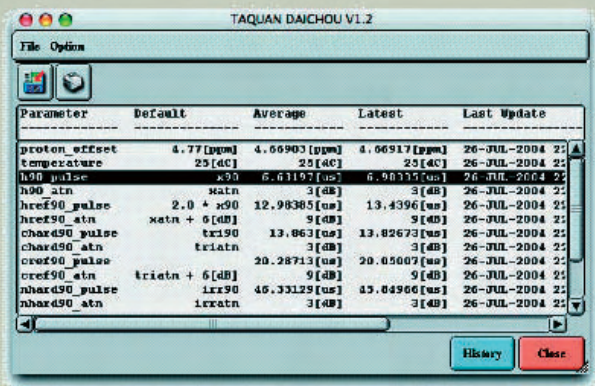


Fig. 5(a) TAQUAN DAICHOU.

沢  
庵  
帳

## IORI

Automatic measurement execution module "IORI" sends measurement conditions directly to the spectrometer. Although measurements are performed in the order of QUEUE recorded in IORI, you can also change the order of measurement here (Fig. 6).

## MATA8

This measurement dimension transfer tool mutually transfers a pulse program from 1D (1 dimension) version to higher dimension up to 4D (4 dimensions) version. This is the tool for pulse program development. To transfer measurement dimension, description of the flag for MATA8 in the pulse program is necessary. In the standard pulse program, although you can select up to 8 kinds of measurement dimension: 1D, 2DXY, 2DXA, 3DXYZ, 3DXYA, 3DXZA and 4D, the kinds of measuring dimension transformed actually differ depending on the pulse program.

## Others

### Pulse program

This is a pulse program group provided for protein solution NMR measurement. All the pulse programs are saved in "for\_protein" of global. The pulse programs for data acquisition and pulse programs for calibration are saved in the experiments and "sword\_for\_taquan", respectively. These pulse programs have been created assuming that they are used with TAQUAN.

### Process list

Corresponding process list has been provided for the data acquisition program. The process lists are saved in "protein\_lists" of global.

### Template

This is a template file for TAQUAN. Text and binary editions are provided.

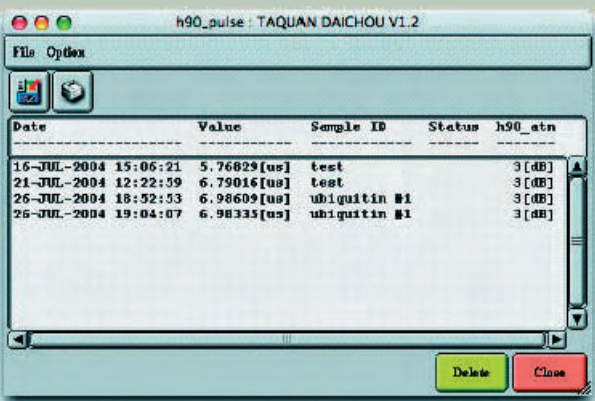


Fig. 5(b) History panel.



Fig. 6 IORI.

伊  
織

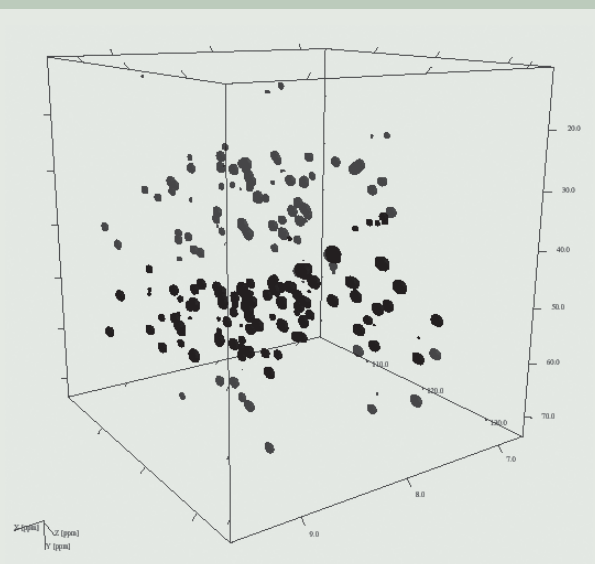


Fig. 7 Three dimension cubic display for HNCACB spectrum measured using GORIN.

## Conclusion

If you use the GORIN, an automatic NMR measurement tool for protein solution, you can obtain good spectrum similar to the spectrum obtained by professional person simply by one-button operation without complicated operation and difficult calibration. Figure 7 demonstrates a high-quality 3D NMR data obtained by the GORIN. We hope that this tool makes NMR measurement easy for protein solution and application field of protein solution NMR will be expanded.

# 100 Sample Auto Sample Changer and Tubeless NMR

## Outline of 100 Sample Auto Sample Changer, ASC100

This instrument takes out the specified sample tube (inserted a folder and rotor) from the rack, and carries it to the super conducting magnet (SCM) of the FT NMR instrument. Moreover, the instrument carries back the sample to the original position from the SCM after measurement is complete.

This instrument quickly and securely performs continuous automatic measurement for multiple samples by combining with the automatic measurement program of the NMR spectrometer.

## Features of 100 sample Auto Sample Changer ASC100

- Performs automatic measurement for up to 100 samples.
- Securely carries the sample automatically because this instrument does not directly pinch the sample glass tube.
- Random access is possible.
- Can be available for the 3 mm OD, 5 mm OD, and 10 mm OD sample tube (7 and 8 inches length).
- Sample can be set at the front table of the magnet.
- A vibration-free table is not required.
- Operation can be done by off-line or on-line.

## Specifications

- Number of samples: Up to 100
- Out diameter of sample tube: 3 mm, 5 mm, 10 mm
- Sample tube length:
  - 178 to 203 mm (not include cap)
  - 7 or 8 inches + cap (10 mm or less)

For example: WILMAD 8 inches sample tube:  
8 inches (203 mm) + cap (10 mm) = 213 mm

## System configuration of ASC100

- Auto sample changer ASC100 : 1 set
- PC (computer) : 1 set
- Holder/rotor : 100 (3 mm OD, 5 mm OD,

- 10 mm OD)
- Air compressor : 1 set

## Configuration and functions of ASC100

**Figure 1** is a schematic diagram of the ASC100. The ASC100 takes out the specified sample from the rack, carries it to the super conducting magnet (SCM) and carries back the sample to the original position from the SCM. The ASC100 consists of the basic unit and the transportation unit.

Since the basic unit and the transportation unit are separated mechanically, the floor vibration is not transmitted through the basic unit installed on the floor.

The sample rack of 10×10 positions is provided in the basic unit, and the samples are set on the sample rack before measurement. The sample rack is placed on the XY stage, and can be moved to the X and Y direction. After a measurement target sample moves to just under the cylinder for perpendicular movement of the sample tube transportation unit by moving the sample rack, the sample is inserted into the cylinder of the transportation unit by the Z axis actuator. The transportation unit lifts up the sample inserted in the cylinder by a lifter, and move it center position on the SCM by moving to the horizontal direction. After that, the sample tube is inserted into the SCM similar to usual measurement.

After measurement is complete, the sample tube is carried back to the original position on

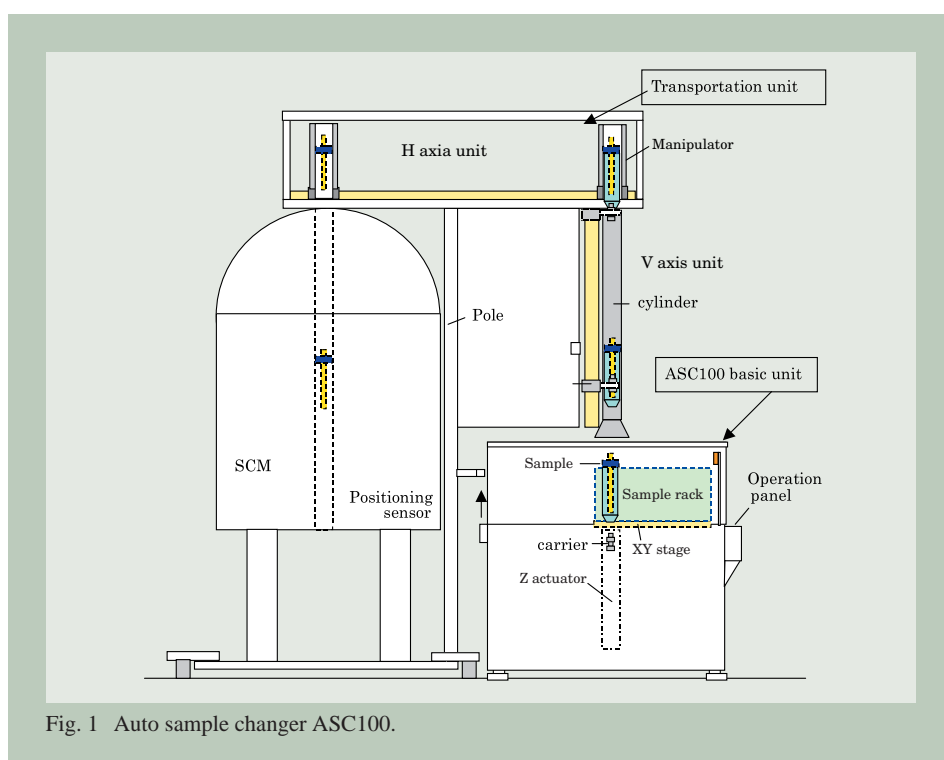


Fig. 1 Auto sample changer ASC100.

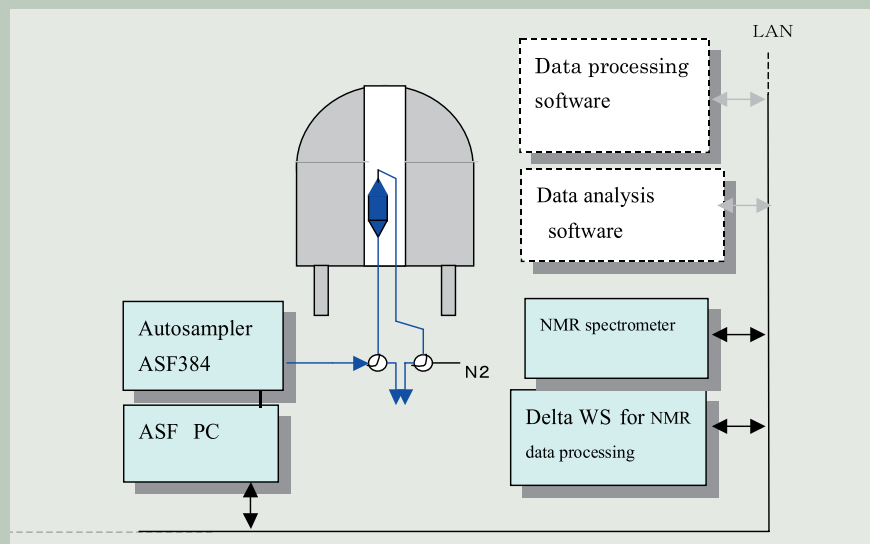


Fig. 2 Flow NMR Autosampler ASF384 connection.



Fig. 3 Configuration of Flow NMR Autosampler ASF384.

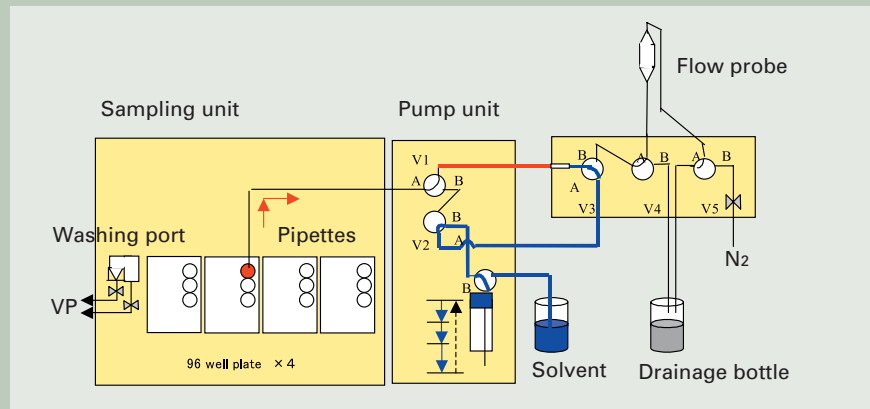


Fig. 4 Block diagram of process of sending solution in Flow NMR Autosampler.

the sample rack.

## Flow NMR Autosampler ASF384

The high throughput automatic measurement is required to process a large number of NMR samples.

This liquid handling robot type sample changer ASF384 performs NMR measurements for up to 384 samples.

This instrument transfers a sample with an ID number from each well to a flow cell probe.

The run-time rinsing the flow path during accumulation enables the measurement of carryover-free NMR spectra.

### Features of flow NMR autosampler ASF384

- Up to 384 samples can be prepared automatically.
- Information on sample ID can be sent automatically.
- High throughput NMR measurement can be done automatically.
- The pipette, cell of the probe and tubing can

be washed automatically.

- A measurement is easily booked or removed. (Visual operation by clicking on the well)
- Record and deletion for measurement can be easily changed. (It can be performed just before measurement.)
- Measurement conditions can be easily confirmed. (The well is displayed with color for unrecorded/record/measured)
- The progress of the well measurement is easily confirmed. (Display for plate No., Well Pos., and Serial No.)

### Main specifications

- Sampling set
  - Sample plate: 96 wells micro-plate × 4 (96 × 4 = 384)
  - Sampling: X direction: moving pipette arm, Y direction: moving tray, Z direction: moving pipette
  - Solvent: One kind
- Software
  - Operation function: Sample selection, start, stop, initialize, purging, and Manual operation
  - Setting: Parameter setting
  - Communication: TCP/IP network connection (between this unit PC and NMR system)

Performs communication of measurement start and stop, and sends sample ID information to the NMR system.

### ASF384 system configuration

- 1) Flow NMR Autosampler
 

ASF384 basic unit	1 set
Sampling unit	1
Pump unit:	1
Valve unit	1
Reagent bottle	1 set
- 2) PC (computer) 1 set
  - Software (Windows based)
- 3) Vacuum pump 1
- 4) Vacuum trap bottle 1 set

### Configuration of Flow NMR Autosampler ASF384 and function

The control PC for ASF384 is connected to LAN so that the NMR spectrometer and its data system are connected, and controlled by processing program of the spectrometer (Figs. 2).

The Flow NMR Autosampler ASF384 consists of the sampling unit, pump unit and valve unit. This AFS384 sends a sample on the micro-plate to the probe by controlling the valve and pump, and exhausts the sample from the flow probe (Figs. 3).

The sampling unit moves the pipette arm (X direction), tray (Y direction) and pipette (Z direction), and automatically performs sampling one by one by sucking the sample from each well of four 96 wells micro-plates placed on the tray according to the sampling order by the pipette.

The pump unit consists of the syringe pump; two-ways switch valves (2), and nitrogen pressure gauge. The syringe sucks a sample and sends it to the probe, and washes the pipette and flow probe by sending solvent.

The valve unit consists of three two-ways switch valves. These valves switch a flow route according to the purpose such as sending sample to the probe, and exhausting a sample from the probe (Fig. 4).

# Latest Information and Future for ALICE2 Software

## -Application for metabonomics-

### Introduction

Recently, the metabolome analysis or metabonomics, which covers all metabolites, is given attention along with progressing genome and proteome science. Generally, the metabolome analysis using NMR uses a proton spectrum. However, since a biological sample includes many low molecular weight substances and biological polymers, the proton spectrum is very complicated by many overlapping peaks. Moreover, since there are many

small signals in the spectrum, it is difficult to distinguish them from noise. So assigning each peak as ordinary analysis method cannot perform structure analysis. Therefore, pattern recognition approach is applied to the classification of the spectra for these samples by measuring many samples and performing statistical analysis. Metabolic difference and time-lapse change can be detected by this method. So far, however, there was not the simple software with this metabolome analysis.

This time, since we develop ALICE2 for metabolome that full automatic metabolome analysis function is added to the ALICE2 of NMR processing software, we will introduce it in this article.

We will explain the outline of the developed program first, and explain results of the inspection experiment of this program using mixture samples. However, since handling of a biological sample is difficult, we try to analyze the proton spectra of various kinds of tea as an example of the analysis of mixture sample.

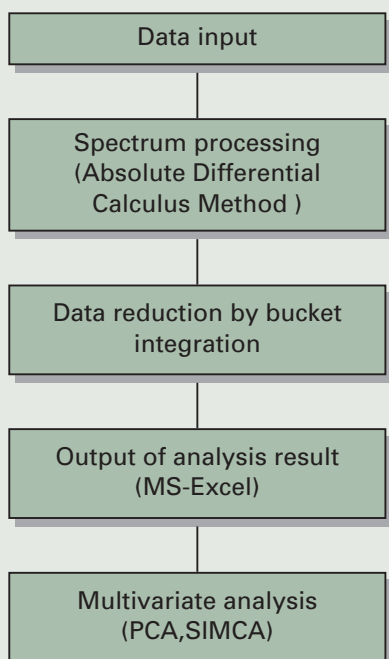


Fig. 1 Process of metabolome analysis.

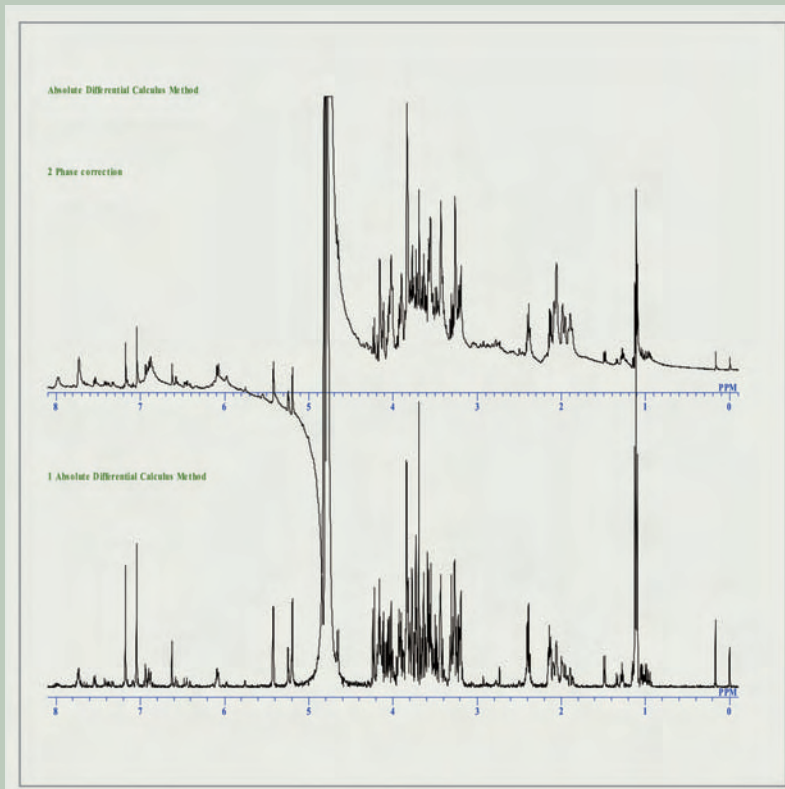


Fig. 2 Phase corrected spectrum (upper), and Absolute differential spectrum (lower).

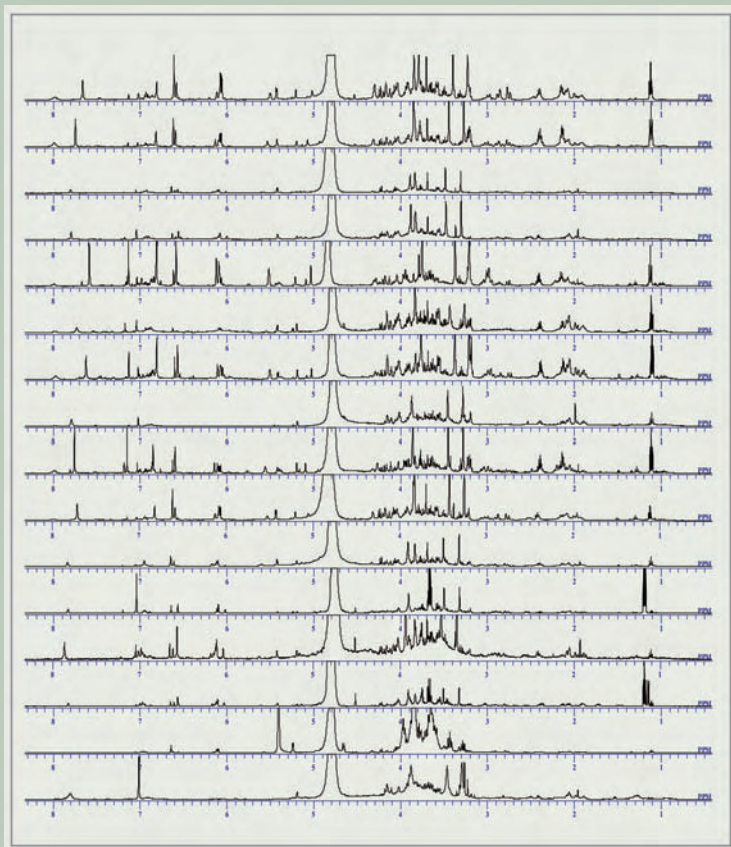


Fig. 3 In the lump display for many spectra of many samples by Multi-spectra function.

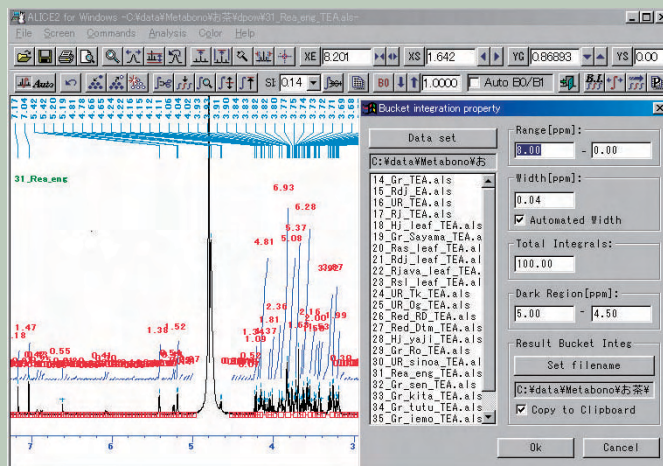


Fig. 4 Setting bucket integration conditions and executed result.

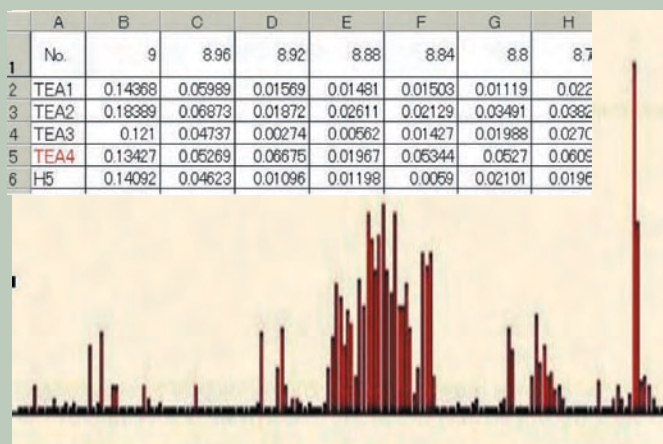


Fig. 5 Bucket integration analysis result pasted on the MS-EXCEL sheet and graph of output result.

At first, we want to say that this software can be applied to not only biological sample, but also any other mixture such as food and polymer.

## Outline of Program

The process of spectrum analysis for a sample mixed multiple substances such as metabolome analysis is shown in Fig. 1. To obtain the statistical reliable data set, the subjects of this program development are high-throughput analysis for many samples, and data reduction of the complicated spectrum to input in multivariate analysis. Purpose of this program is to obtain the optimum analysis result in a short time by full automation process.

## Spectrum processing (Absolute Differential Calculus Method)

In this development, an accuracy of the phase and baseline correction of the spectrum is important subjects. If the phase and baseline correction is performed using ordinary method, many hours are required. Moreover, some factors depending on an operator may influence the corrected phase and baseline due

to performing manually.

To solve this problem, at this time, the Absolute Differential Calculus Method is developed for spectrum analysis. A good quality spectrum can be simply obtained using this method without phase and baseline correction. Moreover, the minimization effect for an influence of a very large water peak was verified (Fig. 2). Demerit of this method is to lose quantitative character between peaks. Especially, the signal intensity of a broad peak decreases extremely.

However, since relative relationship between spectra is kept, this method is effective for analysis of many spectra in this investigation purpose. Moreover, after processing many spectra in the lump, you can verify the processing result using Multi-spectra function, and create data set (Fig.3). You can also correct the data before creating data set if necessary.

## Data reduction by bucket integration and analysis result output

Next step is data reduction by bucket integration, and the analysis result output.

In order to transfer the measurement spec-

trum to multivariate analysis, the bucket integration is performed, which integrates the spectrum divided with specified width, and converts the spectrum into the variable of about 200. These functions can be performed in the exclusive dialog box after specifying a data set, and entering conditions of integration range, width, total values and unnecessary integration range around the water peak. (Fig. 4)

The output format of analysis result is text format of scores. (Fig. 5)

Data processing from data input to analysis result output (MS-EXCEL) is fully automated by combining the Absolute Differential Calculus Method and Bucket integration, and data processing for the multiple samples can provide high throughput.

## Inspection Experiment of ALICE2 for Metabolome

The  $^1\text{H}$  spectra are analyzed as a sample of mixture.

## Sample preparation and measurement for 100 teas

Green tea (Uji Gyokuro, Sayama Sencha,

Yamanashi Hojicha, Chinese green tea) black tea (Darjeering, Assam, Chinese black tea), oolong (Tekkanon, Okinnkei ) are extracted with hot water for 3 minutes at 75°C, and the top is used after centrifuging.

Measurement condition: Deuterated water is added 10 %, and water signal is eliminated using the pre-saturation method.

Instrument: JNM-ECA500 (Proton resonance frequency is 500 MHz.)

Typical spectra of teas are shown in **Fig. 6**. In the spectra, typical peaks of catechin, theanine, caffeine and many amino acids appear. The peak of amino acid cannot be assigned because many amino acids are included. Spectrum pattern of green tea differs from spectrum of black and oolong tea, and peaks of catechin and caffeine are shifted.

### ALICE2 for metabolome processing and multivariate data analysis

The spectra of 100 kinds of teas are processed using the ALICE2 for Metabolome, the MS-EXCEL file is obtained. At that time, the bucket integration width is 0.04 mm, and nearby water signal (4.8 to 5.1 ppm) is eliminated as the unnecessary analysis region. Total bucket integration values from 1 to 10 ppm is set to 100 in order to normalize the integration values between spectra. The multivariate data analysis is preformed using the Strius™ (PRS, Norway) software.

### Principle Component Analysis

By processing ALICE2 for Metabolome, a spectrum is transformed to a characteristics item that consists of variables including about 200 integrations. It is called PCA scores plot that the spectra are arranged along with the largest distribution of the principle component (axis) of 100 characteristics items so that characteristic of 100 spectra can be distinguished clearly. **Fig. 7** is plotted using two axes (principle component). One point shows one spectrum.

In Fig. 7, the typical teas are almost separated into independent groups. The characteristics item at this time can be explained over 70 % by using principle components of the first and second. What is the extracted characteristics item? Although all kinds of tea are made of same kind of tealeaf, green tea and black tea have difference in the fermentation level. Green tee is no fermentation. Black tea is fermented completely. Oolong tea is called semi-fermentation tea, and there are oolong teas of various fermentation levels.

Since oxidation of hojicha is progressed by heating, it may be classified into similar group to fermentation tea. Thus, the fermentation level is extracted as characteristics item, and various kinds of tea can be classified into the specified groups.

### Conclusion

As shown in investigation for 100 teas, quantity of the chemical compositions of tea, such as amino acid, catechin, etc., is different depending on the fermentation level.

Although difference of chemical composition is reflected in the spectrum pattern, impor-

tant characteristics of tea (it is assumed fermentation) can be extracted from the spectra using the statistics method of ALICE2 for Metabolome without assignment of each peak. Moreover, although the analysis method for the variable (peaks of spectrum) that characterized a spectrum also exists, it is omitted here. In statistics analysis, very important factor is a

number of samples. Furthermore, if the samples are increased, more new information may be obtained.

Although it is shown above that ALICE2 for Metabolome is effective in analysis of tea, this program can be applied for analysis of the complicated mixture sample system, such as the food and biological samples.

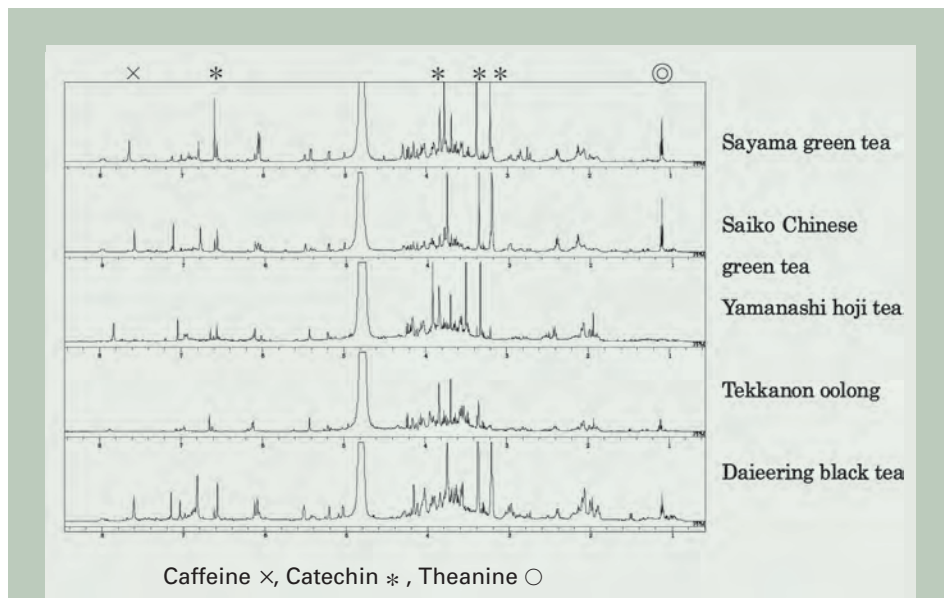


Fig. 6 <sup>1</sup>H spectra of typical teas.

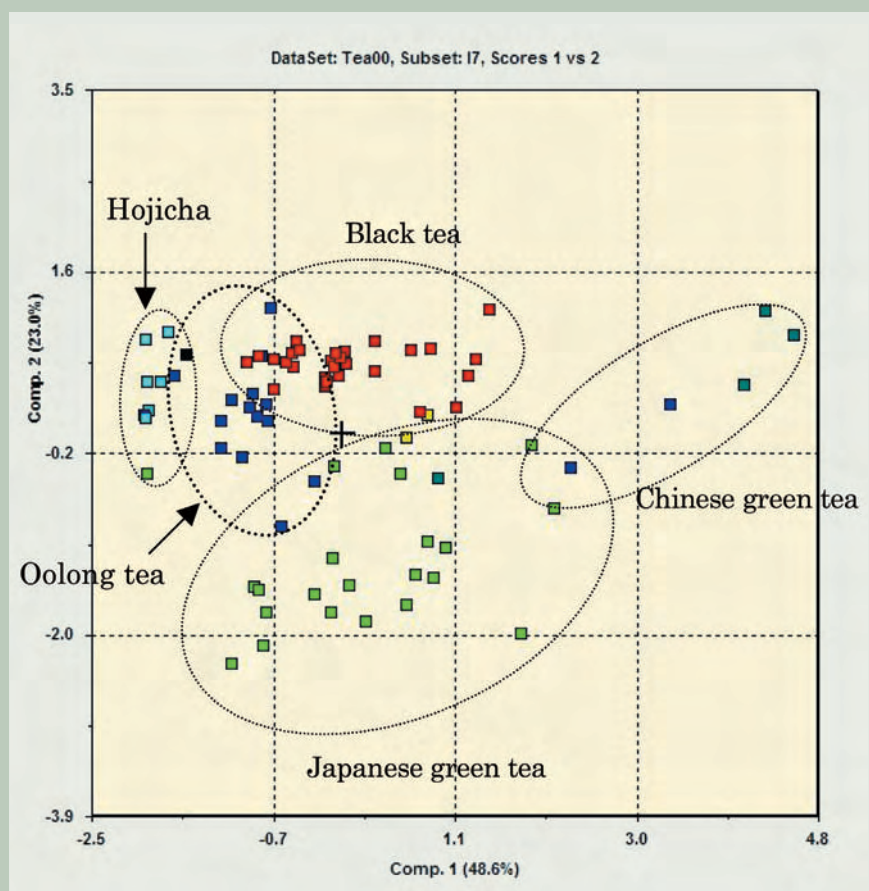


Fig. 7 PCA plot.

# Windows Delta

## Introduction

JEOL has supplied the Delta software in the various platform.

For example, IRIX Delta operated on the Silicon Graphics workstation for the JNM-ECP series FT NMR system, AIX Delta operated on the IBM RS/6000 workstation, and Linux Delta operated on the HP Linux workstation for the JNM-ECA/ECX series FT NMR system have been supplied. This time, Windows Delta operated on the Windows XP® for the JNM-ECA/ECX series FT NMR system will be supplied. This article briefly explains the contents of the software.

## Specifications

### Specifications of hardware

This is the same configuration as the current Linux workstation (NM-57032PCW)

- Processor : Intel Xeon 3.06 GHz × 1
- Memory : 1GB (512 MB× 2)  
ECC registered DDR266 SDRAM
- Hard disk : 73 GB 10 Krpm Ultra 320SCSI
- Graphic adapter (PCI) : NVIDIA Quadro4 980XGL
- Floppy drive : 3.5 inch
- CD-ROM drive : 48 × ATAPI
- Zip drive : zip750ATAPI
- Key board : USA layout
- Mouse : 3 button
- Network : 10Base-T, 100Base-T/TX, 1000Base-T
- 19 inch TFT Liquid crystal monitor 1280 × 1028 pixel

Note: specification of the hardware may be changed without notification.

### Specification of software

#### OS

- Windows XP Professional + Service Pack 1

#### Delta software version

- V 4. 3. 2

#### Function

The functions and features of the NMR software are the same as AIX or Linux:

1. NMR spectrometer control
2. Pulse sequence and measurement
3. NMR data processing
4. NMR data analysis
5. 2D CFR prt11
6. GLP
7. Help and on-line manual

### Restriction items

- Printer  
Delta V4,3,2 performs print out with Postscript. So the printer applied Postscript Level2 is required.
- Restriction by Windows  
Cut & Past of screen cannot be supported.
- Coexistence with other software  
Operation of the Delta software cannot be guaranteed in coexistence with other software

on one computer. It is out of support.

Notes: The software guaranteed operation in coexistence with the Delta software is the following software:

1. Adobe® Reader® 6.0
2. Adobe® Acrobat® 6.0

## Supplying Windows Delta

- Supply style  
The software can be supplied only with workstation.
- Supply start  
From spring in 2005.
- Price  
Please contact the JEOL office for price.

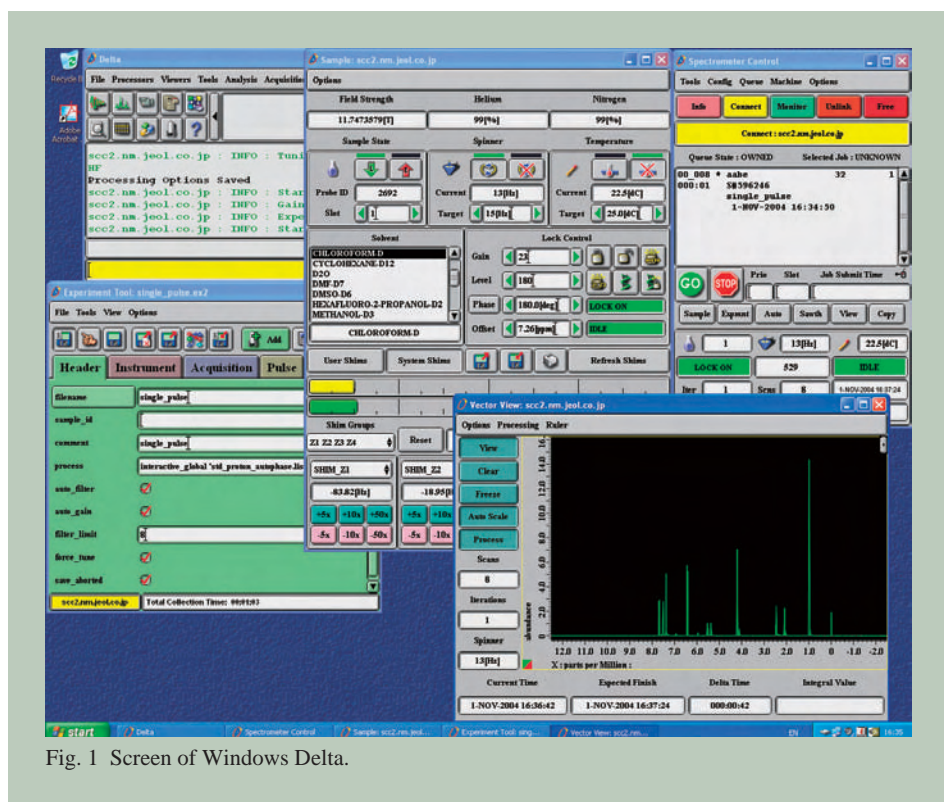


Fig. 1 Screen of Windows Delta.

# Features and Applications of Newly-Developed GC-TOFMS “The AccuTOF GC”

Masaaki Ubukata

Analytical Instrument Division, JEOL Ltd.

## Introduction

A gas-chromatograph mass spectrometer (GC-MS) is a combined analyzer that has superior ability in analyzing organic compounds qualitatively and quantitatively. The first part, gas chromatograph, separates the compounds included in a sample (mixture), then the second part, mass spectrometer, obtains mass spectra of the compounds to carry out qualitative analysis. Quantitative analysis can be carried out as well from the peak area of the mass chromatogram of the compound.

As a mass spectrometer of a GC-MS system, several types of mass spectrometers are on the market, such as magnetic field, quadrupole (QMS), ion trap (ITD), and time-of-flight (TOF). Each mass spectrometer has its own features and applications.

By the way, “fast GC”, one of the GC methods, has become to attract attention recently. The fast GC method can shorten the analysis time remarkably while keeping a good separation ability equal to the conventional GC methods, by using a narrow and short column of about 0.1 mm inside diameter and 10 m long. The fast GC method, adopted in a GC-MS system, has the ability to improve the system throughput. However, it requires a fast spectrum-acquisition speed to the mass spectrometer, because the chromatograph peaks are narrower in time than a conventional GC. TOFMS only has the ability to satisfy the demand for fast spectrum-acquisition speed at the present time, but the existing GC-TOFMS systems are not satisfactory by either of the following reasons: it can follow the fast speed of the fast GC, but its mass resolution is too low to measure accurate mass, or, on the inverse, it has a mass resolution high enough to measure accurate masses but cannot follow the fast speed of the fast GC.

JEOL has developed and announced an innovative GC-TOFMS instrument, JMS-T100GC “The AccuTOF GC” in September of 2004, which satisfies both demands for high speed responding to the fast GC method, and for obtaining accurate mass easily.

The AccuTOF GC inherits the features of high resolution, accurate mass measurement with simple operation, and high sensitivity from its sister instrument, JMS-T100LC “The

AccuTOF.” The AccuTOF series contains a continuous averager in the data acquisition system that offers a wider dynamic range when compared to the time-to-digital converter (TDC) used in a conventional GC-TOFMS. In addition to this, the AccuTOF GC supports the fast GC/MS measurement, and is the first instrument that realizes these features in one instrument, which was impossible for the conventional instruments.

We have reported the principal features and the basic performances of the AccuTOF GC in the preceding 2003 MS Users Meeting. Here, we discuss the applications of the AccuTOF GC, in addition to the features and the basic performances.

## Overview

### Basic configuration

The basic configuration of the AccuTOF GC is as follows:

- TOFMS main unit  
(EI ion source is the standard)
- GC (Agilent 6890N)
- Personal computer
- Printer

Options include:

- Direct Injection Probe  
(Direct Exposure Probe (DEP))
- GC Automatic Sampler  
(injector + 100 sample trays)
- CI Ion Source
- FD/FI Ion Source
- EZChrom  
(software for quantitative analysis)

A plug-and-socket ion chamber is provided for both the standard EI ion source and the optional CI ion source, which allows cleaning of the easily contaminated ion chamber only, and makes replacing the filament easy.

An isolation valve is provided between the ion transfer system and the analyzer. Closing it keeps the analyzer in a high vacuum even during the following occasions: replacing the column and maintenance of the ion source, when a large quantity of solvent flows from the GC during measurement, and in emergency such as power failure.

The direct injection probe is a DEP type; the sample is initially dissolved in a solvent,

and is applied to the platinum filament of the probe using a syringe.

### External view

Figure 1 shows the external view of the AccuTOF GC. The AccuTOF GC is an on-floor type and has casters at the bottom to facilitate transport of the system.

(Note: In order to prevent damage to the turbomolecular pump, the system cannot be moved while in operation.)

The AccuTOF GC has integrated a turbomolecular pump and a rotary pump into the main unit, resulting in an effective footprint equal to or smaller than a typical bench-top system.

## Features of the Instrument

Figure 2 shows the diagram of the AccuTOF GC. It comprises depending on the functions:

- Ion source and ion transfer system
- Analyzer
- Detector
- Data acquisition system
- Data system (personal computer)

### Ion source and ion transfer system

Figure 3 shows a plan-view sectioned diagram of the ion source and ion transfer system. The role of this system is to ionize the sample introduced from the GC, and to transfer the ions to the analyzer at a low kinetic energy of about 30 eV.

The plug-and-socket ion chamber, shown at the top left of Fig. 3, has two gas inlets. One at the upper right in the photo is the gas inlet from the GC, and another one at the lower right is the gas inlet from the sample-heating device for the standard sample and others. The plug-in structure facilitates easy maintenance.

In a GC-MS system, a large quantity of helium gas, used as the GC carrier gas, is introduced to the ion source. The helium gas is ionized and transferred to the analyzer together with the sample. The helium gas, because of its overwhelming volume, causes a serious space-charge effect including charging-up of the surrounding parts. Because the AccuTOF GC is an orthogonal accelerating time-of-flight mass spectrometer (oa-TOF MS), the ions



Fig. 1 External view of the AccuTOF GC (Includes an optional automatic sampler).

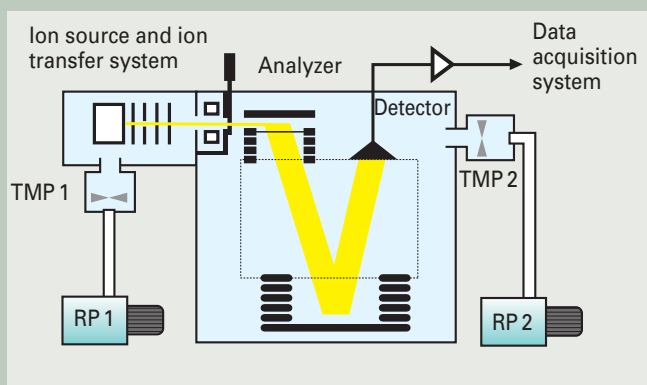


Fig. 2 Diagram of the AccuTOF GC.

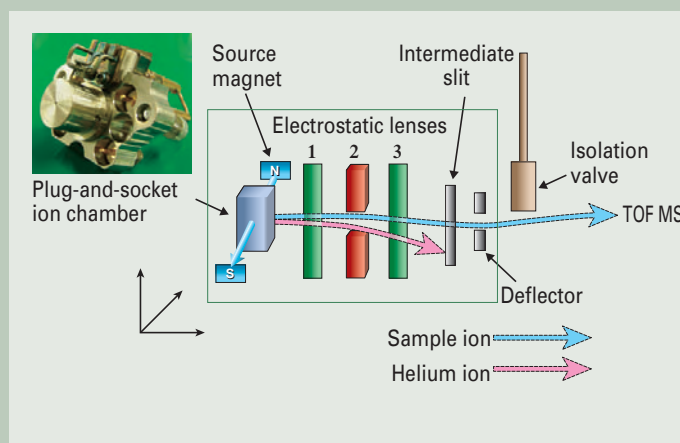


Fig. 3 Ion transfer system diagram.

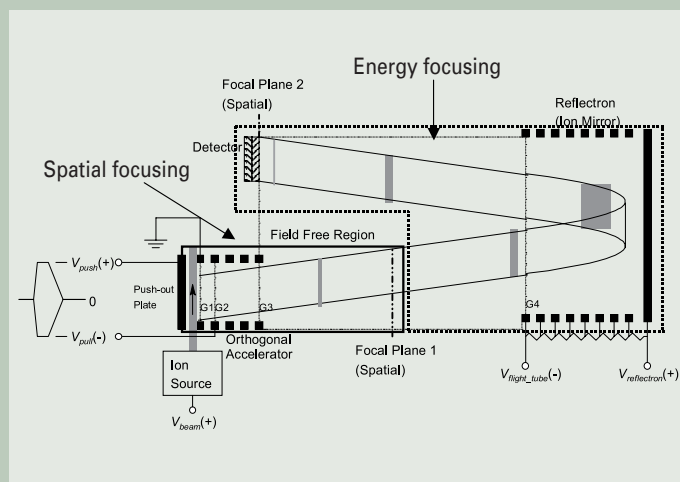


Fig. 4 Analyzer diagram.

must be transferred at a low kinetic energy of about 30 eV to the analyzer. Therefore, the ions are highly susceptible to the space-charge effect. Moreover, as all the ions, including helium ions, introduced to the analyzer reach the detector, the large quantity of helium ions might lead to a failure of the detector. To avoid the problem, the AccuTOF GC specifically developed an ion-transfer system that can remove more than 99% of helium ions before the ions enter the analyzer. The ion transfer system has the following three structural features:

- The electrostatic lens 2 is separated into two parts.
- An intermediate slit is installed.
- A deflector behind the intermediate slit.

In the EI ion source, a source magnet is placed to prevent dispersion of the electron beam emitted from the filament. By arranging the source magnet in a horizontal plane, an ionized ion accepts a force so that it is deflected downward, in case of a positive ion, while moving toward the analyzer. The extent of deflection differs according to the mass; the smaller the mass-to-charge ratio, the larger the deflection. The AccuTOF GC, making use of this mass selection ability of the source magnet, succeeded in colliding the helium ions with the plate of the intermediate slit and remove them, by optimizing the balance of the voltages of the upper and lower parts of the

electrostatic lens 2. The intermediate slit also assists the differential evacuation between the ion source and the analyzer. The ions passed through the intermediate slit are introduced to the analyzer with good efficiency due to the optimized deflector voltage.

In addition, the AccuTOF GC incorporates an isolation valve that isolates the ion transfer system from the analyzer. The isolation valve makes it possible to vent the ion source and carry out maintenance of it without venting the analyzer. Furthermore, it isolates the analyzer automatically in an emergency such as an unexpected stop of the evacuation system, which prevents the detector from degrading.

### Analyzer

The analyzer of the AccuTOF GC is an orthogonal accelerating time-of-flight mass spectrometer (oa-TOF MS) incorporating two-stage acceleration and a single-stage reflectron. It achieves high resolution owing to the spatial focusing by the two-stage acceleration and the energy focusing by the single-stage reflectron.

The diagram of analyzer of the AccuTOF GC is shown in Fig. 4. The sample is ionized in the ion source continuously, arranged in a parallel ion beam, and introduced to the space between the push-out plate and the grid 1 (G 1) in the orthogonal accelerator. To accelerate ions to the orthogonal direction, pulse volt-

ages,  $V_{push}$  and  $V_{pull}$ , are applied at the push-out plate and the grid 2 (G 2) respectively. A negative high voltage,  $V_{flight-tube}$ , is applied at the grid 3 (G 3) and the shield surrounding the field free region all the time, in case of analyzing positive ions. A positive voltage,  $V_{reflectron}$ , is always applied at the end of the reflectron.

### Detector

As we will see in the section “Data acquisition system,” when a time-to-digital converter (TDC) is used as the data acquisition system, the quality of a mass spectrum is hardly affected by the characteristics of the data acquisition system. But the TDC system is difficult to handle because it requires statistical correction of the acquired signal, and the mass accuracy depends on the accuracy of the parameter for the statistical correction. On the other hand, when a high-speed analog-to-digital converter (ADC) in combination with a continuous averager is used as the data acquisition system, the quality of a mass spectrum, such as mass resolution and peak shape, is directly affected by the characteristics of the data acquisition system, but this system has a merit that it does not require the statistical correction essentially. The AccuTOF GC adopts the ADC-with-continuous averager method, and a device to minimize the signal distortion

is installed.

The detector is mainly comprised of a micro channel plate (MCP) and an anode. The MCP is a glass plate approximately 0.6 mm thick having channels, that are honeycomb holes with an inside diameter of 10  $\mu\text{m}$  at intervals of 12  $\mu\text{m}$  (between channel centers). Both surfaces of the MCP are metal coated, serving as electrodes. A voltage applied between the electrodes will produce an electric-field gradient inside the channel.

When an electron hits the inner wall of the channel near the entrance, multiple secondary electrons will be emitted. These electrons will be accelerated by the electric-field gradient inside the channel, hitting the wall on the opposite side and emitting secondary electrons again. Thus, the electrons advance to the exit while hitting the inner wall of the channel repeatedly, resulting in a flow of electrons exponentially multiplied.

The electrons will be captured by the anode to produce an electrical signal. The amplification factor of the MCP (the number of electrons emitted from the exit when one ion is introduced to the entrance) is several thousands at maximum. Since TOF MS requires a detector having an amplification factor of  $10^6$ , it usually uses two MCPs layered (dual MCP).

## Data acquisition system

The data acquisition system digitizes electrical signals from the detector, arranges them into a format compatible with the data system,

and transfers them to the data system. The data acquisition system of an oa-TOF MS system must meet the following severe requirements.

### Acquiring data with extremely high time resolution

When the AccuTOF GC achieves a mass resolution of 5,000 (FWHM; full width at half maximum) with the molecular ion of octafluoronaphthalene ( $m/z$  272), the time of FWHM of the peak is 3 ns. To specify the peak position (= flight time = mass) as accurately as possible, it is said that at least 10 data points are necessary in the FWHM. Accordingly a time resolution of 300 ps is required for the data acquisition system of the AccuTOF GC.

### Acquiring data continuously

The system needs to begin acquiring data for the next ion flight as soon as one ion flight is completed. If there is a time lag between flights, the ion utilization ratio will decline because the ions that have passed through between the push-out plate and the grid 1 are wasted and not detected, resulting in poor sensitivity.

### Accumulating spectra in real time

The flight times of any ions will be shorter than 200 ms. When the  $m/z$  range to measure is less than 1,000, the flight time of ions will

be shorter than 55 ms. Therefore, when ion flights are repeated with this time intervals, ion flights of approximately 18,000 times per a second are counted. However, it is meaningless to try to get each flight data as an independent spectrum due to the following two reasons: First, each flight data is poor in S/N to be analyzed because the number of ions generated in the ion chamber in 1/18,000 second is small. Second, saving data of 18,000 spectra per second on a hard disk is utterly impractical in terms of data transfer speed and data capacity. Therefore, the data acquisition system acquires and accumulates multiple spectra for a specified period of time and forwards the accumulated data to the data system.

Two types of data acquisition systems meet these basic requirements, TDC and the ADC-with-continuous averager.

TDC (time-to-digital converter) is a kind of high-speed and high-accuracy stopwatch. It judges if any pulse of ions having a height exceeding a certain threshold level is detected or not in a specified measurement interval, resulting data of 1 (detected) or 0 (not detected). Even if multiple pulses are detected in one measurement interval, the later pulses are not counted, resulting in data of 1 (dead time loss). Thus, the TDC method requires a statistical correction, resulting in a low dynamic range as low as  $10^3$ , which is one of the demerits.

On the other hand, the ADC-with-continuous averager converts a signal from the amplifier with its high speed 8-bit analog-to-digital

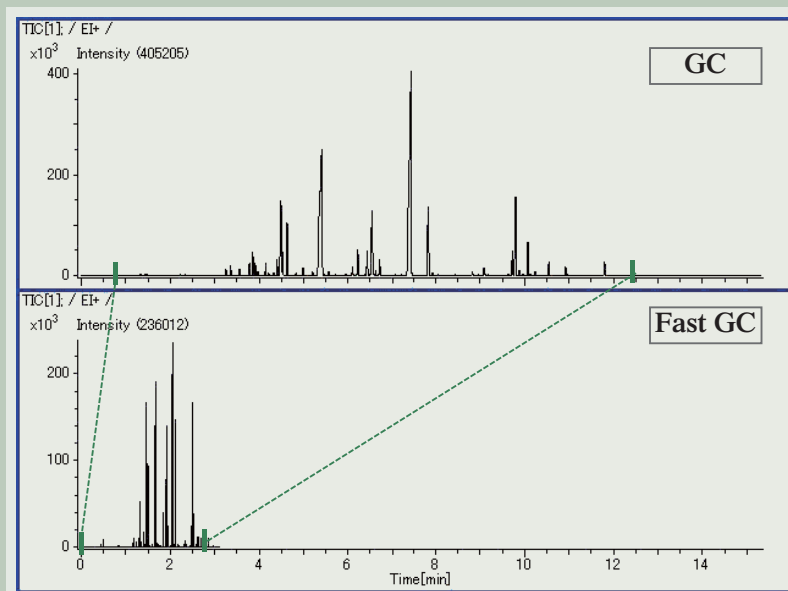


Fig. 5 Comparison of total ion chromatograms using conventional GC and fast GC methods (upper: conventional GC, lower: fast GC).

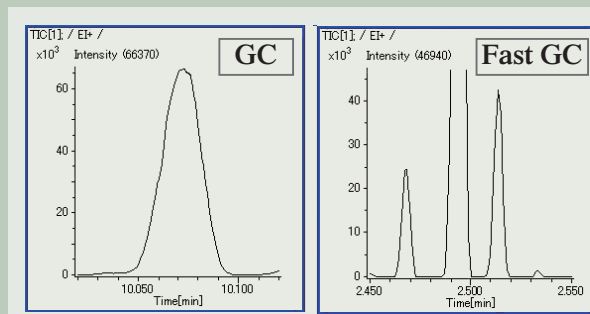


Fig. 6 Chromatogram peaks of  $\beta$ -farnesene measured using GC (left) and fast GC (right) methods (time range for both TIC is 0.1 minute).

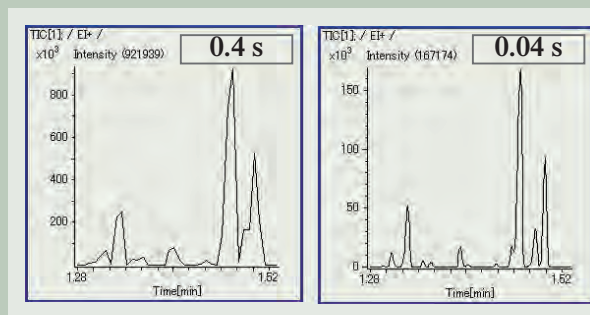


Fig. 7 Difference of chromatogram peaks with different spectrum-acquisition speeds (acquisition intervals) in fast GC method (left: 0.4 s, right: 0.04 s; both are data of AccuTOF GC).

converter (ADC) to a digital value of 0 to 255 (= 2<sup>8</sup>-1), and the data are accumulated in the summing memory. Therefore, the ADC-with-continuous averager basically does not need a statistical correction.

The AccuTOF GC adopts an ADC-with-continuous averager in the data acquisition system.

## Basic Performance

The basic performance of the AccuTOF GC is as follows.

- Resolution: 5,000 or more (FWHM, PFK m/z293)
- Mass range: 4 to 2,000
- Sensitivity
  - EI<sup>+</sup> mode: S/N ≥ 100, Octafluoronaphthalene, 1 pg (mass chromatogram of m/z 272, RMS)
  - CI<sup>+</sup> mode: S/N ≥ 150, Benzophenone, 100 pg (mass chromatogram of m/z 183, RMS)
  - Isobutane: 0.1 mL/min
  - CI<sup>-</sup> mode: S/N ≥ 20, Hexachlorobenzene, 100 fg (mass chromatogram of m/z 284, RMS)
  - Methane: 1.0 mL/min
- GC conditions:
  - Column: Agilent Technologies, DB-5ms 0.25 mm (inside diameter) × 30 m (length), 0.25 μm (film thickness)

Flow rate: Helium 1.0 mL/min (constant flow)

- Spectrum-acquisition speed: 0.04 s or longer (25 spectra/s or smaller)
- Mass accuracy: 2 mmu or 5 ppm (RMS, internal standard)

The AccuTOF GC has the features of high resolution, accurate mass measurement with easy operation, and high sensitivity as same as its sister instrument, JMS-T100LC "The AccuTOF." The AccuTOF GC furthermore attains a high spectrum-acquisition speed of 25 spectra per second, and fully corresponds to the fast GC/MS measurement.

We show data regarding the basic performance below, that are: fast GC/MS measurement, accurate mass measurement, stability, and dynamic range.

## Fast GC/MS measurement

As an example of the fast GC/MS measurement, an essential oil of lavender is measured. Here, we discuss the differences between the conventional GC and the fast GC methods, and the high spectrum-acquisition speed required for the fast GC/MS method. These two points are described briefly.

## What is fast GC method?

The fast GC method uses a narrow and short column, which shortens the analysis time while retaining a high-separation ability equiv-

alent to a conventional GC method.

An essential oil of lavender is measured using the AccuTOF GC with the conventional GC method, and also with the fast GC method, and the results are compared.

## GC parameters

- Sample injection: Split (1:500)
- Sample injection volume: 0.2 μL
- Oven program: 70°C (0.5 min) → <ramp rate: 10 °C/min> → 250°C (3 min)
- Column: DB-5ms, 0.25 mm (inside diameter) × 30 m (length), 0.25 μm (film thickness)

## Fast GC parameters

- Sample injection: Split (1:500)
- Sample injection volume: 0.2 μL
- Oven program: 70°C (0.5 min) → <ramp rate: 60°C/min> → 250 °C (3 min)
- Column: BPX-5, 0.1 mm (inside diameter) × 10 m (length), 0.1 μm (film thickness)

## MS parameters

- Mass measurement range: m/z 35 to 300
- Spectrum-acquisition speed: 0.04 s (25 spectra/s)

The parameters for GC and the fast GC differs in two points; column type and oven-temperature ramp rate. The fast GC uses a narrow and short column of 0.1 mm inside diameter and 10 m long, and the oven-temperature ramp

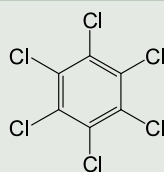


Fig. 8 Structural diagram of hexachlorobenzene (C<sub>6</sub>Cl<sub>6</sub>).

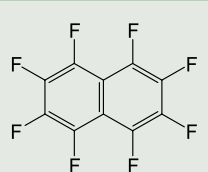


Fig. 10 Structural diagram of octafluoronaphthalene (C<sub>10</sub>F<sub>8</sub>).

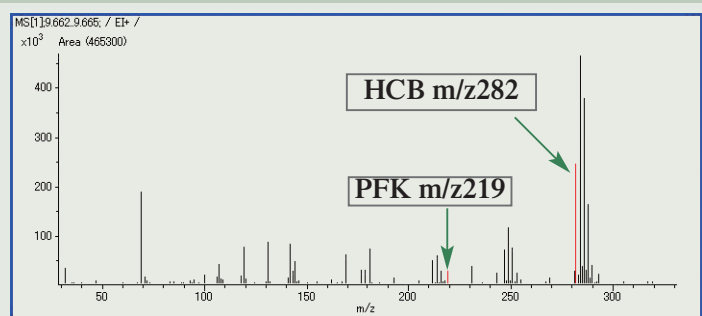


Fig. 9 Mass spectrum of mixture of PFK and hexachlorobenzene (2 ng).

Table 1 Measured masses of hexachlorobenzene with different concentrations are compared with the theoretical mass.

Sample concentration	Theoretical m/z	Measured m/z	Error (mmu)
3pg	281.81312	281.81233	- 0.79
10pg		281.81180	- 1.32
30pg		281.81196	- 1.16
100pg		281.81211	- 1.01
300pg		281.81160	- 1.52
1ng		281.81153	- 1.59
2ng		281.81214	- 0.98

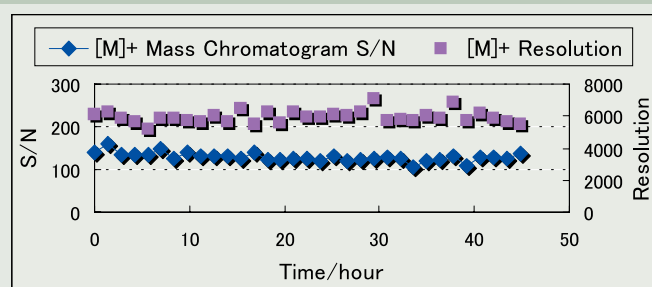


Fig. 11 Stability of sensitivity and resolution during the 45-hour continuous measurement. Sample: octafluoronaphthalene.

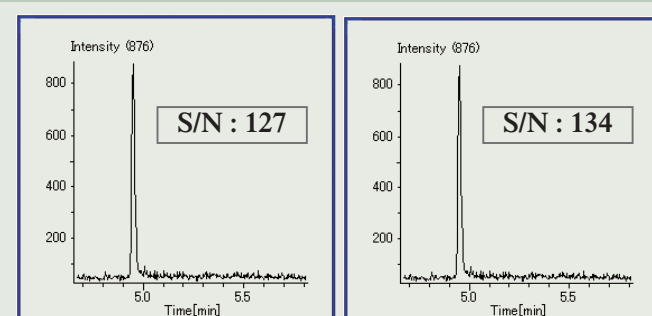


Fig. 12 Mass chromatograms of m/z 272 when starting (left) and 45 hours later (right).

rate is rapid as 60°C/min. If the rapid oven-temperature ramp rate of 60°C/min was applied to the conventional thick and long column, the peaks will overlap resulting in a poor resolution. To shorten the measurement time, it is necessary to raise the oven temperature rapidly and separate the sample rapidly. A narrow and short column satisfies this requirement.

The upper chromatogram in Fig. 5 shows a TIC taken using a conventional GC, which takes about 12 minutes, whereas, the lower chromatogram, using the fast GC, takes about 3 minutes, which is one fourth of the conventional GC. The throughput has improved four times concerning only the measurement time, excluding the preparation and data processing times. The fast GC method provides a high throughput GC/MS.

### Fast spectrum-acquisition speed required for fast GC/MS measurement

The fast GC method uses a narrow and short column. For that reason, chromatogram peaks in the fast GC/MS measurement are very sharp having widths of about 0.5 to 1 second, compared to 2 to 3 seconds using the conventional GC method (Fig. 6).

If a QMS, which is widely used in a GC-MS system, or a magnetic-field type MS, which is used for measurements such as dioxin to check for conformity with environmental regulations, is combined with a fast GC, it will not be able to acquire sufficient number of data points needed for each peak, because its spectrum-acquisition speed (scan speed) is 0.2 to 0.4 second. On the other hand, the AccuTOF GC can measure the total mass range in 0.04 second (25 spectra/s) and can follow the high-speed of the fast GC without losing the separation ability of the chromatograph and also, with high sensitivity.

Fig. 7 shows the results of the AccuTOF GC with different spectrum-acquisition speeds using the fast GC method.

The left chromatogram is measured with a spectrum-acquisition speed of 0.4 s, which is equal to the conventional magnetic-field MS and QMS, and the right is measured at a spectrum-acquisition speed of 0.04 s, the maximum speed of the AccuTOF GC. The difference between the two is quite obvious; for example at the retention time near 1.5 min, two sharp peaks are observed in the 0.04 s data, whereas the data of 0.4 s cannot separate the peaks because of the lack of data points.

As shown above, a fast spectrum-acquisition speed is necessary for the fast GC/MS measurement. The conventional magnetic-field and QMS mass spectrometers can not meet the high-speed requirement, but the AccuTOF GC can.

### Accurate mass measurement (one-point calibration)

The AccuTOF GC essentially has a high mass accuracy and therefore, calibration can be carried out correctly using the one-point calibration method. That is, the AccuTOF GC needs only one ion whose exact mass is known (internal standard ion) to measure accurate masses, whereas a magnetic-field mass spectrometer needs two or more internal standard

ions of known masses before and after the unknown peak. For example, hexachlorobenzene was analyzed as an unknown sample with PFK (m/z 219) as an internal standard for mass calibration (Fig. 9).

#### Sample

- Sample: Hexachlorobenzene (Fig. 8)
- Sample concentration: 3 pg/μL to 2 ng/μL (solvent: hexane)
- Internal standard for mass calibration: PFK

#### GC parameters

- Sample injection: Splitless
- Sample injection volume: 1.0 μL
- Oven program: 40°C (1 min) → <ramp rate: 20°C/min> → 280°C (3 min)
- Column: DB-5ms, 0.25 mm (inside diameter) × 30 m (length), 0.25 μm (film thickness)

#### MS parameters

- Mass measurement range: m/z 30 to 350

- Spectrum-acquisition speed: 0.2 s (5 spectra/s)

Table 1 shows measured masses of hexachlorobenzene with different concentrations. It shows such good mass accuracy that each mass error is smaller than -1.59 mmu.

Although we used m/z 219 of PFK in the measurement above as the mass calibration ion, m/z 207, 281 or others brought by column bleed when using a polydimethylsiloxane-bonded column can be used as the one-point calibration ion. That is, when an ion of known mass, originated in the column, is detected in the measured data, the ion can be used to calculate the accurate mass without using a standard sample.

#### Stability

Good stability when measuring continuously is one of the features of the AccuTOF GC. This comes from the stability of the newly-developed low-acceleration ion transfer system, in addition to the stability of the analyzer

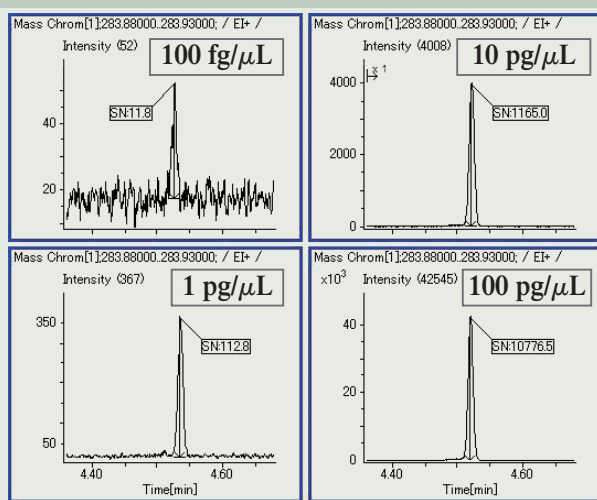


Fig. 13 Mass chromatograms of hexachlorobenzene (100 fg/μL, 1 pg/μL, 10 pg/μL, and 100 pg/μL).

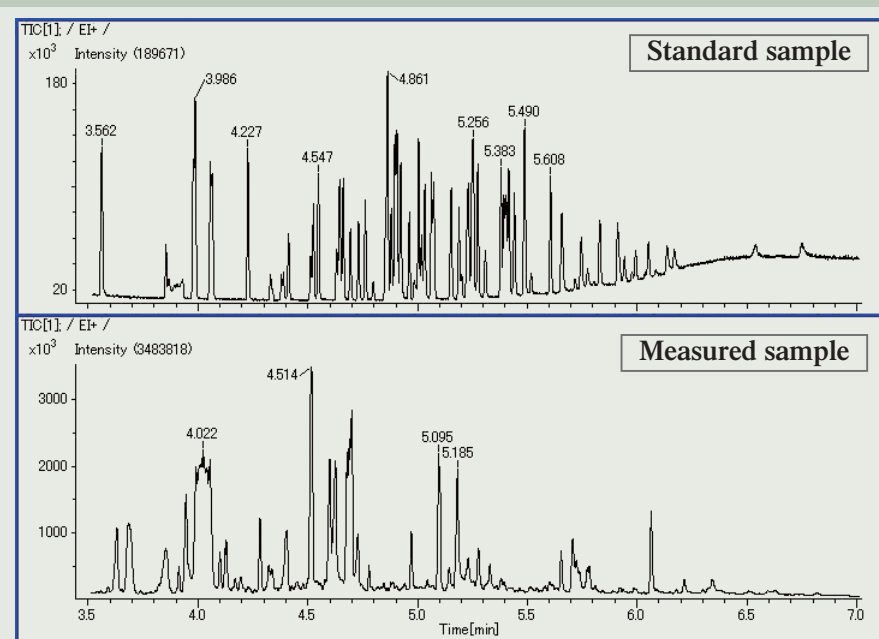


Fig. 14 Results of fast GC/MS measurements for standard sample (upper) and measured sample (lower).

already achieved by the AccuTOF. Stability is tested by measuring 1 pg of octafluoronaphthalene for 45 hours continuously (Fig.11). Octafluoronaphthalene is the sample used for specifying the sensitivity of EI positive mode.

### Sample

- Sample: Octafluoronaphthalene (Fig. 10)
- Sample concentration: 1 pg/ $\mu$ L (solvent: hexane)

### GC parameters

- Sample injection: Splitless
- Sample injection volume: 1.0  $\mu$ L
- Oven program: 40°C (1 min)  $\rightarrow$  <ramp rate: 20°C/min>  $\rightarrow$  280°C (3 min)
- Column: DB-5ms, 0.25 mm (inside diameter)  $\times$  30 m (length), 0.25  $\mu$ m (film thickness)

### MS parameters

- Mass measurement range: m/z 30 to 300
- Spectrum-acquisition speed: 0.2 s

(5 spectra/s)

At every measurement, the S/Ns of the chromatogram of m/z 272 were more than 100, and the mass resolutions at m/z 272 were more than 5,000. The sensitivity was very stable during the measurement time of 45 hours (approximately two days); the S/N was 127 at the start and 134 at 45 hours later (Fig. 12).

### Dynamic range

In order to demonstrate the dynamic range, hexachlorobenzene was analyzed at various concentrations ranging from 100 fg/ $\mu$ L to 100 pg/ $\mu$ L (100 fg/ $\mu$ L, 1 pg/ $\mu$ L, 10 pg/ $\mu$ L and 100 pg/ $\mu$ L) (Fig. 13).

The AccuTOF GC has a wider dynamic range than a conventional GC-TOFMS, realizing a dynamic range of  $10^3$  or more.

### Application Data

Here, we introduce the application data that demonstrate the features of the AccuTOF GC:

fast GC/MS measurement, improvement of selection ability using high-resolution mass chromatogram, and identifying unknown components by accurate mass measurement using CI method.

### Improvement of selection ability using high-resolution mass chromatogram

A magnetic field mass spectrometer can carry out quantitative and qualitative analysis with accuracy even when the sample contains many foreign materials (impurities), by taking advantage of its high-resolution analysis capability. In recent years, the high-resolution magnetic field mass spectrometers are playing an active part in the field of environmental analysis such as dioxin. Since the AccuTOF GC always operates at a high resolution with high sensitivity, it is expected to be applied to qualitative analysis of very small quantity compounds.

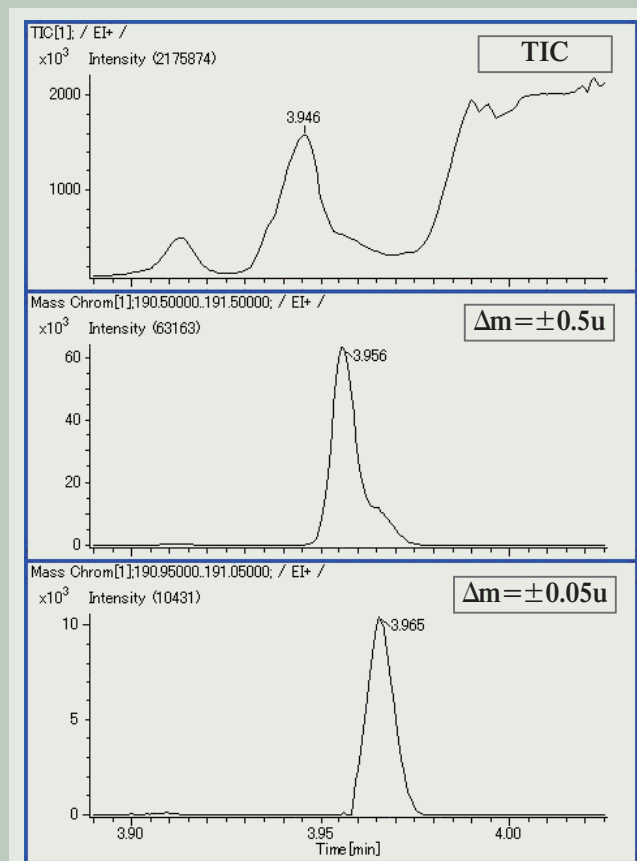


Fig. 15 TIC of the measured sample (top), and mass chromatograms of m/z 191 with  $\Delta m = \pm 0.5$  u (middle) and  $\pm 0.05$  u (bottom).

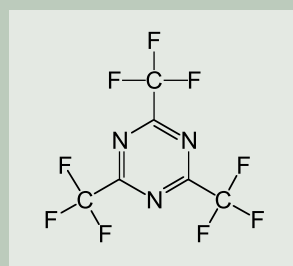


Fig. 16 Structural diagram of TTT ( $C_6N_3F_9$ ).

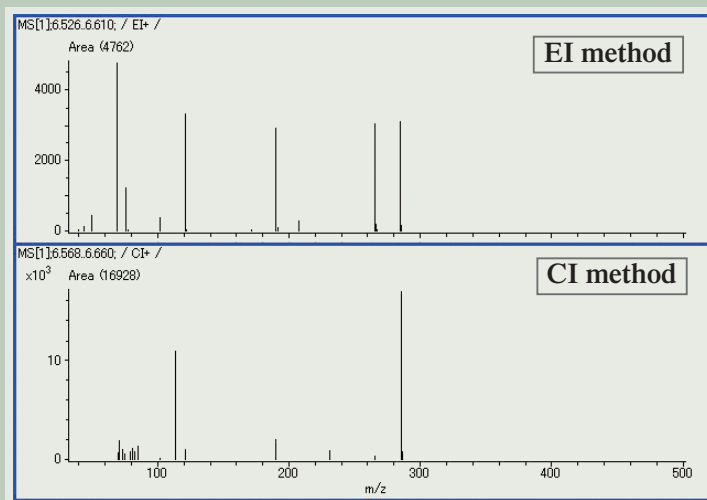


Fig. 17 Mass spectra of TTT (upper: EI method, lower: CI method).

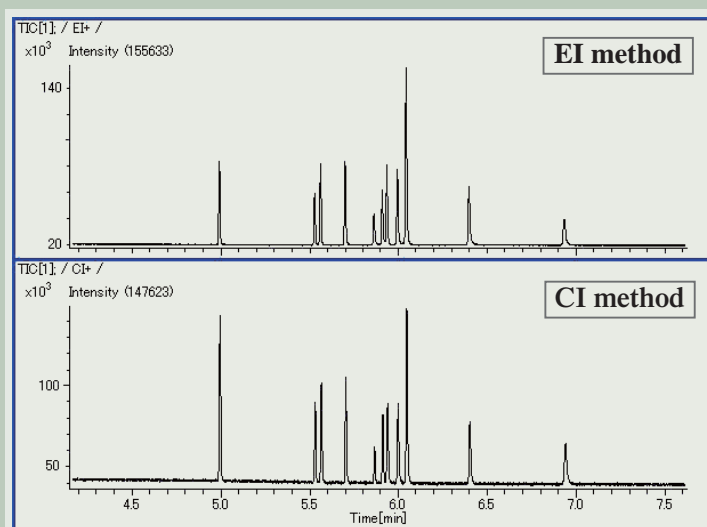


Fig. 18 TIC of liquid crystal (upper: EI method, lower: CI method).

In order to verify mass separation of a target compound from a sample containing many foreign materials using a high-resolution mass chromatogram, we added a standard sample, which includes 68 pesticides, into the extract from food, and verified that the compounds can be detected as a peak in a mass chromatogram. Measurement conditions and results are presented below.

### ■ Sample

- Standard sample: Includes 68 pesticides.
- Standard sample concentration: 50  $\mu\text{g}/\mu\text{L}$   
(solvent: hexane)
- Measured sample: Blank (extract from food) + standard sample

### ■ Fast GC parameters

- Sample injection: Splitless
- Sample injection volume: 1.0  $\mu\text{L}$
- Oven program: 40°C (1 min)  $\rightarrow$  <ramp rate: 50°C/min>  $\rightarrow$  300°C (1 min)
- Column: DB-5, 0.18 mm (inside diameter)  $\times$  10 m (length)  $\times$  0.18  $\mu\text{m}$  (film thickness)

### ■ MS parameters

- Mass measurement range: m/z 30 to 500
- Spectrum-acquisition speed: 0.04 s  
(25 spectra/s)

Figure 14 shows the TICs of the standard sample (upper) and the measured sample (lower). The measured sample is prepared by spiking 50  $\mu\text{g}$  of standard sample into the blank (extract from food). The standard sample (upper) is clearly separated, and we could identify each pesticide even in the TIC. However, it is difficult to identify the standard sample in the TIC of the measured sample (lower), because the measured sample contains many foreign materials.

In the AccuTOF GC, when you create a mass chromatogram from measured data, a mass range (window width) must be specified. That is, if a wide mass range is specified, a low-resolution mass chromatogram equivalent to the conventional low-resolution measurement is obtained. On the other hand, if a narrow mass range is specified, a high-resolution mass chromatogram is obtained.

We examined what kind of mass chromatograms are obtained when we give two window width values,  $\Delta m = \pm 0.5$  u and  $\pm 0.05$  u, to the base peak of Chloroneb,  $[\text{M}-\text{CH}_3]^+$  (m/z 191), which is one of the 68 pesticides (Fig. 15).

In the TIC (top), the intense background is observed, and the chromatogram is broad and dull. In the mass chromatogram with the window width  $\Delta m = \pm 0.5$  u (middle), a peak was observed at a retention time of 3.956 minutes. However, searching for this spectrum using the NIST library database identified that the compound is most possibly 2, 4-Di-tert-butylphenol, a different material from the spiked 68 pesticides. Next, in the mass chromatogram with the window width  $\Delta m = \pm 0.05$  u (bottom), a peak was observed at a retention time of 3.965 minutes. This peak was identified to be chloroneb using the NIST library database.

Thus, when we create a low-resolution mass chromatogram ( $\Delta m = \pm 0.5$  u, equivalent to QMS), it was difficult to find the compounds buried in the foreign materials; however, the high-resolution mass chromatogram ( $\Delta m = \pm 0.05$  u) enabled the identification of the com-

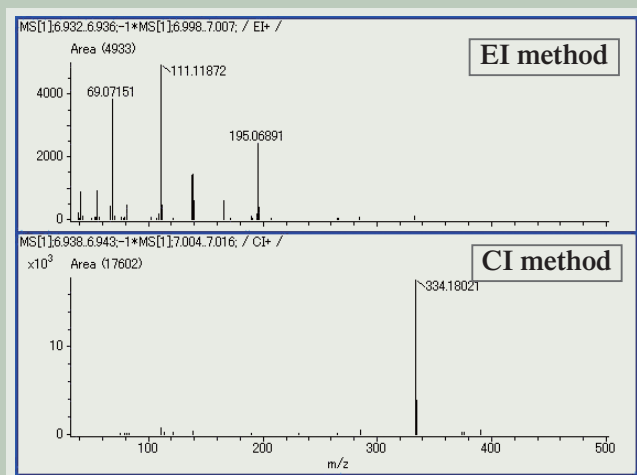


Fig. 19 Mass spectra of compound A (upper: EI method, lower: CI method).

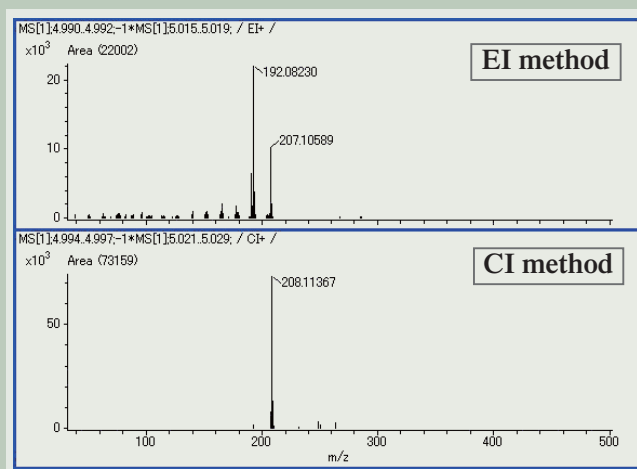


Fig. 20 Mass spectra of compound B (upper: EI method, lower: CI method).

Table 2 Calculated accurate mass of each ion.

Ionization method	Ion	Theoretical m/z	Measured m/z	Error (mmu)
EI method	$[\text{M}-\text{CH}_3]^+$	192.08132	192.08230	0.98
	$[\text{M}]^+$	207.10480	207.10589	1.09
CI method	$[\text{M}+\text{H}]^+$	208.11262	208.11367	1.05

Table 3 Composition estimation result of  $[\text{M}+\text{H}]^+$  in compound B.

Candidate	Measured m/z	Theoretical m/z	Error (mmu)	Estimated formula	Unsaturation number
No.1	334.18021	334.18070	-0.49	$\text{C}_{22}\text{H}_{24}\text{NO}_2$	11.5
No.2		334.18185	-1.64	$\text{C}_{19}\text{H}_{25}\text{FNO}_3$	7.5

Table 4 Estimated formula for each ion of compound B observed by EI method.

Ion	Measured m/z	Theoretical m/z	Error (mmu)	Estimated formula	Unsaturation number
m/z 333	333.17432	333.17288	1.44	$\text{C}_{22}\text{H}_{23}\text{NO}_2$	12
m/z 195	195.06891	195.06841	0.5	$\text{C}_{13}\text{H}_9\text{NO}$	10
m/z 111	111.11872	111.11738	1.34	$\text{C}_8\text{H}_{15}$	1.5
m/z 69	69.07042	69.07042	1.09	$\text{C}_6\text{H}_9$	1.5

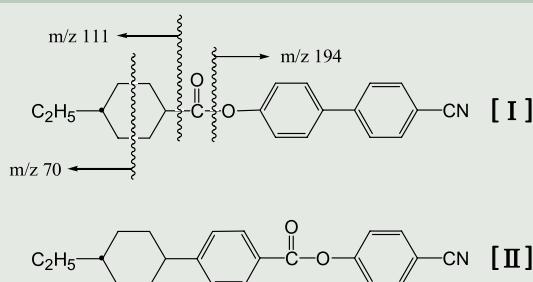


Fig. 21 Estimated structure of compound B.

pound.

In addition, we mention that the fast GC/MS measurement took only about six minutes to detect the 68 pesticides. It will take about thirty minutes for a conventional GC/MS measurement, demonstrating improvement of the throughput about five times.

### Identifying unknown compounds by accurate mass measurement using CI method

The process of the CI method is as follows: First, the reagent gas, for example, methane or isobutene, is introduced into a closed ionization chamber, and the reagent gas is ionized by the EI method. Next, the sample is introduced from the sample injection section (a GC or standard-sample injection section) into the ionization chamber. There, an ion-molecule reaction takes place between the reagent gas ions and the sample molecules resulting in the ionization of the sample.

The CI method is a soft ionization method compared to the EI method, and offers useful information for determining the molecular mass of unknown sample. As the reagent gas, methane, isobutene or ammonia is mainly used. Ions  $[M+H]^+$  are mainly observed when using the former two gases, and  $[M+NH_4]^+$  ions when using ammonia gas.

In the present experiment, we carried out a measurement that combines the CI method and "simple and accurate mass measurement", one of the features of the AccuTOF GC.

#### ■ Sample

- Sample: Liquid crystal in a commercially available pocket calculator was dissolved in a solvent (hexane).
- Internal standard compound: 2, 4, 6-Tris (trifluoromethyl)-1, 3, 5-triazine (abbreviated to TTT, Fig. 16)

#### ■ Fast GC parameters

- Sample injection: Split (1:400 (EI method), 1:200 (CI method))
- Sample injection volume: 1.0  $\mu$  L
- Oven program: 40°C (1 min)  $\rightarrow$  <ramp rate: 50°C/min>  $\rightarrow$  300°C (1 min)
- Column: DB-5, 0.18 mm (inside diameter)  $\times$  10 m (length)  $\times$  0.18  $\mu$  m (film thickness)

#### ■ MS parameters

- Measurement mass range: m/z 70 to 500
- Spectrum-acquisition speed: 0.04 s (25 spectra/s)

#### ■ CI parameters

- CI reagent gas: Isobutane
- Flow rate of CI reagent gas: 0.1 mL/min (controlled by mass-flow controller)

Figure 17 shows the mass spectra of TTT, the internal standard compound, obtained using EI (upper) and CI (lower) methods.

The TTT can be ionized by the CI method since it contains many nitrogen atoms, as well as by the EI method. Figure 17 indicates that  $[M]^+$  is obtained by the EI method and  $[M+H]^+$  by the CI method with good sensitivity. The accurate masses are calculated by one-point calibration using these ions. The measured data are shown below.

Figure 18 shows very sharp peaks since the injection method "split" is used in both EI and CI methods. To show an example of identification analysis, we selected the first peak A (compound A) at the retention time around 5.0 min and the last peak B (compound B) at the retention time around 7.0 min.

On the upper mass spectrum in Fig. 19, compound A by EI method, m/z 192 is observed as the base peak and the next intense peak is m/z 207. The lower mass spectrum in the figure, compound A by CI method, shows base peak of m/z 208. Therefore, it is inferred that m/z 207 ion observed using the EI method is the molecular ion of the compound A. The mass spectrum obtained by the EI method is searched for using the NIST library database, resulting in a compound with molecular mass of 207 as the first candidate (match: 912), that is, (1, 1'-Biphenyl)-4-carbonitrile, 4'-ethyl- ( $C_{15}H_{13}N$ ). As the next step, one-point calibration is carried out to calculate the accurate mass of it using TTT, the internal standard compound.

Accurate masses are calculated from the predicted structures of each ion (Table 2). As a result, measured values have mass errors of about 1 mmu from the theoretical values, showing very good accuracy. Thus, the compound A is determined to be (1, 1'-Biphenyl)-4-carbonitrile, 4'-ethyl- using the NIST library database search and the calculated accurate masses by using the EI and CI methods.

Next, the compound B is analyzed and discussed below. The obtained mass spectra are shown in Fig. 20.

On the upper mass spectrum in Fig. 20, compound B by EI method, m/z 111 is observed as the base peak, and m/z 69 and 195 as successive peaks. The lower mass spectrum in the figure (compound B by CI method) shows base peak of m/z 334. In the upper mass spectrum by EI, a small peak is observed at m/z 333. Therefore, it is inferred that m/z 333 is the molecular ion of the compound B. However, when we searched for the mass spectrum obtained by the EI method using the NIST library database, even the spectrum pattern of the first-candidate compound could not agree (match: 557). In addition, its molecular mass was not 333. Furthermore, other candidates did not have a molecular mass of 333. Thus, from the viewpoints of spectrum pattern and molecular mass, it is considered that there is a high possibility that this compound is not registered in the NIST library database. In order to find this unknown compound, we calculated accurate masses of each ion and estimated the composition.

Since the molecular mass of this compound is estimated to be 333, an odd number, it is considered, from the nitrogen rule, that the number of nitrogen atoms contained is odd. In the present study, estimation was carried out by aiming and estimating element species and their numbers, taking the representative liquid-crystal families into account [1]. Table 3 shows the result of the composition estimation by deducing from the accurate mass of m/z 334 in the mass spectrum obtained by the CI method. In estimating composition, the calculation was carried out with an error of 2 mmu or less.

When we consider the composition of candidate No. 2 from the compounds of the repre-

sentative liquid-crystal families, compounds having three oxygen atoms are narrowed down to azoxy compounds and p-cyano-phenyl-ester compounds of p-alkyl substitution benzoic acid. But, among these compounds, not one containing a fluorine atom has been reported [1]. From these facts, the composition of compound B is possibly and surely must be No. 1. We estimated the structure from the composition formula of No. 1 ( $C_{22}H_{24}NO_2$ ) and the fragment pattern obtained by the EI method. First, we estimated the composition formula from the accurate masses of the ions obtained by the EI method. Table 4 shows the results.

The candidate No. 1 contains one nitrogen atom, but it is known that there is no compound having an amino group (-NH<sub>2</sub>) or a nitro group (-NO<sub>2</sub>) in the liquid-crystal families. From this fact, it is estimated that the nitrogen atom in the candidate No. 1 exists in the form of a cyano group (-CN). The candidate No. 1 also includes two oxygen atoms and they are estimated to form an ester. In addition, since the unsaturation number of  $[M]^+$  is twelve, it is estimated that at least one or two benzene nuclei are included. As a result, two structures are deduced and shown in Fig. 21, that are p-cyanophenylester and cyclohexanecarboxylic acid aryl ester substitution product.

It is considered that m/z 111 is formed by a simple cleavage of an alkyl group, and m/z 69 is formed accompanying hydrogen transfer in a cyclohexane ring. These two ions can be generated from either structures [I] and [II]. However the ion m/z 195 is difficult to create from structure [II], and is deduced to arise from a simple cleavage of an alkoxy group accompanying hydrogen transfer in structure [I]. As a conclusion, the structure of the compound B is suggested to be structure [I] from the fragment ions obtained by the EI method.

## Conclusion

In the present paper, we introduced the features of the AccuTOF GC and its applications, including fast GC/MS measurement, accurate mass measurement, and improvement of selection ability using high-resolution mass chromatogram. In particular, it was demonstrated that measuring accurate masses using the EI and CI methods allows structural and qualitative analysis of the target compound with high reliability.

JMS-T100GC, the AccuTOF GC, is an innovative GC-MS that succeeds in obtaining the features that were impossible to attain simultaneously using conventional instruments. The features are: fast spectrum-acquisition speed that deals the fast GC/MS data, accurate mass measurement with simple operation, and stable, high sensitivity.

We hope the AccuTOF GC will help you in your research and studies.

## References

- [1] Liquid Crystal Compound Glossary, ed. Japan Society for the Promotion of Science, Baifukan Co., Ltd, Tokyo (in Japanese)

# Development of Ion Slicer (Thin-Film Specimen Preparation Equipment)

Akira Yasuhara

Electron Optics Division, JEOL Ltd.

Transmission electron microscope (TEM) is an indispensable tool in various fields, including research and development of new materials and failure analysis, etc. As researchers have demanded high-level analytical techniques for TEM, TEM has continued to improve its performance and capabilities from a viewpoint of hardware. On the other hand, methods of preparing thin-film specimens always draw attention, because the quality of the prepared specimen greatly affects the analysis results obtained using a TEM. The focused ion beam (FIB) method is mainly used recently; however, this method is not only accompanied by the problem of milled layers of amorphous on the specimen surface, but also has a limitation of a thinning area. To the contrary, the ion milling method and the electrolytic polishing method do not cause these problems, but they require a lot of techniques and know-how. To reduce these disadvantages, we have developed a new thin-film specimen preparation equipment (Ion Slicer) which employs a new technique, aiming for that anyone can easily prepare high-quality thin-film specimens. The principle of the Ion Slicer and its applications are presented.

## Introduction

Major methods of preparing thin-film specimens include FIB processing, ion milling and electrolytic polishing. However, these methods require various expertise and know-how and also have several disadvantages.

Though FIB processing has an advantage of simple operational technique, sometimes it induces a damaged layer on a specimen surface due to high-energy gallium ions. This damage changes the specimen into amorphous, negatively affecting the analysis results of the specimen.

Ion milling requires prior treatment of the specimen before ion sputtering for thin-film preparation. This treatment involves disc grinding and dimple grinding after disc cutting. In the prior treatment, the specimen is thinned down to a thickness of 100  $\mu\text{m}$  by disc grinding, and then, it is further thinned down to a thickness of several tens of micrometers dimple grinding. Since these mechanical polishing procedures introduce lattice distortion into the specimen, the original structure of the specimen is predicted to change. This phenomenon has long been a problem for observation of areas of interest in the specimen. In addition, in the sputtering process using argon ions, if the irradiation conditions of the argon ions are not properly selected, the argon ions implanted into the specimen cause ion radiation damage to the specimen surface.

On the other hand, electrolytic polishing requires proper selection of electrolytic solution suitable for a target material and proper control of the solution temperature. Since the electrolytic solution may generate oxides on the specimen surface, sometimes the surface layer changes its properties. Thus, careful attention has been needed for analysis.

In order to reduce the disadvantages of FIB processing, ion milling and electrolytic polishing, we have developed a new thin-film specimen preparation equipment, the Ion Slicer. The Ion Slicer uses a combination of a broad argon ion beam (hereinafter, called BIB (broad ion beam)) and a thin plate of shield material. This innovative tool bases on a thinning method using BIB milling [1] which has employed diamond particles with a low sputtering rate for a shield material. That is, by dispersing diamond particles onto the specimen surface and performing BIB milling, a columnar thin-film specimen is prepared, taking advantage of a difference in the sputtering rates of diamond and specimen. The Ion Slicer applies this technique to prepare a thin-film specimen by using a thin shielding plate instead of diamond particles as the shield material. This preparation method with a combination of a shield plate and BIB milling is, in principle, the same as Hauffe's "Ion Beam Slope Cutting [2]" and has already been applied to a JEOL cross-section specimen preparation equipment for scanning electron microscopes (SEMs). This equipment, named the Cross Section Polisher, has produced many achievements in various research fields [3].

Since the Ion Slicer is configured based on such an innovative technique, required prior treatment is only preparation of a thin plate with a thickness of about 100  $\mu\text{m}$  using mechanical polishing. Thus, it is possible for anyone to easily prepare thin-film specimens in a short time. This implies that deformation introduced into the specimen can be reduced, because the specimen is polished simply to an extent where its thickness is relatively large. Furthermore, since the specimen is irradiated with the argon ion beam at very low angles, the ions implanted into the specimen can be

drastically suppressed. This reduces the ion radiation damage to the specimen and a high-quality thin film specimen can be obtained. From a viewpoint of environmental conservation, the Ion Slicer is very eco-friendly. It requires no electrolyte and prepares specimens in a dry environment. Thus, this innovative tool eliminates a problem of oxides, drainage and waste liquid, which is accompanied by electrolytic polishing.

## Principle of Thinning

**Figure 1** is a diagram showing the principle of thin-film preparation using the Ion Slicer. As shown in Fig. 1 (a), a thin shield plate is mounted on the upper portion of a block specimen (about 0.5 mm  $\times$  2.8 mm  $\times$  0.1 mm in thickness) pre-prepared with abrasive paper, and BIB milling is applied to it. At this time, the specimen is irradiated with an argon ion beam; and the ion source is tilted up to  $\pm 6^\circ$  during the process. The ion beam sputters the specimen from its both sides for preparing a thin-film specimen. Placing the shield on the upper portion of the specimen allows low-angle BIB milling as shown in Fig. 1 (b). BIB milling is finished when perforation occurs in the specimen, and the thin-film area with a thickness less than 100 nm around the perforation is observed with a TEM. The specimen and shield plate are swung up to  $\pm 30^\circ$  perpendicular to the tilting plane of the ion source for suppressing non-uniformity caused by BIB milling. After finishing the BIB milling, the specimen is adhered to a reinforced ring and is subject to TEM observation.

**Figure 2** shows a series of images that monitor the milling process of the specimen ( $\text{Si}_3\text{N}_4$ ) taken with a CCD camera. The image taken at the start of milling (0 minute) mixes

reflected and transmitted lights. The shield plate (shield belt) is seen to be affixed on the upper portion of the specimen. The images taken during BIB milling (20 to 135 minutes) are formed by transmitted lights, revealing that a light-transparent thin area is spreading. In the image taken at 135 minutes shows that perforation occurs near the center of the thin area. The last image that mixes reflected and transmitted lights demonstrates a difference in specimen thickness depending on the intensity distribution of the ion beam.

## Instrument

**Figure 3** is the schematic diagram of the major parts of the Ion Slicer. The ion source used for argon-ion irradiation has a tilt mechanism up to  $\pm 6^\circ$ . The thin plate of shield material is configured as an endless-belt structure, affording the feeding of a new shield by feeding a belt. The specimen and the plate is combined as one unit and can be swung at up to  $\pm 30^\circ$  perpendicular to the tilt plane of the ion source. The milling process can be monitored using a CCD camera.

**Figure 4** and **Table 1** show the appearance of the Ion Slicer and its principal specifications, respectively. This equipment adopts a Penning-type argon ion source that can vary the accelerating voltage (1 to 8 kV); therefore, it can provide an argon ion beam with high current densities at low energies. The milling rate is  $5 \mu\text{m}/\text{min}$ . for Si at an accelerating voltage of 8 kV. Its evacuation system employs a turbo-molecular pump, enabling one to prepare specimens in a dry environment and to obtain clean thin films. A personal computer controls the operation of the equipment. Since a control panel is used for setting the milling conditions such as accelerating voltage and tilt parameters of the ion source (**Fig. 5**), anyone can easily operate this Ion Slicer.

In addition, this equipment has a function of monitoring the milling process by automatic acquisition of CCD images. Thus, the Ion Slicer can stop the irradiation of argon ions and finishes thin-film preparation at the moment perforation occurs in the specimen.

## Application

**Figure 6** shows 100 kV-TEM images of a mineral prepared with the Ion Slicer and a 30

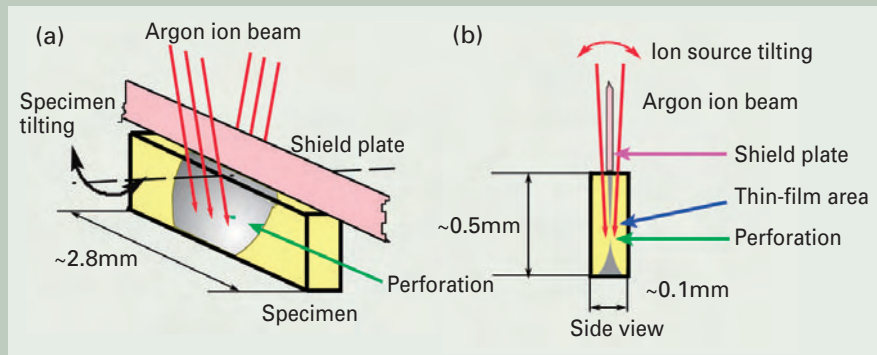


Fig. 1 Diagram showing the principle of argon-beam polishing using a shield plate.

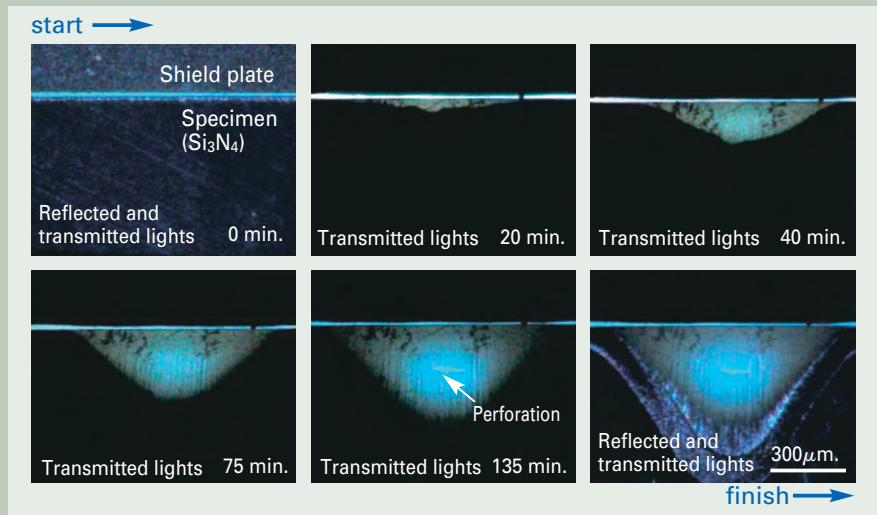


Fig. 2 Milling process of specimen ( $\text{Si}_3\text{N}_4$ ).

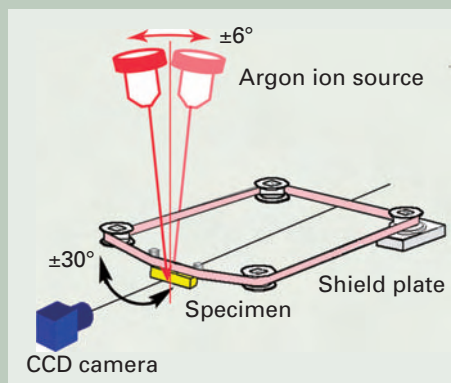


Fig. 3 Schematic diagram of the Ion Slicer.

Table 1 Specifications of the Ion Slicer.

● Ion source	Penning-type argon ion source
● Tilt angle of ion source	Up to $\pm 6^\circ$ ( $0.1^\circ$ step)
● Accelerating voltage	1 to 8 kV
● Milling rate	$5 \mu\text{m}/\text{min}$ . (8 kV, silicon)
● Evacuation system	TMP, RP



Fig. 4 Appearance of the Ion Slicer.

kV-STEM image. The BIB milling time is about one hour. Figure 6 (a) is a low-magnification TEM image, indicating that a thin film with a relatively uniform thickness is produced over a wide area. Figure 6 (b) of a high-resolution TEM image characterizes lattice fringes with a spacing of 1 nm in a lamellar crystal, demonstrating a small irradiation damage to the specimen. In addition, in the STEM image obtained with ultra-high resolution FE SEM (Fig. 6 (c)), lattice fringes are observed even at a low accelerating voltage of 30 kV, indicating that a sufficiently thin specimen is prepared.

**Figure 7** shows TEM image of ceramics (SiAlON) taken at an accelerating voltage of 200 kV. It takes about two hours for BIB milling. A high-contrast lattice image is obtained at a high magnification, indicating that an amorphous layer on the specimen surface is very thin. **Figure 8** is a TEM image of a thin film of metal titanium at an accelerating voltage of 200 kV. This specimen was prepared by a two-hour BIB milling. It is found that even from titanium, which is difficult to thin, a sufficiently thin film over a wide area is obtained. Each specimen in Figs. 6 to 8 is prepared within a two-hour BIB milling. This implies that a thin film can be prepared in a short time. In addition, these application examples demonstrate that low-angle ion irradiation can reduce unevenness of specimen thickness and high-quality thin films can be prepared over a wide area.

**Figure 9** shows a STEM bright-field image and a HAADF image of a laminated ceramic capacitor at an accelerating voltage of 200 kV, together with elemental mapping using an EDS. As is found from the result of elemental mapping, metal (Ni) and ceramics (BaTiO<sub>3</sub>) coexist in the capacitor. Even if this material has different hardnesses and etching rates, a thin film with an even surface can be obtained using the Ion Slicer. We also mention that it is possible to easily prepare a thin-film specimen even from a porous composite by low-angle irradiation of argon ions.

## Conclusion

A thin-film specimen preparation equipment (Ion Slicer), which combines a thin shield plate and BIB milling, can prepare thin-film specimens faster and easier than with conventional preparation tools. In addition, this equipment can suppress deformation introduced into the specimen, which was a problem in conventional mechanical polishing. Furthermore, the Ion Slicer affords low-angle ion-beam irradiation for drastically reducing irradiation damage to the specimen. These advantages of the Ion Slicer will contribute to preparation of high-quality thin-film specimens.

## References

- [1] M. Kawasaki, T. Yoshida and M. Shiojiri, *J. Elec. Microsc.*, **48**, 131-137 (1999)
- [2] W. Hauffe: "Production of Microstructures by Ion Beam Sputtering" in Particle Bombardment III, eds, R. Behrisch and K. Wittmaack ; Springer-Verlag, Berlin 305-338 (1991)
- [3] M. Shibata, *JEOL news* **Vol. 39**, No. 1, 28-31 (2004)



Fig. 5 Control panel.

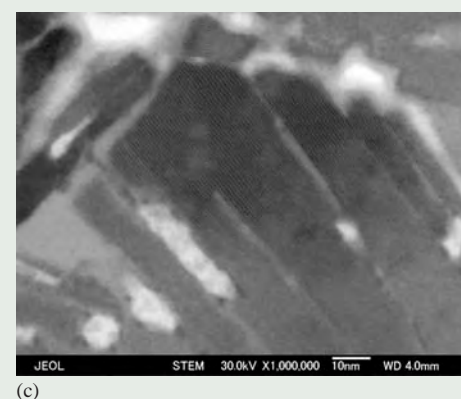
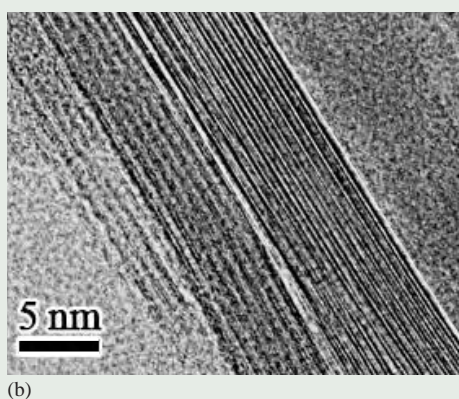
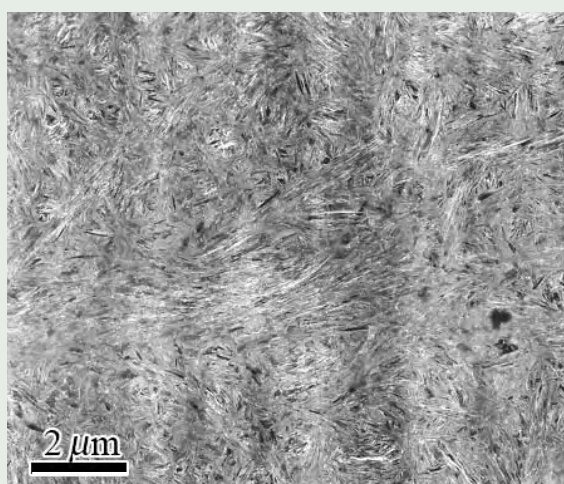


Fig. 6 TEM and STEM images of mineral (argon irradiation time: about one hour). (a) low magnification image at 100 kV, (b) high resolution image at 100 kV, and (c) STEM image at 30 kV.

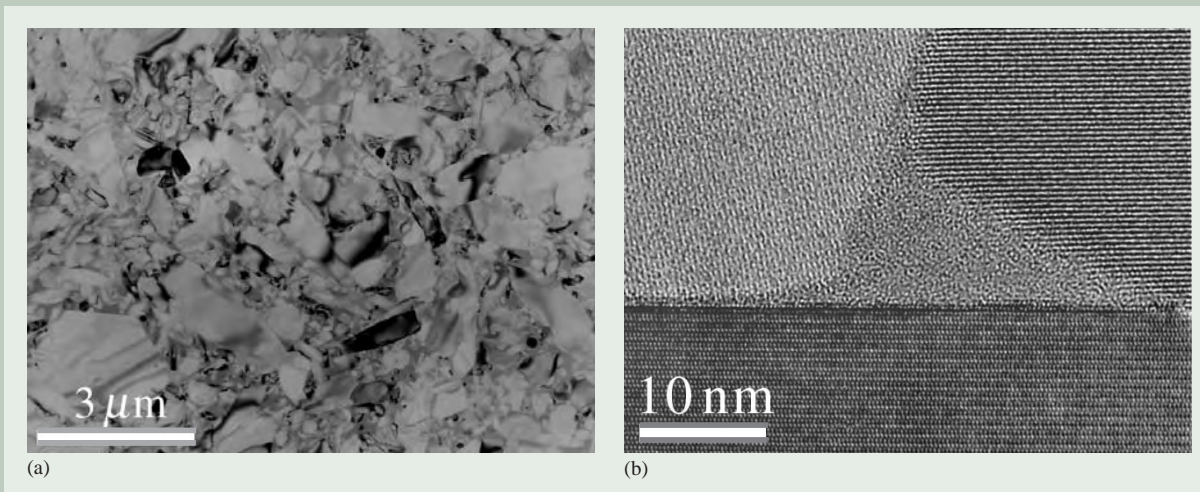


Fig. 7 TEM images of ceramics (SiAlON) at 200 kV (argon irradiation time: about two hours).

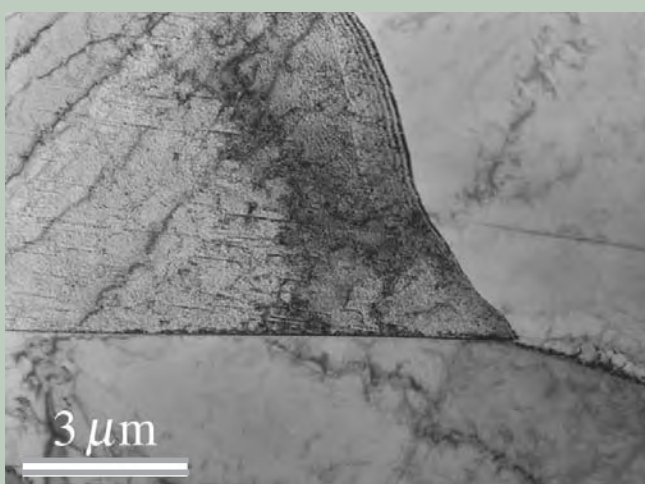


Fig. 8 TEM image of metal titanium at 200 kV (argon irradiation time: about two hours).

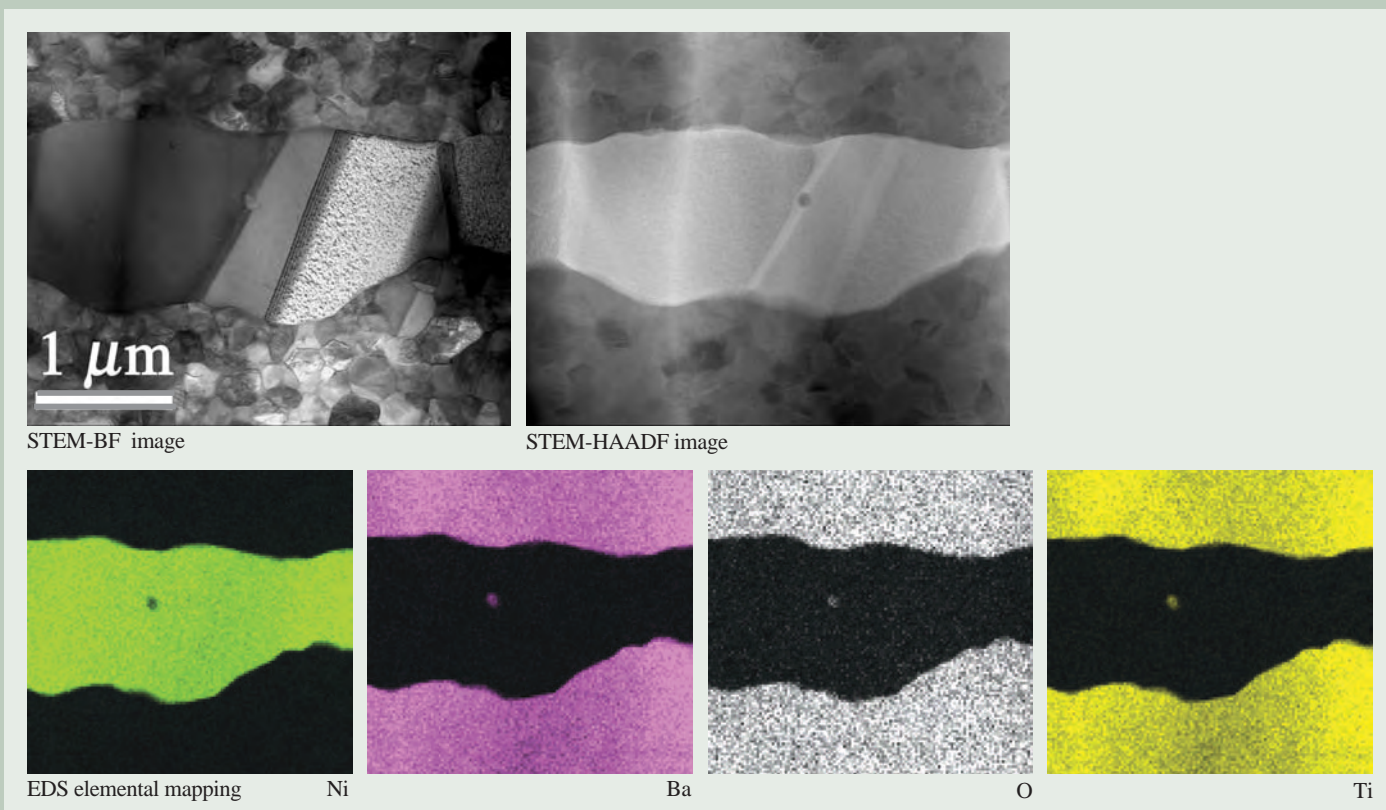


Fig. 9 STEM-BF/HAADF images and elemental mapping of laminated ceramic capacitor obtained at 200 kV.

# Introduction of Wafer Edge SEM Review

Tomohiro Mihira

Semiconductor Equipment Division, JEOL Ltd.

## Introduction

Wafer edge problems are beginning to be pointed out with progress in larger-diameter silicon wafers and practical use of 300 mm wafers.

There are two problems of wafer edges. The first is wafer cracks that have come to be serious with the employment of 300 mm wafers.

A wafer crack not only wastes a wafer that came through the semiconductor production processes, but also causes a large downtime in the production equipment because the wafer cracks in the equipment. A crack in the wafer edge leads to a crack of the entire wafer. That is, if the wafer has a crack in the edge, as the stress applied to a wafer increases in many production processes, the wafer cracks.

The second problem is yield degradation due to dust generated from the wafer edge.

As the device production process proceeds, deposition and peeling-off of insulating and metallic films results in contamination, particles adhering to the wafer and scratches on it. The resultant particles come around on the wafer surface and they cause a "killer defect". In addition, as the wafer diameter increases, the number of chips on the wafer surface also increases, together with the increase in the number of chips on the periphery of the wafer. The chips near the periphery are easily affected by particles peeled off from the edge, and the dust from the edge greatly degrades the yield. Furthermore, in the process where deposition is applied to the entire wafer surface, deposited films come around to the lower bevel of the wafer edge, and this phenomenon causes contamination in the subsequent processes.

Under these problematic circumstances, defect analysis/management of the wafer edge, which previously did not draw attention, is becoming more important in recent years.

To solve the above problems, JEOL will propose defect analysis/management of the wafer edge by Wafer Edge SEM Review.

## Wafer Edge SEM Review

### Outline

JEOL DRT-SEMs (defect-review-tool scanning electron microscopes), the JWS/JFS series, have conventionally used tilting/rotat-

ing stages. Also, the JWS/JFS series employ a conical objective lens for higher SEM resolution and a eucentric stage for tilt observation. These features are widely accepted to be very effective for defect analysis of wafer surfaces. Recently, these features, particularly tilting/rotating stages, have found also to be effective for observation of wafer edges.

The JWS/JFS series can observe wafer surfaces tilted up to 60°. Observation of the wafer edge at 60° allows one to view the lower bevel and apex of the edge as well as the wafer surface. In addition, since the wafer stage of the JWS/JFS can endlessly rotate over 360° with 0.1° step rotational movement, an operator can observe the entire circumference of the wafer.

**Figure 1** shows the observable range of the wafer edge using the JWS/JFS series. As mentioned above, using the wafer stage of the JWS/JFS, an operator can limitlessly and easily observe a broad range of the wafer edge, illustrated in **Fig. 1 (left)**.

Furthermore, since an optional EDS (energy-dispersive X-ray) detector can be attached to the instrument, EDS measurement can be performed for defects on the wafer edge. In this way, the JWS/JFS series provide composition analysis of the wafer edge through EDS measurement as well as wafer edge observation, thus enabling one to obtain necessary information to be fed back to each production process.

Featuring their wealth of capabilities, the JWS/JFS series are increasingly attracting much attention, as powerful tools for wafer edge analysis.

### New functions

For smooth and easy analysis of wafer edges using the JWS/JFS series, JEOL has developed two new functions (**Fig. 2**).

#### Coordinate linkage with Raytex EdgeScan+

The coordinate-linkage function has enabled the JWS/JFS to link with the coordinate system of the Raytex EdgeScan+, the industry-standard, optical wafer edge defect-inspection system.

An optical wafer edge defect-inspection system measures positions where defects are present. Using this new function, the JWS/JFS instruments can concentrate on observing

defect points according to the positional information measured by a wafer edge defect-inspection system. This capability allows one to inspect and analyze defects on the wafer-edge with high throughput.

#### Automatic observation of wafer-edges

The Auto Edge Review function automatically captures a sequence of SEM images of the entire circumference of the wafer edge. Since the images are saved in the computer, after capturing the images, an operator can review the images and determine the presence or absence of defects and the defect positions. This function is effective for users who do not have wafer edge defect-inspection systems.

## Application Example of Wafer Edge SEM Review

**Figure 3** shows an example of Wafer Edge SEM Review.

SEM images in **Fig. 3** show that part of the tungsten (W) film deposited on the wafer edge is peeled off. It is said that the adhesion between the substrate and the deposited film is low, and these SEM images prove this thinking.

If the peeled-off W film adheres to the wafer surface, this can degrade the yield. The SEM images suggest that it is necessary to mill the deposited W film before it peels off from the wafer edge.

In this way, SEM observation of wafer-edges enables one to take measures for the process of the wafer edge, which was not done previously.

## Summary

JEOL will propose Wafer Edge SEM Review for defect analysis of wafer edges, which is now drawing attention. The wafer stage of the JWS/JFS series can tilt over a wide range and afford rotational movement, enabling one to easily observe wafer edges. Furthermore, EDS analysis as well as SEM observation allows one to precisely obtain detailed information on defects on the wafer edge and feed the information back to the production processes. Thus, Wafer Edge SEM Review will play an important role in yield improvement of semiconductor devices.

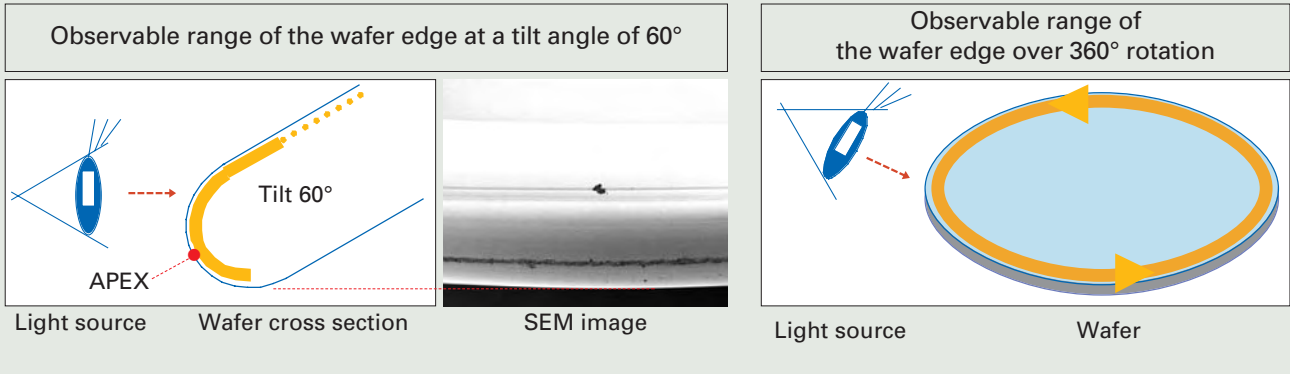


Fig. 1 Observable range of the wafer edge.

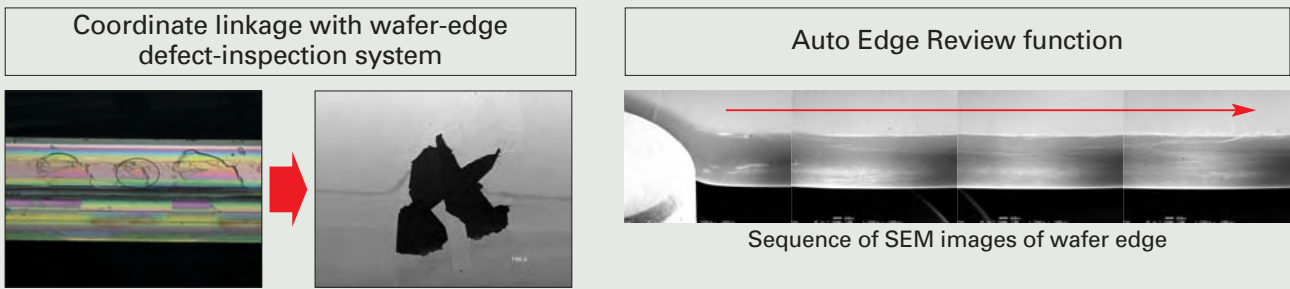


Fig. 2 Effective functions for wafer edge observation.

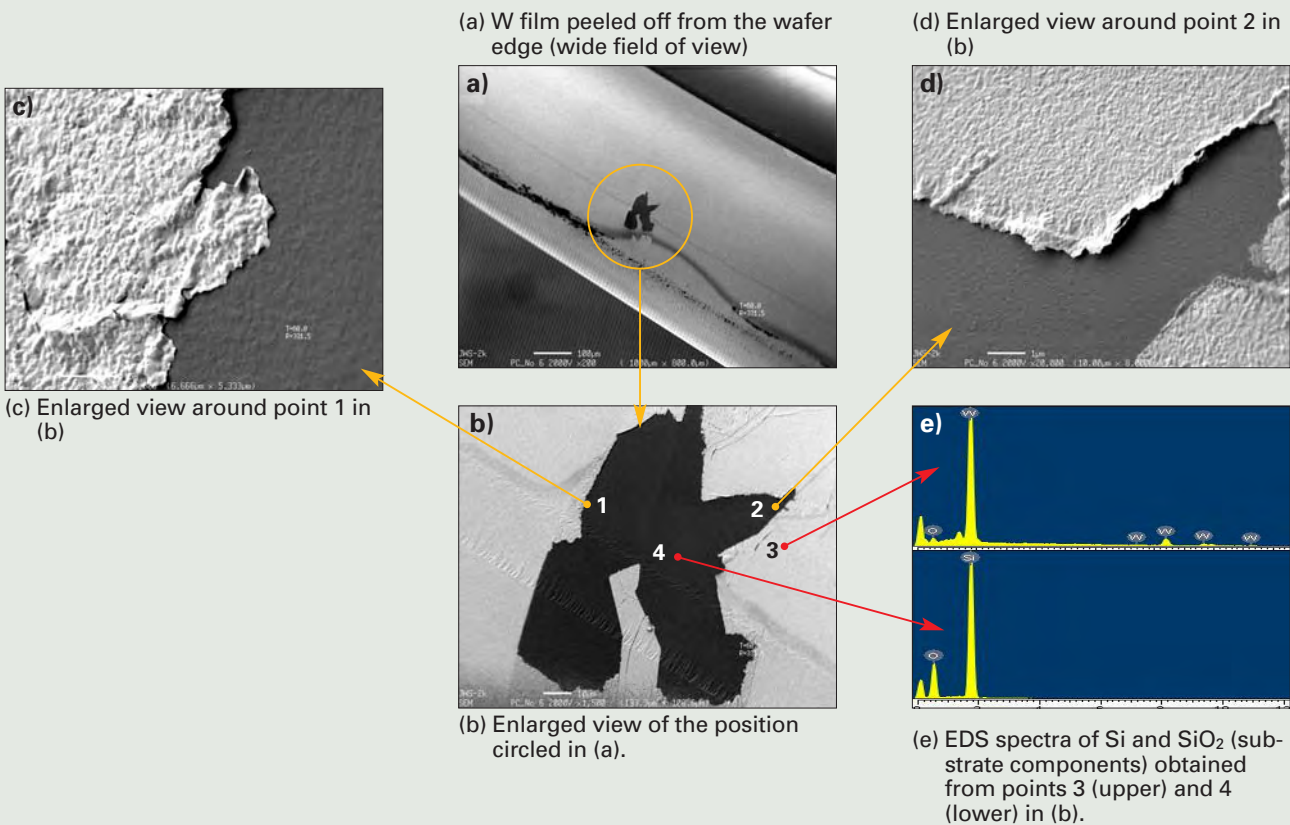


Fig. 3 Application example of Wafer Edge SEM Review to observation of peeling-off of W film.



Certain products in this brochure are controlled under the "Foreign Exchange and Foreign Trade Law" of Japan in compliance with international security export control. JEOL Ltd. must provide the Japanese Government with "End-user's Statement of Assurance" and "End-use Certificate" in order to obtain the export license needed for export from Japan. If the product to be exported is in this category, the end user will be asked to fill in these certificate forms.

**JEOL JEOL Ltd.** 1-2 Musashino 3-chome Akishima Tokyo 196-8558 Japan Sales Division ☎(042)528-3381 ㊚(042)528-3386 <http://www.jeol.co.jp/>

#### ARGENTINA

COASIN S. A. C. I. yF.  
Virrey del Pino 4071,  
1430 Buenos Aires, Argentina  
Telephone: 54-11-4552-3185  
Facsimile: 54-11-4555-3321

#### AUSTRALIA & NEW ZEALAND

JEOL (AUSTRALASIA) Pty. Ltd.  
Unit 9, 750-752 Pittwater Road,  
Brookvale, N. S. W. 2100, Australia  
Telephone: 61-2-9905-8255  
Facsimile: 61-2-9905-8286

#### AUSTRIA

LABCO GmbH  
Dr.-Trittemmel-Gasse 8,  
A-3013 Pressbaum, Austria  
Telephone: 43-2233-53838  
Facsimile: 43-2233-53176

#### BANGLADESH

A. C. CHOWDHURY & CO. Pvt. Ltd.  
Baridhara Central Plaza 87, Suhrawardy Avenue  
2nd Floor Baridhara,  
Dhaka-12129 Bangladesh  
Telephone: 880-2-9862272, 9894583  
Facsimile: 880-2-988070

#### BELGIUM

JEOL (EUROPE) B. V.  
Zaventem/Ikaros Business Park,  
Ikaroslaan 7A, B-1930 Zaventem, Belgium  
Telephone: 32-2-720-0560  
Facsimile: 32-2-720-6134

#### BRAZIL

FUGIWARA ENTERPRISES  
INSTRUMENTOS CIENTIFICOS LTDA.  
Avenida Itaberaba,3563  
02739-000 Sao Paulo, SPI Brazil  
Telephone: 55-11-3983-8144  
Facsimile: 55-11-3983-8140

#### CANADA

JEOL CANADA, INC.  
(Represented by Soquelec, Ltd.)  
5767 Cavendish Boulevard, Suite 540,  
Montreal, Quebec H4W 2W8, Canada  
Telephone: 1-514-482-6427  
Facsimile: 1-514-482-1929

#### CHILE

TECSIS LTDA.  
Avenida Holanda 1248,  
Casilla 5019 Correo 9, Providencia, Santiago, Chile  
Telephone: 56-2-205-1313  
Facsimile: 56-2-225-0759

#### CHINA

JEOL LTD., BEIJING OFFICE  
Room No. B2308,  
Vantone New World Plaza,  
No. 2 Fuvai Street, Xicheng District,  
Beijing 100037, P. R. China  
Telephone: 86-10-6804-6321/6322/6323  
Facsimile: 86-10-6804-6324

#### JEOL LTD., SHANGHAI OFFICE

Sanhe Building 11F2, Yan Ping Road,  
No. 121, Shanghai 200042, P. R. China  
Telephone: 86-21-6246-2353  
Facsimile: 86-21-6246-2836

#### JEOL LTD., GUANG ZHOU OFFICE

S2204 World Trade Center Building  
371-375, Huang Shi East-Road, Guang Zhou,  
510095, P. R. China  
Telephone: 86-20-8778-7848  
Facsimile: 86-20-8778-4268

#### JEOL LTD., WUHAN OFFICE

Room. 3216, World Trading Bld., 686 Jiefang Street,  
Hankou, Wuhan, P. R. China  
Telephone: 86-27-8544-8953  
Facsimile: 86-27-8544-8695

#### FARMING LTD.

Unit 1009, 10/F., MLC Millennium Plaza  
663 King's Road, North Point, Hong Kong  
Telephone: 852-2815-7299  
Facsimile: 852-2581-4635

#### CYPRUS

MESLO LTD.  
Scientific & Laboratory Division,  
P. O. Box 27709, Nicosia Cyprus  
Telephone: 357-2-666070  
Facsimile: 357-2-660355

#### EGYPT

JEOL SERVICE BUREAU  
3rd Fl. Nile Center Bldg.,  
Naval Street, Dokki, (Cairo), Egypt  
Telephone: 20-2-335-7220  
Facsimile: 20-2-338-4186

#### FRANCE

JEOL (EUROPE) SAS  
Espace Claude Monet,  
1, Allée de Giverny 78290  
Croissy-sur-Seine, France  
Telephone: 33-13015-3737  
Facsimile: 33-13015-3747

#### GERMANY

JEOL (GERMANY) GmbH  
Oskar-Von-Miller-Strasse 1,  
85386 Eching Germany  
Telephone: 49-8165-77346  
Facsimile: 49-8165-77512

#### GREAT BRITAIN & IRELAND

JEOL (U.K.) LTD.  
JEOL House, Silver Court, Watchmead,  
Welwyn, Garden City, Herts AL7 1LT., England  
Telephone: 44-1707-377117  
Facsimile: 44-1707-373254

#### GREECE

N. ASTERIASIS S. A.  
56-58, S. Trikoupi Str. P.O.Box 26140  
GR-10022 Athens, Greece  
Telephone: 30-1-829-8383  
Facsimile: 30-1-823-9567

#### INDIA

Blue Star LTD. (HQ)  
Analytical Instruments Department,  
"Sahas 414/2 Veer Savarkar Marg,  
Prabhadey Mumbai 400 025, India  
Telephone: 91-22-5666-4068  
Facsimile: 91-22-5666-4001

#### Blue Star LTD. (New Delhi)

Analytical Instruments Department,  
E-44/12 Okhla Industrial Area,  
Phase-11, New Delhi 110 020, India  
Telephone: 91-11-5149-4000  
Facsimile: 91-11-5149-4004

#### Blue Star LTD. (Calcutta)

Analytical Instruments Department,  
7, Hare Street Calcutta 700 001, India  
Telephone: 91-33-2248-0131  
Facsimile: 91-33-2248-1599

#### Blue Star LTD. (Chennai)

Analytical Instruments Department, Lakshmi  
Neela Rite Choice Chambers, 5, Bazulsh Road,  
3rd Floor T. Nagar Chennai 600 017, India  
Telephone: 91-44-2815-8015  
Facsimile: 91-44-2815-8015

#### INDONESIA

PT. TEKNOLABINDO PENTA PERKASA  
J1. Gading BukitRaya,  
Komplek Gading Bukit Indah Blok I/11,  
Kelapa Gading Jakarta 14240, Indonesia  
Telephone: 62-21-45847057/58/59  
Facsimile: 62-21-45842729

#### IRAN

IMACO LTD.  
No. 141 Felestin Ave.,  
P. O. Box 13145-537, Tehran, Iran  
Telephone: 98-21-6402191/6404148  
Facsimile: 98-21-8978164

#### ITALY

JEOL (ITALIA) S.p.A.  
Centro Direzionale Green Office Via Dei Tulipani,  
1, 20090 Pieve, Emanuele (MI), Italy  
Telephone: 39-2-9041431  
Facsimile: 39-2-90414353

#### KOREA

JEOL KOREA LTD.  
Sunmin Bldg. 6th F1., 218-16, Nonhyun-Dong,  
Kangnam-Ku, Seoul, 135-010, Korea  
Telephone: 82-2-511-5501  
Facsimile: 82-2-511-2635

#### KUWAIT

YUSUF I. AL-GHANIM & CO. (YIACO)  
P. O. Box 435, 13005 - Safat, Kuwait  
Telephone: 965-4832600/4814358  
Facsimile: 965-4844954/4833612

#### MALAYSIA

JEOL (MALAYSIA) SDN. BHD. (359011-M)  
205, Block A, Mezzanine Floor,  
Kelana Business Center#7,  
Jalan SS 7/2, Kelana Jaya,  
47301 Petaling Jaya, Selangor, Malaysia  
Telephone: 60-3-7492-7722  
Facsimile: 60-3-7492-7723

#### MEXICO

JEOL DE MEXICO S.A. DE C.V.  
Av. Amsterdam #46 DEPS. 402  
Col. Hipodromo, 06100 Mexico D.F. Mexico  
Telephone: 52-5-55-211-4511  
Facsimile: 52-5-55-211-0720

#### PAKISTAN

Analytical Measuring System (Pvt.) Limited, AMS House  
Plot # 14C, Main Sehar Commercial Avenue,  
Commercial Lane 4,  
Khayaban-e-Sehar,  
D.H.A Phase 7, Karachi, Pakistan  
Telephone: 92-21-5345581/5340747  
Facsimile: 92-21-5345582

#### PANAMA

PROMED S.A.  
Parque Industrial Costa del Este  
Urbanizacion Costa del Este  
Apartado 6281, Panama, Panama  
Telephone: 507-269-0044  
Facsimile: 507-263-5622

#### PHILIPPINES

PHILAB INDUSTRIES INC.  
7487 Bagtikan Street, SAV Makati, 1203 Metro,  
Manila Philippines  
Telephone: 63-2-896-7218  
Facsimile: 63-2-897-7732

#### PORTUGAL

Izasa. Portugal Lda.  
R. do Proletariado 1,  
2790-138 CARNAXIDE Portugal  
Telephone: 351-21-424-7300  
Facsimile: 351-21-418-6020

#### SAUDI ARABIA

ABDULREHMAN ALGOSAIBI G. T. B.  
Algasaihi Bldg. Airport Rd., P. O. Box 215,  
Riyadh 11411, Saudi Arabia  
Telephone: 966-1-479-3000  
Facsimile: 966-1-477-1374

#### SCANDINAVIA

JEOL (SKANDINAVISKA) A.B.  
Hammarbacken 6 A, Box 716  
191 27 Sollentuna, Sweden  
Telephone: 46-8-28-2800  
Facsimile: 46-8-29-1647

#### SERVICE & INFORMATION OFFICE

JEOL NORWAY  
Ole Deviks vei 28, N-0614 Oslo, Norway  
Telephone: 47-2-2-64-7930  
Facsimile: 47-2-2-65-0619

#### JEOL FINLAND

Ylakaupinkuja 2, FIN-02360 Espoo, Finland  
Telephone: 358-9-8129-0350  
Facsimile: 358-9-8129-0351

#### JEOL DENMARK

Naverland 2, DK-2600 Glostrup, Denmark  
Telephone: 45-4345-3434  
Facsimile: 45-4345-3433

#### SINGAPORE

JEOL ASIA PTE. LTD.  
29 International Business Park,  
#04-02A Acer Building,  
Tower B Singapore 609923  
Telephone: 65-6565-9989  
Facsimile: 65-6565-7552

#### SOUTH AFRICA

ADI Scientific (Pty) Ltd.  
109 Blandford Road, North Riding,Randburg  
(PO box 71295 Bryanston 2021)  
Republic of South Africa  
Telephone: 27-11-462-1363  
Facsimile: 27-11-462-1466

#### SPAIN

IZASA S.A.  
Aragoneses, 13,  
28100 Alcobendas,  
(Poligono Industrial) Madrid, Spain  
Telephone: 34-91-663-0500  
Facsimile: 34-91-663-0545

#### SWITZERLAND

JEOL (GERMANY) GmbH  
Oskar-Von-Miller Strasse 1,  
85386 Eching Germany  
Telephone: 49-8165-77346  
Facsimile: 49-8165-77512

#### TAIWAN

JIE DONG CO., LTD.  
7F, 112, Chung Hsiao East Road, Section 1, Taipei,  
Taiwan 10023, Republic of China  
Telephone: 886-2-2395-2978  
Facsimile: 886-2-2322-4655

#### JEOL TAIWAN SEMICONDUCTORS LTD.

11F, No. 346, Pei-Ta Road, Hsin-Chu City 300,  
Taiwan Republic of China  
Telephone: 886-3-523-8490  
Facsimile: 886-2-523-8503

#### THAILAND

BEOETHAI BANGKOK EQUIPMENT  
& CHEMICAL CO., Ltd.  
300 Phaholyothin Rd. Phayathai,  
Bangkok 10400, Thailand  
Telephone: 66-2-615-2929  
Facsimile: 66-2-615-2350/2351

#### THE NETHERLANDS

JEOL (EUROPE) B.V.  
Tupolevlaan 28-A, 1119 NZ Schiphol-Rijk,  
The Netherlands  
Telephone: 31-20-6533088  
Facsimile: 31-20-6531328

#### TURKEY

TEKSER LTD. STI.  
Acibadem Cad. Erdem Sok. Bayer Art. 6/1  
34660 Uskudar/Istanbul-Turkey  
Telephone: 90-216-3274041  
Facsimile: 90-216-3274046

#### UAE

BUSINESS COMMUNICATIONS LLC.  
P. O. Box 2534, Abu Dhabi UAE  
Telephone: 971-2-6348495  
Facsimile: 971-2-6316465

#### USA

JEOL USA, INC.  
11 Dearborn Road, Peabody, MA. 01960, U. S. A.  
Telephone: 1-978-535-5900  
Facsimile: 1-978-536-2205/2206

#### JEOL USA, INC. WEST OFFICE

5653 Stoneridge Drive Suite  
#110 Pleasanton, CA. 94588 U. S. A.  
Tel: 1-925-737-1740  
Fax: 1-925-737-1749

#### VENEZUELA

MITSUBISHI VENEZOLANA C. A.  
Avenida Francisco de Miranda Los Palos Grandes,  
Caracas, Venezuela  
Telephone: 58-212-209-7402  
Facsimile: 58-212-209-7496